Sea urchin membrane transport mechanisms for calcification and pH homeostasis

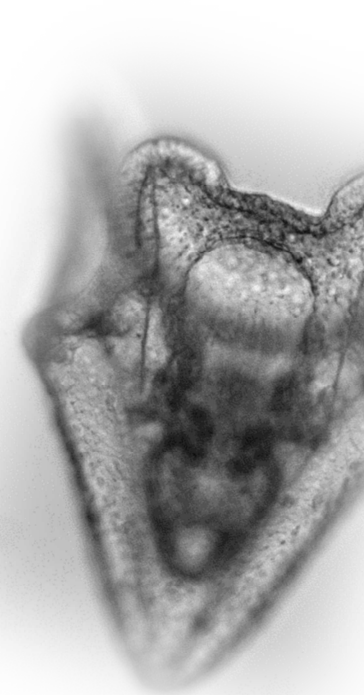

Dissertation
zur Erlangung des Doktorgrades
der Mathematisch-Naturwissenschaftlichen Fakultät
der Christian-Albrechts-Universität zu Kiel
vorgelegt von

Wiebke Catharina Holtmann
Kiel, 2013

Erster Gutachter: Prof. Dr. Markus Bleich
Zweiter Gutachter: Prof. Dr. Frank Melzner

Tag der mündlichen Prüfung: 17.06.2013
Zum Druck genehmigt am: 24.06.2013

Gez. Prof. Dr. Wolfgang J. Duschl, Dekan

… one can always enjoy life, with a small microscope and a few sea urchins.

Jean Brachet, 1973

Table of Contents

List of Abbreviations

ACC	amorphous calcium carbonate
ASW	artificial seawater
CA	carbonic anhydrase
CMFSW	calcium magnesium free seawater
DIDS	4,4´-diisothiocyanatostilbene-2,2´-disulfonate
DMSO	dimethylsulfoxid
FITC	fluorescein-isothiocyanate
FSW	filtered seawater
fwd	forward PCR primer
$[HCO_3^-]_e$	extracellular bicarbonate concentration
$[HCO_3^-]_{PCF}$	bicarbonate concentration of the perivisceral coelomic fluid
PCF	perivisceral coelomic fluid
PFA	paraformaldehyde
pH_e	extracellular pH
pH_i	intracellular pH
pH_{PCF}	pH of perivisceral coelomic fluid
PMC	primary mesenchyme cell
rev	reverse PCR primer
R_{te}	transepithelial resistance
RVI	regulatory volume increase
MCT	mutable collagenous tissue
NKCC	$Na^+K^+2Cl^-$ cotransporter
TAL	thick ascending limb
TEP	transepithelial potential
TJ	tight junction
sd-NKCC	NKCC of *Strongylocentrotus droebachiensis*
SEM	scanning electron microscopy
SJ	septate junction
sp-NKCC	NKCC of *Strongylocentrotus purpuratus*
SMC	secondary mesenchyme cell
V_{te}	transepithelial voltage

Summary

Larval sea urchins serve as a model organism for calcification and adult individuals are a keystone species in marine shelf ecosystems. Both life stages will presumably be affected by alterations of seawater pCO_2 and the accompanying change in pH, $[HCO_3^-]$ and $[CO_3^{2-}]$. This change in seawater carbonate chemistry is known as ocean acidification and is based on anthropogenically caused increase in pCO_2 by burning fossil fuels and deforestation. Ocean acidification is thought to affect marine organisms in terms of acid-base regulation but also in terms of calcification, somatic growth and reproductivity. To understand the impact of ocean acidification on calcification processes a profound knowledge of the underlying cellular mechanisms is needed.
This thesis is split into two main topics: cellular mechanisms involved in sea urchin larval calcification, and ocean acidification related effects on skeletal elements and mechanisms for acid-base regulation of the perivisceral coelomic fluid (PCF) in adult sea urchins.

To understand more about the cellular mechanisms involved in sea urchin calcification, larvae of *Strongylocentrotus droebachiensis* were raised in the presence of different ion transport protein inhibitors and the primary body rod length of pluteus larvae was taken as a measure for calcification. This investigation challenged the current cell model of sea urchin ion transport. The model had been developed on the basis of high drug concentrations which partially resulted in toxic side effects on larval development.
The inhibitors used in this study targeted the $Na^+K^+2Cl^-$ cotransporter (NKCC), L-type Ca^{2+} channel, Ca^{2+} ATPase, anion exchangers (SLC4-family), H^+K^+ ATPase and V-ATPase. I could show that loop diuretics inhibited calcification selectively and could prove that NKCC is expressed in sea urchin larvae. In addition, the function of the cotransporter in the primary mesenchyme cells (PMCs) was addressed and it could be shown that this transporter is needed for maintaining the cytoplasmic cord, *i.e.* the part of the PMCs which sheaths the larval spicule. In contrast, the other drugs caused toxic side effects in whole larvae assays. This questions any published interpretation concerning the direct involvement of the respective transport proteins in calcification mechanisms.

It has recently been shown that adult *S. droebachiensis* can regulate its pH of PCF by increasing $[HCO_3^-]$ during long-term exposure to elevated CO_2 (6 weeks, 102 and 284 Pa). The underlying mechanisms are still unknown. However, stereom dissolution and active HCO_3^- reabsorption mechanisms *via* the intestine are two possible distinct hypotheses. I investigated the epithelia which are covering the PCF space for their putative role in barrier and transport function.
The peritoneal epithelium, an epithelial barrier between the stereom and the PCF, was shown to be rather leaky for ions. This favours the direct contact of the stereom to any PCF acid-base condition.

The intestine exhibited low transepithelial resistance and a relative cation selectivity. It was found to be tight for HCO_3^- suggesting a contribution to acid-base regulation of PCF by representing a diffusion barrier against the loss of HCO_3^- from PCF into the intestine.

During acute-exposure to hypercapnic conditions (< 4 days) the corrosive character of the PCF resulted in minor dissolution events which led to a partial increase in $[HCO_3^-]_{PCF}$. Long-term exposure (6 weeks) did not cause any further ossicle dissolution but daily ossicle growth was reduced. In contrast to the ossicles, primary spines were severely affected by the long-term hypercapnic exposure resulting in destabilisation and dissolution.

Zusammenfassung

Seeigellarven dienen als Modelorganismus zur Erforschung von Kalzifizierungsprozessen, adulte Seeigel sind eine Schlüsselart in marinen Schelf-Ökosystemen. Es ist anzunehmen, dass Seeigel in der Zukunft durch pCO_2 Änderungen im Seewasser und die damit einhergehenden Änderungen in pH, $[HCO_3^-]$ und $[CO_3^{2-}]$ beeinflusst werden. Diese Änderung in der Karbonatchemie ist bekannt als Ozeanversauerung, ausgelöst durch das Verbrennen von fossilen Brennstoffen und Abholzung. Beide anthropogenen Tätigkeiten führen zu einem Anstieg in atmosphärischem CO_2, das wiederrum mit dem Ozean im Equilibrium steht. Es wird angenommen, dass Ozeanversauerung marine Organismen auf verschiedenen Ebenen beeinflusst: zum einem in der Säure-Base Regulation, aber auch in der Kalzifizierung, dem Wachstum und der Fortpflanzung. Um den Einfluss von Ozeanversauerung auf Kalzifizierung zu verstehen ist es notwendig, fundierte Kenntnisse über die der Kalzifizierung zugrunde liegenden Mechanismen zu erlangen.
Die vorliegende Arbeit ist in zwei Themenfelder aufgeteilt. Zum einen wurden die Mechanismen, die an der Kalzifizierung von Seeigellarven beteiligt sind, untersucht. Zum anderen wurden in adulten Seeigeln Mechanismen zur Säure-Base Regulation der Coleomflüssigkeit (PCF) und Effekte der Ozeanversauerung auf adulten Skelettanteile untersucht.

Um die zellulären Mechanismen der Larvenkalzifizierung zu untersuchen, wurden Larven des Seeigels *Strongylocentrotus droebachiensis* unter Inhibitoren verschiedener ionaler Transportproteine wachsen gelassen. Die Länge des „primary body rods“ wurde als Maß für die Kalzifizierung genommen. Durch diese Untersuchung wurde das aktuell gültige Zellmodel des Ionentransportes zur Kalzifizierung in Seeigellarven überprüft. Dieses Model wurde aus Studien, die hohe Inhibitorenkonzentrationen verwendet haben und teilweise toxische Nebeneffekte berichtet haben, entwickelt.
Die in der vorliegenden Studie verwendeten Inhibitoren blockieren $Na^+K^+2Cl^-$ Kotransporter (NKCC), L-type Ca^{2+} Kanal, Ca^{2+} ATPase, Anionenaustauscher (SLC4-family), H^+K^+ ATPase und V-ATPase. Es konnte gezeigt werden, dass die verwendeten Schleifendiuretika selektiv die Kalzifizierung inhibiert haben. Zudem konnte die Expression von NKCC in Seeigellarven durch RT-PCR bestätigt werden und es wurde gezeigt, dass NKCC notwendig ist, um die „cytoplasmic cords“, PMC-Membranausläufer, die die Kalknadeln ummanteln, aufrechtzuerhalten. Alle anderen Inhibitoren haben trotz gering eingesetzter Konzentrationen toxische Artefakte auf Entwicklung und Larvenvitalität hervorgerufen. Dies stellt die publizierten Interpretationen über die direkte Beteiligung der jeweiligen Transportproteine innerhalb der Kalzifizierung in Frage.

Vor kurzem konnte gezeigt werden, dass adulte *S. droebachiensis*, die in einem Langzeitexperiment erhöhten CO_2 ausgesetzt waren (6 Wochen, 102 und 284 Pa), den pH der PCF durch einen Anstieg in

[HCO_3^-] regulieren können. Die zugrundeliegenden Mechanismen sind unbekannt; die Auflösung des Stereoms oder eine aktive HCO_3^- Reabsorption durch den Darm stellen mögliche Kompensationsmechanismen dar. Die Epithelien, die in Kontakt mit der PCF stehen, wurden auf ihre mögliche Rolle als Barriere oder transportierendes Epithel hin untersucht.

Das peritoneale Epithel, welches das Stereom vom PCF trennt, zeigte eine hohe ionale Durchlässigkeit. Dadurch ist es wahrscheinlich, dass das Stereom jeder Säure-Base Änderungen der PCF ebenfalls ausgesetzt ist. Der Darm entwickelte einen geringen transepithelialen Widerstand und eine relative Kationenselektivität. Obwohl der geringe Widerstand das Gewebe als ionendurchlässig charakterisiert, konnte eine HCO_3^--Barrierefunktion gezeigt werden. Durch diese Barriere kann ein HCO_3^- Verlust über den Darm verhindert werden und das Gewebe kann somit zur Säure-Base Regulation der PCF beitragen.

Während kurzeitigen hyperkapnischen Bedingungen (< 4 Tage) waren die Ossikel korrosiven Bedingungen der PCF ausgesetzt, was wiederrum in leichten Auflösungen der Ossikel resultierte. In Langzeitexperimenten (6 Wochen) führte die Regulation der PCF dazu, dass keine weiteren Auflösungen eintraten; die Wachstumsrate der Ossikel wurde jedoch unter hyperkapnischen Bedingungen reduziert. Im Gegensatz zu den Ossikeln wurden die primären Stacheln durch anhaltende erhöhte pCO_2 Werte (6 Wochen) in ihrer Stabilisation beeinträchtigt und wiesen Auflöseerscheinungen auf.

1 Introduction

1.1 Sea urchins

The phylum echinodermata belongs to the deuterostomia; within the phylum five modern classes are known: the echinoidea (sea urchins and sand dollars), the asteroidea (sea stars and cushion stars), the crinoidea (sea lilies and feather stars), the ophiuroidea (brittle stars and basket stars) and the holothuroidea (sea cucumbers). Adult echinodermata are characterised by radial symmetry (except for holothuroidea and sand dollars) in contrast to the bilaterally symmetric larvae. The phylum possesses a mesodermal skeleton and a water vascular system.

Within the echinodermata the class echinoidea is best understood with regard to its developmental biology (Ettensohn et al., 2004). Furthermore, the larvae serve as a model for calcification (chapter 1.1.3.1).

In this thesis, I studied the larval and adult stages of the Baltic green sea urchin *Strongylocentrotus droebachiensis* with respect to calcification related transport processes, membrane transport and effects of ocean acidification on adult calcification.

1.1.1 Ecology

The distribution of the green sea urchin is broad and includes the North Atlantic, North Pacific, Barents, White, Kara, and Chukchi Sea (Scheibling and Hatcher, 2007). The animals used in this study originated from the Baltic Sea (Kattegat and Oslo Fjord).

Within the ecosystem *S. droebachiensis* is an omnivorous keystone species. By feeding on kelp and other macroalgae, they shape the benthos: in regions where extensive feeding has occurred so-called barrens develop (characterised by loss of macroalgae, abundant coralline algae) (reviewed by Scheibling and Hatcher, 2007). In addition to their function as a predator, they also serve as prey for fish, crustaceans (*e.g.* crab and lobster) and starfish.

1.1.2 Larval development

The time needed for complete development is species- and temperature-dependent. The relevant stages and ages for this thesis for *S. droebachiensis* at 10.6°C were: blastula hatching (28 h), gastrula stage (47.5 h), prism (72 h), and four arm pluteus (120 h) (Figure 1). These points of time only represent the incubation times I used.

After fertilisation the embryo develops encased by the fertilisation membrane until the blastula stage (Figure 1). In this stage, cilia are formed all over the blastula surface and the blastula hatches. At the late blastula stage, cells of the vegetal pole start to ingress into the blastocoel. These cells are determined in the 16-cell stage to become primary mesenchyme cells (PMCs) (Figure 1c) and ingress into the blastocoel prior to gastrulation (Figure 1e). When gastrulation begins the archenteron

invaginates from the vegetal pole into the blastocoel to form the primitive gut and later the digestion system of the larvae. Larvae then continue developing through the following stages: prism stage, 4-arm pluteus, 8-arm pluteus. The pluteus larvae start feeding on planktonic algae by producing a current towards their mouth with cilia along the arms. Depending on the food availability the arms grow to be short (high amount of food) or long (low amount of food) (McEdward and Herrera, 1999; Miner, 2005; Adams et al., 2011). In the 8-arm pluteus the later juvenile is formed as a rudiment on the left side of the digestive tract (Smith et al., 2008). The juvenile sea urchin exhibits all characteristics of adult urchins and hatching occurs after the larvae have settled on substrate.

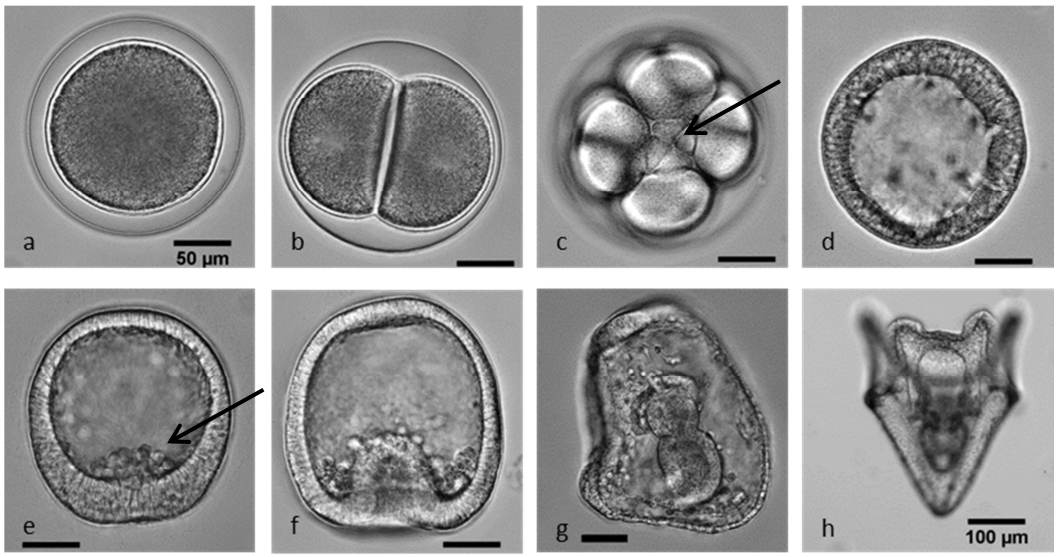

Figure 1 Development of *Strongylocentrotus droebachiensis*. (a) Development of a fertilisation membrane, (b) first cleavage after 3 h (10.6°C), (c) four micromeres, ancestors of the PMCs, marked with an arrow (8 h 40 min, 10.6°C), (d) hatched blastula (28 h, 10.6°C), (e) PMC-ingression (37.5 h, 10.6°C), marked with an arrow, (f) early gastrula (49 h, 10.6°C), (g) prism stage (72 h, 10.6°C); (h) 4-arm pluteus larva (> 120 h, 10.6°C). Scale bars: a-f: 50 µm, f: 100 µm

1.1.3 Calcification in sea urchins

Sea urchins possess a mesodermal skeleton made of Mg-calcite throughout their whole life cycle. In larvae two spicules are formed, in adults the skeleton is represented by the ossicles and spines. Additional skeletal parts in adults are the jaws, pedicellaria and parts of the tube feet.

In the following sections the calcification processes in both life stages, as well as the transient mineral phase of calcite and the organic matrix are described.

1.1.3.1 Calcification in sea urchin larvae

PMCs of sea urchin larvae are a distinct cell type which is responsible for the formation of the Mg-calcite spicules. Their precursors are determined rather early in larval development (chapter 1.1.2). Descendants of these cells ingress into the blastocoel of the late blastula stage and form a syncytium at the vegetal pole and around the ingressing archenteron.

At the middle gastrula stage the spicule formation begins. Starting from the first calcite-precursor the spicules will grow into three directions and form a triradiate spicule (Figure 2). The elongation rate is 5 µm h^{-1} (Beniash et al., 1997) and the increment in thickness of the primary body rod is 4-6 µm between prism and pluteus stage (Beniash et al., 1999).

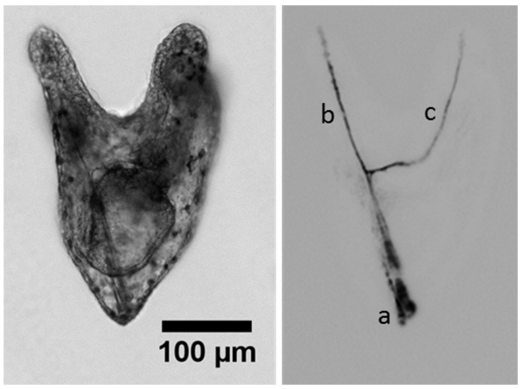

Figure 2 Lateral view of the three rods of larval skeleton. The left picture is a bright field picture, the right image was taken using polarised light (inverted colours and brightness adjustment for best visualisation; skeleton = black); (a) primary body rod, (b) antero-lateral rod and (c) post-oral rod.

Microanatomy of primary mesenchyme cells

The PMCs are ~8 µm in diameter and form a syncytial network with their filopodia. In Figure 3 PMCs *in vivo* are shown and the cytoplasmic cord (thick filopodia in which spicule deposition takes place) are visualised. The cytoplasmic cords do not fully surround the spicules, thus exchange with the fluids of the extracellular body cavity is possible and the spicules are directly influenced by the alkaline conditions of the body cavity (Wilt, 1999, 2002; Stumpp et al., 2012a).

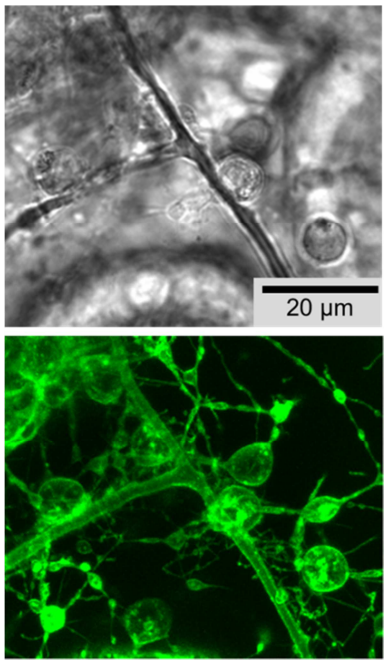

Figure 3 Primary mesenchyme cells *in vivo* (bright field image) and stained with the membrane dye FM®1-43. In the lower picture, the cytoplasmic cord and filopodia are visible.

Within the PMCs vesicles of different types are detectable: yolk granules (Ingersoll et al., 2003), polymembranous granules (Beniash et al., 1999; Ingersoll et al., 2003) and post-Golgi transport vesicles (Ingersoll et al., 2003). The polymembranous granules are known to be rich in Ca^{2+} (Decker et al., 1987), and transport amorphous $CaCO_3$ (ACC) (Beniash et al., 1999). These vesicles are stainable for calcein (Wilt et al., 2008) and are 0.5-1.5 µm in diameter in contrast to the smaller post-Golgi vesicles (< 50 nm). Moreover, it has been shown that integral matrix proteins and ACC are transported separately in post-Golgi vesicles and polymembranous granules, respectively (Ingersoll et al., 2003; Wilt et al., 2008).

The polymembranous granules will be called calcification vesicles in the following text.

Ion transport

The current knowledge of ion transport in sea urchin larvae originates mostly from studies which are more than 20 years old. In the following section I will give an overview about the current knowledge

of calcification related ion transport in larvae (Figure 4).

The inorganic carbon used for calcification originates from both seawater as well as larval metabolism. In contrast, calcium originates exclusively from seawater (Sikes et al., 1981). Calcium uptake in embryos starts at the mesenchyme blastula stage and is dependent on the developmental stage (Nakano et al., 1963; Fujino et al., 1985; Mitsunaga et al., 1987b) and calcium appears to be stored at large amounts prior to precipitation (Wilt et al., 2008).

The expression of SERCA- and plasma membrane Ca^{2+} ATPases directly involved in calcium transport increases over the course of development (Jayantha Gunaratne and Vacquier, 2007). Several inhibitors can interfere and stop Ca^{2+} uptake. L-type calcium channel blockers (*e.g.* verapamil, nifedipine, diltiazem) have been used and resulted in inhibition of calcification and ^{45}Ca-uptake (Fujino et al., 1985; Yasumasu et al., 1985; Mitsunaga et al., 1986c, 1989; Hwang and Lennarz, 1993; Dale et al., 1997).

Carbonic anhydrases (CA) catalyse the reaction of CO_2 to HCO_3^- and H^+ in biological systems. The inhibition of this enzyme has been shown to inhibit spicule calcification (Carson et al., 1985; Mitsunaga et al., 1986a). Moreover, three CA-encoding genes in sea urchin larvae can be found in PMCs (Livingston et al., 2006) and the enzyme activity throughout the development is species specific (Chow and Benson, 1979; Mitsunaga et al., 1986a).

The activity of the plasma membrane H^+K^+ ATPase is detectable not before the start of calcification (Mitsunaga et al., 1987a, 1987b, 1989) and the inhibition of this protein inhibits also calcification (Fujino et al., 1987; Mitsunaga et al., 1987b, 1989) and decreases pH_i of PMCs (Mitsunaga et al., 1989). Another, Na^+ and HCO_3^- dependent, H^+extrusion mechanism has been proposed by Stumpp et al. (2012a).

In addition, the inhibition of Cl^--transport by loop diuretics (*e.g.* furosemide and ethacrynic acid) interfered negatively with calcification and has been hypothesised to be mediated by a $Cl^-HCO_3^-$ ATPase (Fujino et al., 1985; Yasumasu et al., 1985; Mitsunaga et al., 1986b, 1986c, 1987a) located in the calcification vesicles of PMCs (Mitsunaga et al., 1987a).

Not only the involvement of ion transporters and channels has been investigated, also the importance of a functioning endomembrane system for calcification has been shown by disrupting the endomembrane system (*e.g.* Golgi apparatus and ER) by monensin and brefeldin A (Hwang and Lennarz, 1993).

Some of these results and the following assumption of the involvement of certain transporters have, however, to be re-considered carefully. For example, in some loop diuretic related studies the inhibitor concentrations were chosen too high to guarantee inhibitor specificity. In addition, the existence of a $Cl^-HCO_3^-$ ATPase has to be re-considered based on the current knowledge of loop diuretic targets (chapter 1.2.3).

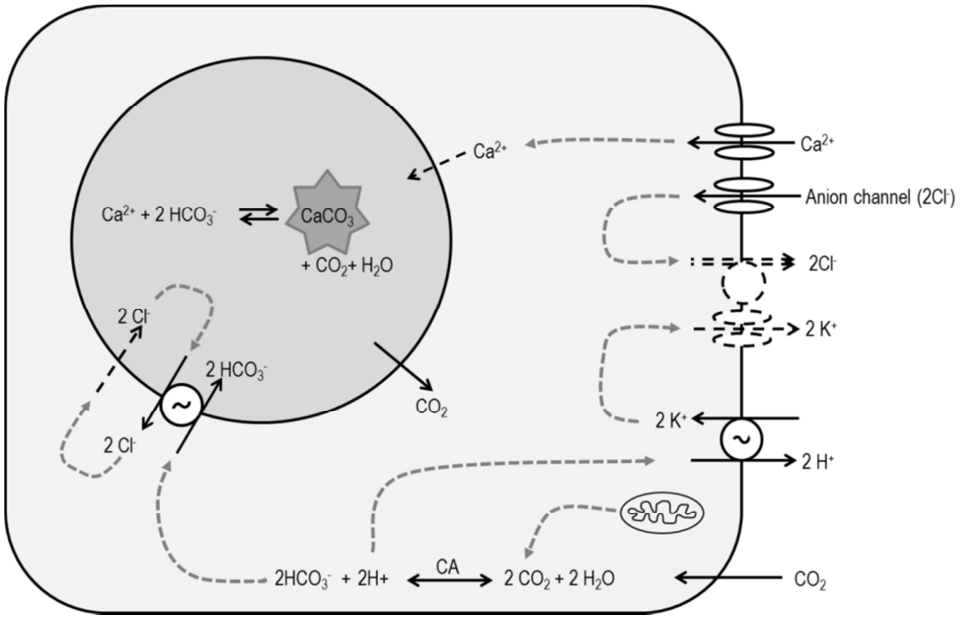

Figure 4 Current cell model for sea urchin larval calcification (after Mitsunaga et al., 1987a). Note that some of the mentioned transporters and pumps (SERCA, Na^+, HCO_3^- dependent H^+ extrusion mechanism) are not involved in this model as their existence has been shown rather recently and their location within the PMCs remains unclear. Proposed ion pathways are dashed in black, previously detected pathways are in solid black. Grey dashed lines show the further processing of ions. The outer membrane shows the plasma membrane of primary mesenchyme cells, the inner membrane resembles the calcification vesicle.
The model describes that Ca^{2+} is taken up *via* a channel and is transported into the calcification vesicle. Anions (presumably Cl^-) are recirculating and are coupled to a K^+ channel. An H^+K^+ ATPase is needed for pH_i homeostasis. HCO_3^- is processed mainly from metabolic CO_2 and is assumed to be transported into the calcification vesicle *via* a $Cl^-HCO_3^-$ ATPase. This ATPase is further coupled to an unknown Cl^- transport.

1.1.3.2 Calcification in adult sea urchins

Anatomy of adult skeletal parts

In the following section, I will focus on the mesodermally derived skeletal parts ossicles and spine as they were investigated in this study.

Ossicles are connected *via* connective tissue and form the test. They are arranged in two rows which in turn are defined as ambulacral and interambulacral and are arranged in alternate order and only the ambulacral plates contain tube feet (Figure 5a). Approximately 50% of the ossicle volume is Mg-calcite; the remaining 50% is filled by stroma (fluid, coelomocytes and connective tissue). This fenestrated skeleton is called the stereom (Figure 5d).

Sea urchin spines are connected to the ossicles *via* connective tissue and muscles. The base of the spines is adjacent to the ossicles tubercle (Figure 5c). Three types of spines can be classified according to their length: primary, secondary and tertiary spines, with primary being the longest. They are also characterised by a stereom structure and in non-cidaroid sea urchins - such as *S. droebachiensis* - the entire length of the spines is covered with an epidermis throughout the entire adult life stage. In contrast, fully grown spines of cidaroid sea urchins are not covered by an epidermis but by a polycrystalline cortex layer (Märkel and Röser, 1983a, 1983b).

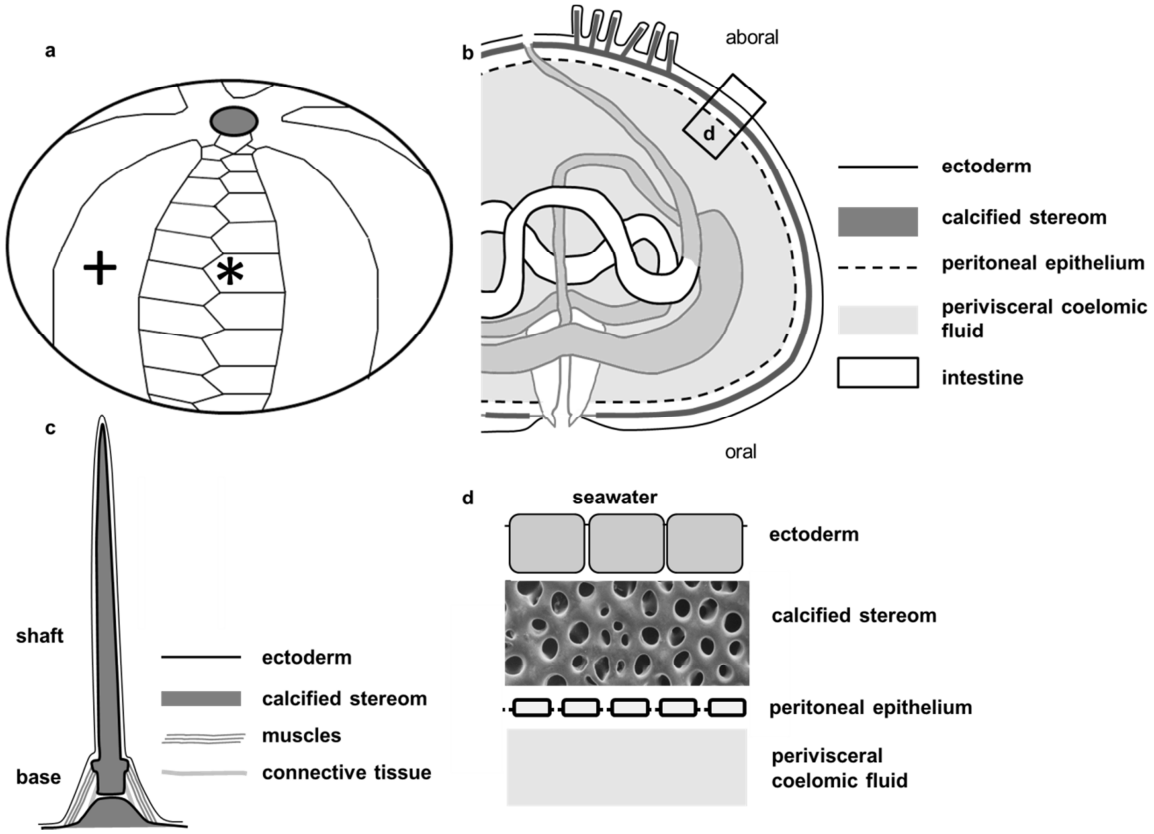

Figure 5 Schematic anatomy of sea urchins, (a) test structure; ambulacral plates are marked with + (tube feet are not shown), interambulacral plates are marked with *, grey circle: periproct; (b) arrangement of the digestive tract and alignment of the epithelia close to the calcified stereom (after Storch and Welsch, 2009); a close up is given in (d); (c) example for a spine, connected to a tubercle (after Heatfield and Travis, 1975).

Sclerocytes in ossicles and spines

Growth of adult sea urchin proceeds by an ossicle-production at the aboral section next to the periproct and by extension of the ossicle edges. In ossicles and spines, calcification is maintained by specialised cells, the so called sclerocytes. These cells form, comparable to PMCs, a syncytium that maintains an environment that favours calcification (Märkel and Röser, 1983b; Märkel, 1990). Their role has been studied in spine regeneration, and they have been shown to enfold newly built microspines (Heatfield and Travis, 1975). In older regions of the stereom the syncytium is broken down, but sclerocytes maintain contact with the stereom *via* filiform cytoplasmic processes (Märkel and Röser, 1983b; Märkel, 1990).

Ion transport and amorphous $CaCO_3$

In comparison to the knowledge about larval calcification, almost no work has been done to address processes related to adult calcification. However, in adult regenerating spines and growing teeth it has been shown that CA also plays a role in the adult calcification process (Heatfield, 1970; Chen and Lawrence, 1987).

Another similarity to larval calcification is the precursor phase of ACC which has been shown to occur as an intermittent phase in regenerating spines and in sea urchin teeth (reviewed by Killian and Wilt,

2008). Adult sclerocytes also exhibit large vesicles filled with granular, heterogeneous or membranous content (Heatfield and Travis, 1975). Whether these vesicles are Ca^{2+}-rich, remains unclear.

1.1.3.3 Amorphous calcium carbonate

In the previous subchapter, ACC, the precursor phase of Mg-calcite (Beniash et al., 1997; Addadi et al., 2003; Raz et al., 2003; Politi et al., 2004, 2008), was already introduced to be precipitated in calcification vesicles within PMCs (Beniash et al., 1999). Politi et al. (2008) defined three different stages of ACC in larval spicules: the 1st type is transient and can only be found in areas of fast growth and is rapidly transformed into the 2nd type which is "most abundant in fresh spicules" (Politi et al., 2008) and is transformed slowly into the 3rd type (biogenic calcite). As amorphous minerals are unstable (Addadi et al., 2003) they are stabilised by specialised matrix molecules (Aizenberg et al., 2003; Addadi et al., 2003; Raz et al., 2003).

1.1.3.4 Organic matrix

Biogenic minerals are not only made up of an inorganic mineral phase but also of an organic matrix which is located within the skeleton as well as on its surface. In sea urchin larvae carbohydrates and more than 40 proteins constitute the complement of integral matrix proteins (Benson et al., 1986; Swift et al., 1986; Ameye et al., 2001; Killian and Wilt, 2008). However, the matrix only accounts to 0.1% of the skeletal mass. 4-19% of these 0.1% are carbohydrates as components of N- and O-glycoproteins (Benson et al., 1986; Swift et al., 1986; Ameye et al., 2001). Processing of the PMC-specific matrix proteins SM30 and SM50 is known to occur in the Golgi apparatus (Ingersoll et al., 2003) and the location within the spicule is protein specific (Urry et al., 2000; Ingersoll et al., 2003; Wilt et al., 2008). Interestingly, some of the same matrix proteins can be found in both larvae and adults (Livingston et al., 2006; Killian and Wilt, 2008).

In addition, PMCs begin to secrete collagen at the blastula stage (Benson et al., 1990; Wessel et al., 1991). As it is known that the organic matrix is collagen-free (Benson et al., 1986) it is thought that the secreted collagen helps to structure development and spiculogenesis (Benson et al., 1990; Wessel et al., 1991).

1.1.4 Adult anatomy

In Figure 5b a cross section of an adult sea urchin is shown; only the gonads, pedicellaria and tube feet are omitted. In regular sea urchins, like *S. droebachiensis*, mouth and anus are lying in the oral-aboral axis (Figure 5b). As already introduced, sea urchins are characterised by a five-fold symmetry and the tube feet of their water vascular system penetrate the ambulacral plates. In the following only thesis-relevant aspects of the anatomy are presented.

The mesodermal ossicles (chapter 1.1.3.2) are lined by two epithelia: the external epidermis and the coelomic lining epithelium (from now on called peritoneal epithelium). The peritoneal epithelium is described as a columnar and flattened epithelium (Hyman, 1955; Barnes, 1980) and move the

perivisceral coelomic fluid (PCF) with its cilia. The PCF is in contact with the inner organs; however, "there is no conclusive evidence of a functional vascular circulation (…)" (Farmanfarmaian, 1966). The epidermis seem to absorb molecules and organic substances (summarised in Heatfield and Travis, 1975) and during spine regeneration it is responsible for Ca^{2+} uptake (Heatfield, 1970).

1.1.5 Digestion in adult sea urchin

The digestion system can be separated in the following parts: mouth, oesophagus, stomach, intestine and rectum. The mouth is located at the oral side and is characterised by five teeth of the Aristotle's Lantern. The oesophagus leaves the lantern and increases in diameter at the transition zone oesophagus-stomach. This segment turns counter clockwise within the body cavity and is characterised by a siphon. The intestine turns clockwise and passes into the narrow rectum which opens aborally (De Ridder and Jangoux, 1982).

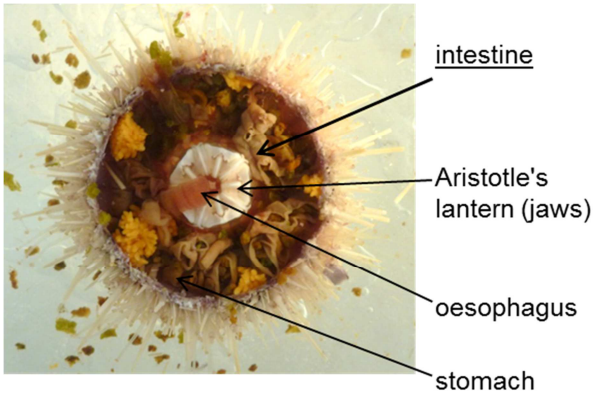

Figure 6 Horizontal section though an adult sea urchin (*S. droebachiensis*). The course of parts of the digestive system can be seen; the oesophagus derives from the Aristotle's lantern and pass into the stomach (red-brownish) which lies underneath the clockwise turned intestine (light brown). The yellow parts are residues of the gonads and fecal pellets lie around the sea urchin.

The intestinal epithelial barrier consists of four distinct layers: the luminal enterocytes with absorbing character (Tokin and Filimonova, 1977), connective tissue, circular and longitudinal muscle cells, and an outer epithelium (Boolootian, 1964). The thickness of the nutrient absorptive intestine has been shown to be dependent on food availability and ranged between 55 µm (starved) and 175 µm (fed) (Bishop and Watts, 1992).

TEM studies revealed a high density of mitochondria within the intestinal cells which points towards their function as an actively transporting epithelium (Tokin and Filimonova, 1977; Santos-Gouvea and Freire, 2007). Bacteria of the genus *Vibrio spp.* colonise the gut of sea urchins and are linked to anaerobic alginate digestion and seasonal N_2-fixation (Unkles, 1977; Guerinot and Patriquin, 1981; Sawabe et al., 1995).

1.2 Transport – transcellular and paracellular

In the following sections I will introduce principle mechanisms of ion transport across cell membranes and epithelia as the investigation of this was a main part of my thesis in both the adult and larvae studies. Furthermore, the concepts of the $Cl^-HCO_3^-$ ATPase and the $Na^+K^+2Cl^-$ cotransporter (NKCC) are introduced and discussed, as they are essential for the calcification model in sea urchin larvae.

1.2.1 Ion transport across cell membranes

Cell membranes separate the intracellular and the extracellular space and are impermeable for ions and macromolecules. In addition, they are tight for water whereas diffusible gases and lipophilic substances can pass. Ion gradients are established *via* the Na^+K^+ ATPase (stoichiometry: 3:2; intracellular high K^+, low Na^+) and transport of other ions is mediated by active or passive transport.

Primary active transporters utilise energy from ATP hydrolysis to transport ions against their concentration gradients. Cotransporters and ion exchangers allow the so-called secondary active transport and use the electrochemical driving forces established by primary active transport. By using the electrochemical gradient of one ion these proteins cotransport other ions against their gradient, *e.g.* NKCC (Dubyak, 2004). In contrast, passive transport is the flux of ions down their concentration gradient and is mediated by ion channels or carrier proteins. This form of transport is also dependent on electrochemical gradients.

Most animal cells are characterised by a resting membrane potential of ~ -80 mV which is maintained by the Na^+K^+ ATPase and is mainly dependent on K^+ conductances (Wright, 2004). However, the cell specific resting membrane potential may dependent on cell-specific intra- and extracellular ion concentrations and on distinct sets of ion channels, exchangers and transporters.

1.2.2 Epithelial transport

Epithelial cells are connected *via* cell junctions which tighten the paracellular cleft and separate the luminal compartment (*e.g.* intestine lumen) from the basolateral compartment (*e.g.* PCF). Analogous to transport across cell membranes, transport across epithelia is also dependent on the electrochemical driving forces, concentration gradients, and transepithelial potential (TEP).

In this thesis, I investigated transcellular and paracellular properties of adult sea urchin intestine and peritoneal epithelium.

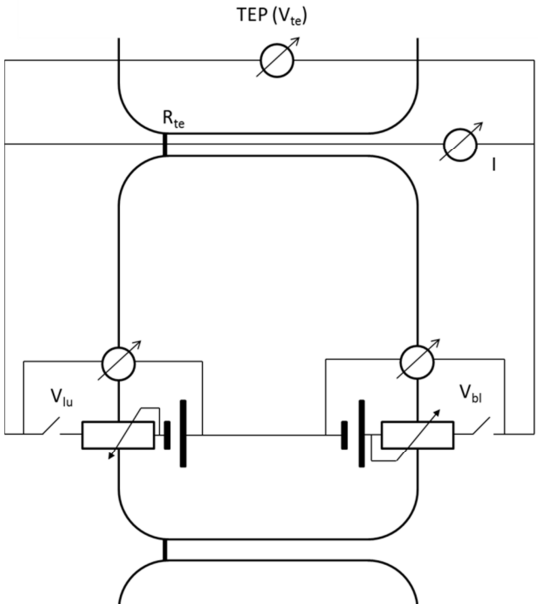

Figure 7 Electrical model for an epithelium. Luminal tight junctions separate the luminal and basolateral compartment. The transepithelial resistance (Rte) is the result of TJ resistance connected in parallel to the variable series resistances of the voltage sources. These voltage sources are the sum of transport molecules in each membrane which generate specific Nernst potentials and thus the respective membrane potential. Transepithelial potential (Vte) and current (I) are shown.

1.2.2.1 Transcellular transport

The polarisation of epithelia involves polarised distributions of ion channels, exchangers and transporters in the luminal and basolateral membranes. As shown in Figure 7, a transepithelial potential (TEP; V_{te}) will be established if transcellular transport generates different luminal and basolateral membrane potentials.

The transepithelial resistance (TER; R_{te}) is dependent on the resistance of both membranes and the paracellular resistance (see next section). Both parameters, as well as the resulting current, can be determined using the Ussing chamber technique.

1.2.2.2 Paracellular transport

Cell junctions tighten the paracellular cleft of epithelia and determine the permeability and selectivity in terms of charge and size of ions and molecules. Further, junctions maintain the polarised character of epithelia by preventing the intermixing of cell membrane constituents (proteins and lipids). Evolutionary, two groups of cell junctions can be determined: the septate junctions (SJ) which are characteristic for invertebrates and the tight junctions (TJ) which are characteristic for vertebrates (Furuse and Tsukita, 2006; Beyenbach et al., 2010; Figure 8). In addition, anchoring junctions (adherens junctions, desmosomes and hemidesmosomes) and communication junctions (gap junctions) are known (Banerjee et al., 2006).

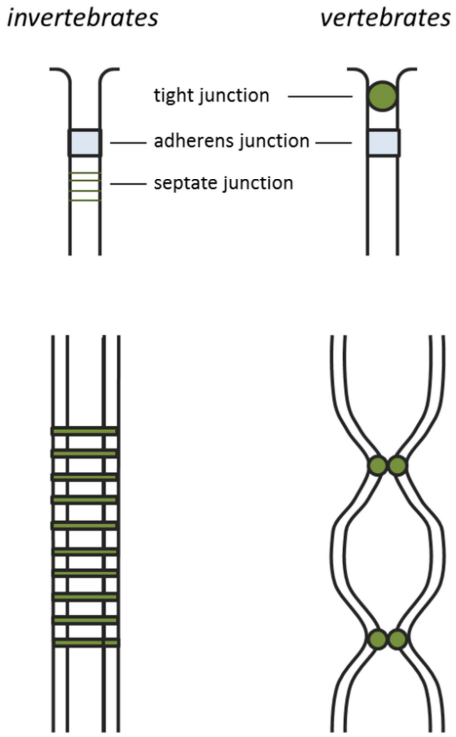

Figure 8 Septate vs. tight junctions. The upper schematic drawings show the overall structural appearance of septate (invertebrata) and tight (vertebrata) junctions. In the lower schematic drawing the differences of the paracellular cleft are given. In invertebrates the plasma membranes are in parallel and the SJ cross the constant cleft with septa, in vertebrates TJ form so-called kissing points (paired TJ) and tighten the space more. None of the drawings are to scale; after Furuse and Tsukita (2006).

SJ cross the constant paracellular cleft (15-20 nm) with ladder like septa (Lane et al., 1994; Furuse and Tsukita, 2006; Beyenbach et al., 2010; Figure 8). In contrast to the near-luminal localisation of the TJ, SJ are located below the adherence junctions but still luminally (Figure 8). In both junction structures, junction-forming proteins form a complex with cytoplasmic scaffolding proteins and are anchored within the cytoskeleton (Matter and Balda, 2003; Beyenbach et al., 2010). SJ's of *Drosophila melanogaster* have been investigated for their integral membrane protein composition and homo- and heterophilic adhesion molecules as well as two claudin-homologous proteins have been identified (Furuse and Tsukita, 2006). In TJ, claudins are known to be the most important proteins in the formation of homo- or heterotypic protein complexes bridging the paracellular cleft (Furuse and Tsukita, 2006). The expression of certain claudins in an epithelium determines its tightness and selectivity for certain charges (Günzel and Yu, 2013).

The electrical resistance of the paracellular pathway is dependent on the gate function of SJ or TJ for ions and is part of the R_{te} (chapter 1.2.2.1). When transcellular transport is inhibited diffusion potential measurements can be performed by changing the anion- and cation concentrations at one of the

epithelial sides (*e.g.* by reducing the luminal NaCl concentration) to determine whether the epithelium exhibits a relative cation- or anion permeability. In the given example, the paracellular cleft is characterised as cation-permeable if a lumen-positive V_{te} is generated. In addition, the size barrier function of the paracellular cleft can be determined by applying a fluorescent dye bound to dextran of a selected size.

SJ in echinoderms

Echinoderms possess two types of septate junctions. The first, more primitive junction, is called double-septum SJ and is found in the ectoderm of tube feet (Green, 1981). The second type is the anastomosing septate junction of endothelia where an anastomosing network is built by the septa (Green et al., 1979).

1.2.3 $Cl^-HCO_3^-$ ATPase

The current model for larval calcification includes a $Cl^-HCO_3^-$ ATPase whose existence has been widely discussed in the literature in the past, primarily in fish gills, exocrine secretion organs and kidney (*e.g.* Burg and Green, 1973b; Bornancin et al., 1980; Gassner and Komnick, 1981). Although until today no direct genetic evidence has been found for a Cl^- pump, it is still discussed as one potential mechanism for Cl^- transport (Gerencser and Zhang, 2004). These formerly described Cl^- ATPases are mostly Mg-dependent, present in mitochondria and plasma membranes and were thought to be inhibitable by loop diuretics (Burg and Green, 1973b; Bornancin et al., 1980; Gassner and Komnick, 1981).

It has been known for a long time that loop diuretics act as diuretics and saluretics (*i.e.* increase of renal water and salt excretion) in the kidney thick ascending limb of Henle's loop (TAL) but the target protein was not known. In the field of kidney research the effect of loop diuretics on Cl^- transport of the TAL was investigated and has been discussed controversially.

The transepithelial potential of TAL was measured under different conditions: i) control (identical ionic concentrations both basolaterally and luminally), ii) Na^+free solutions luminally (choline substitution) and iii) under the presence of either furosemide (1-300 µM), ouabain (1-10 µM) or ethacrynic acid (0.3-1 mM and 3-10 µM (ethacrynic-cystein)) (Burg and Green, 1973a, 1973b; Burg et al., 1973; Greger, 1981). Measurements of the TEP under control conditions revealed a lumen-positive potential (Burg and Green, 1973a, 1973b; Burg et al., 1973; Greger, 1981) which was interpreted as the proof that Cl^- is reabsorbed by a primary active transport *(i.e.* a Cl^- ATPase) (Burg and Green, 1973a, 1973b; Burg et al., 1973). Based on the seemingly independency of Na^+ free solution (Burg and Green, 1973b; Burg et al., 1973) and the decrease in TEP in the presence of loop diuretics, an inhibition of the assumed ATPase was favoured.

Greger (1981) improved the generation of Na^+ free solutions and could successfully reduce the Na^+contamination by performing a series of experiments where the Na^+free solutions were used first.

The results revealed a decrease in TEP. In a second series, Na^+free glass pipettes were used and decreased TEP even further. The results from both series suggested Na^+ dependent reabsorption of Cl^- which would be secondary active transport. In another study, a further K^+dependency was detected (Greger and Schlatter, 1981) and based on these findings the concept of a loop-diuretic sensible $Na^+K^+2Cl^-$ cotransporter (NKCC) was developed whereas the concept of a Cl^- ATPase has not been further pursued, at least in kidney physiology.

1.2.4 NKCC-cotransporters and their functions

NKCC belongs to the SLC12 family of electroneutral cation-coupled Cl^- cotransporters (Hebert et al., 2004). Within the family-nomenclature the two known genetically distinct isoforms NKCC1 and NKCC2 are called SLC12A2 (for NKCC1) and SLC12A1 (for NKCC2). In this thesis the nomenclature NKCC (1or 2) is used.

In mammals the occurrence of these two isoforms is tissue-specific: NKCC1 is broadly expressed and NKCC2 is kidney-specific (Xu et al., 1994; Payne and Forbush III, 1995; Haas and Forbush, 1998). Their homology at the protein level is known to be ~60% (Haas and Forbush, 1998); however, in a phylogenetic tree both isoforms are shown to be separated from each other (Figure 9). Both hydropathy profiles are similar and reveal an integral membrane protein with 12 putative transmembrane segments (Payne and Forbush III, 1995).

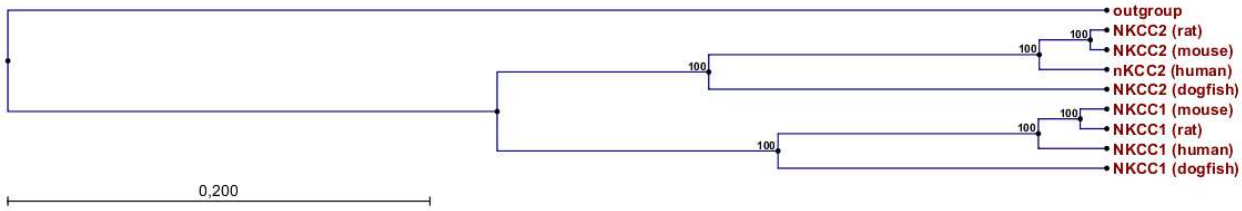

Figure 9 SLC12-family phylogenetic tree, protein level, calculated with UPGMA algorithm. The NKCC sequence of the tobacco hornworm (AAA75600) were used as outgroup, the other used NKCC isoforms derived from rat (NKCC1: NP_113986; NKCC2: NP_062007), human (NKCC1: NP_001037; NKCC2: NP_00032), spiny dogfish (NKCC1: AAB60617; NKCC2: AAM74966), and mouse (NKCC1: NP_033220; NKCC2: NP_899197.2). Numbers at the nodes show the bootstrap analysis result (100 bootstrap replicates), the scale shows the fraction of amino acid substitution. The tree was conducted in CLC Sequence Viewer (version 6.7; Aarhus, Denmark) as described later in chapter 2.7.1

The function of the cotransporter is dependent on the availability of Na^+, K^+ and Cl^- which are transported electroneutrally with a stoichiometry of 1:1:2, driven by the gradients for Na^+ and Cl^-. Furthermore, ammonium is known to be able to replace K^+ (Kinne et al., 1985; Loong et al., 2012). Reversible inhibition of both isoforms is performed with loop diuretics (*e.g.* furosemide, bumetanide and azosemide). The most effective loop diuretic to inhibit NKCC1 is azosemide, whereas NKCC2 is most effectively inhibited by bumetanide (Ecke et al., 1996; Warth et al., 1998; Greger, 2000).

1.2.4.1 NKCC1

Cells use this broadly expressed isoform for regulatory volume increase (RVI), cellular migration, cell proliferation and exocrine secretion (Payne and Forbush III, 1995; Haas and Forbush, 1998; Hoffmann et al., 2007; Haas and Sontheimer, 2010; Cuddapah and Sontheimer, 2011; Garzon-Muvdi et al.,

2012). Cellular volume regulation is mediated by inward transport of osmoregulatory ions and coupled water flux (Figure 10a). This mechanism is used in RVI and in cell migration where NKCC1 is located at the leading edge of the cell. For Cl^-secretion, the cotransporter is located at the basolateral membrane of the respective tissue (*e.g.* shark rectal gland, mammalian colon). Cl^- leaves the cell *via* luminal channels and generates a lumen-negative potential; Na^+ recirculates *via* the Na^+K^+ ATPase and diffuses towards the luminal compartment *via* the paracellular pathway, driven by the lumen-negative potential (Figure 10b).

Within the mechanism of cellular volume regulation the cotransporter can be activated *via* phosphorylation mediated by kinases, *e.g.* PKC and PKA. For activation, a rearrangement of the cytoskeleton caused by hypotonic shock is thought to be needed (reviewed by Hoffmann et al., 2007). The importance of a cytoskeleton rearrangement for NKCC activation has also been shown in sea urchin coelomocytes. The rearrangement of F-actin was blocked by phalloidin which prevented an increase of NKCC within the plasma membrane (D'Andrea-Winslow et al., 2001).

An essential involvement of NKCC1 within bone formation of rats has been shown by Bush et al. (2010): the chondrocytes need to increase their cell volume using NKCC1.

1.2.4.2 NKCC2

This isoform is exclusively expressed in kidney TAL. Here it is located at the luminal membrane and mediates NaCl reabsorption. Cl^- is further transported *via* basolateral channels; Na^+ follows the electrical gradient *via* the paracellular pathways and is actively extruded from the cells *via* the Na^+K^+ ATPase (Figure 10c).

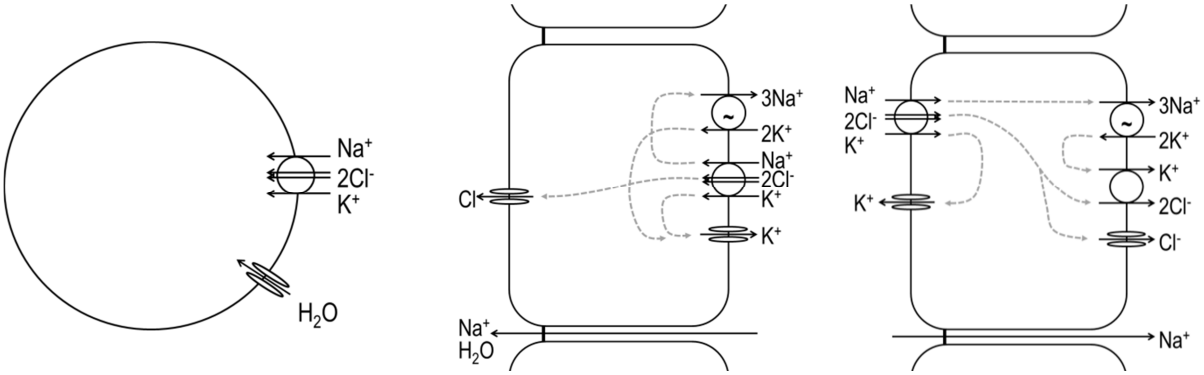

Figure 10

a) NKCC1 involved in regulatory volume increase (RVI) and cellular movement. Osmolytes are transported inside the cell and thus, water will follow passively *via* aquaporins. Note that other RVI-relevant transporters are not shown.

b) NKCC1 function in *e.g.* shark rectal gland. Cl^- is secreted *via* the basolateral cotransporter and a luminal located Cl^-channel. Due to potential differences Na^+ diffuse paracellularly and H_2O follows. Na^+K^+ ATPase and basolateral K^+ channels provide the driving force.

c) NKCC2 function in mammalian kidney TAL. Cl^- is taken up luminally and can be secreted to the blood side. K^+ is recirculated *via* a channel and Na^+ follows due to potential differences at the paracellular pathway or is extruded by the Na^+K^+ ATPase.

1.2.4.3 NKCC in sea urchins

The cotransporter has been shown to be present in adult petalloid coelomocytes of *Paracentrotus lividus*. These immune cells undergo a transformation caused by a rearrangement of the cytoskeleton when they reach a wound and transformation can be induced *via* a hypotonic shock. After transformation NKCC distribution is changed from hetero- to homogeneous and is located within the plasma membrane (D'Andrea-Winslow et al., 2001).

1.2.5 Ion transport inhibitors

Specific ion transport inhibitors can be used in different assays to investigate whether the respective ion transport is involved in the process of interest. One goal of this study was to investigate the contribution of different ion transporters mainly in the process of calcification.

1.2.5.1 Loop diuretics

Loop diuretics act on both isoforms of NKCC. The used loop diuretics furosemide, bumetanide and azosemide are sulfamoylbenzoic acid derivatives and share the feature of an acid group (furosemide and bumetanide: carboxyl group, azosemide: tetrazolate group) in the meta position (Figure 11; Greger, 1995). They reversibly block NKCC presumably by either binding in a translocation pocket of the molecule or by competing with the Cl^- binding site of the NKCC (Kinne et al., 1985; Isenring and Forbush, 2001; Somasekharan et al., 2012).

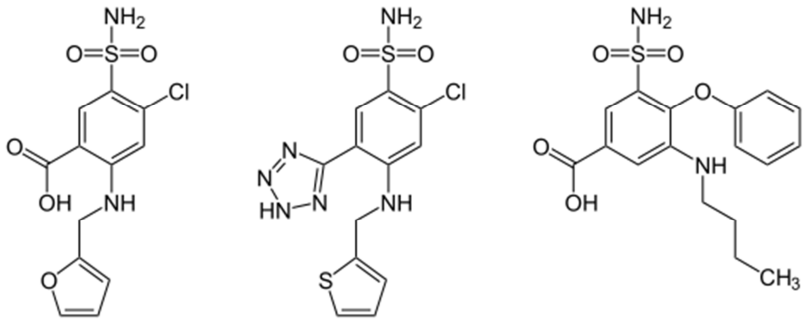

furosemide azosemide bumetanide

Figure 11 Structural formulas of the used loop diuretics.

1.2.5.2 Concanamycin A

Concanamycin A belongs to the group of plecomacrolide antiobiotics and is produced by *Streptomyces* sp. This antibiotic is known to inhibit the vacuolar-type ATPase (V-ATPase) at the nanomolar level (Dröse and Altendorf, 1997) and it can also act on the P-ATPases but at micromolar levels.

By inhibition of the V-ATPase the proton transport, directed away from the cytoplasm, towards the organelle lumen (*e.g.* lysosomes, trans Golgi network) is inhibited. As a result, processes as protein translocation and protein degradation are affected (Yoshimori et al., 1991; Muroi et al., 1993).

1.2.5.3 Cyclopiazonic acid

This substance is a myotoxin produced by *Aspergillus sp.* and *Penecillium sp.* and its inhibition of

SERCA-ATPases is known (Goeger et al., 1988; Inesi and Sagara, 1994). Isoforms of this ATPase can be found in various tissues in the endoplasmatic and sacroplasmatic reticulum where it is responsible for the refill of the intracellular Ca^{2+} stores.

1.2.5.4 DIDS

4,4´-diisothiocyanatostilbene-2,2´-disulfonate (DIDS) is known to inhibit most of the members of the SLC4 family (AE1-3, NBCe1 and NBCe2, NDCBE, NCBE-B). It is proposed that there is an interaction with a DIDS-reaction motif at the extracellular end of the fifth transmembrane segment (AE1 and NBCe1). In addition, for AE1 a covalent binding site for the isothiocyanate group is known (Romero et al., 2004; Alper, 2006).

Members of the SLC4 family are needed to transport HCO_3^- across the plasma membrane of various tissues for *e.g.*, intracellular acid-base homeostasis, CO_2 transport or cell volume regulation (Romero et al., 2004). For this, the different sub-groups can be defined due to the co-transported substrates: Cl^- HCO_3^- exchanger (AE), $Na^+HCO_3^-$ cotransporter (NBC) and $Cl^-HCO_3^-$ exchange (Na^+ driven) (NDCBE).

1.2.5.5 Omeprazole

The drug in its initial form cannot interact with the H^+K^+ ATPase. Activation can be achieved by a low pH (Morii et al., 1990; Peterson, 1997) with half-maximal activation at approximately pH 5.0 (Huber et al., 1995). After activation of the pro-drug the tetracyclic, planar sulphonamide can react with the H^+K^+ ATPases (Huber et al., 1995).

The inhibited ATPase is classified as a P-type ATPase (Huber et al., 1995; Beisvag et al., 2003) and is expressed in parietal cells (gastric acid secretion) and various other tissues responsible for acid-base homeostasis (Beisvag et al., 2003). Due to this task, protons are transported towards the extracellular cavity and potassium ions are transported towards the cytosol.

1.2.5.6 Verapamil

This Ca^{2+} antagonist inhibits voltage-gated L-type calcium channels. Thus, extracellular calcium cannot flow towards the cytosol which results in reduced contractility of cardiac muscles, a lowered blood pressure and vasodilation in humans (Elliott and Ram, 2011; Van Zwieten, 1998).

1.2.6 Cellular processes involved in pH homeostasis

1.2.6.1 General information

External pH (pH_e) of extracellular body fluids as well as the internal pH (pH_i) of cells have to be kept stable because of the sensitivity of physiological processes, enzyme performance and cell vitality to changes in $[H^+]$. Maintenance is done by the regulation of $[HCO_3^-]$ as well as the presence of non-bicarbonate buffers. In marine invertebrates, disturbances in pH_e can arise from metabolic processes

and changes in seawater carbonate chemistry, *e.g.* ocean acidification (chapter 1.3); pH_i is also decreased by metabolic acid load, proton transport towards the intracellular compartment, by export of HCO_3^- and by calcification in case of intravesicular calcification of PMCs (Equation 1).

$$Ca^{2+} + HCO_3^- \leftrightarrow CaCO_3 + H^+ \qquad \text{Equation 1}$$
$$Ca^{2+} + 2HCO_3^- \leftrightarrow CaCO_3 + CO_2 + H_2O$$

Active regulation

Intracellular and extracellular acid or base load is regulated with a defined set of ion exchangers and transporters (chapter 1.2.6) (Boron, 2004). An important transporter family is the SLC4 family (Romero et al., 2004) which comprises secondary active HCO_3^- cotransporters which use either Na^+ or Cl^- gradients as a driving force. The coupling on acid-base regulatory transport to actively maintained ion gradients in ion extruding organs (*e.g.* gills and digestive system) makes this mechanisms dependent on the metabolism and activity state of the respective organisms (reviewed by Melzner et al., 2009).

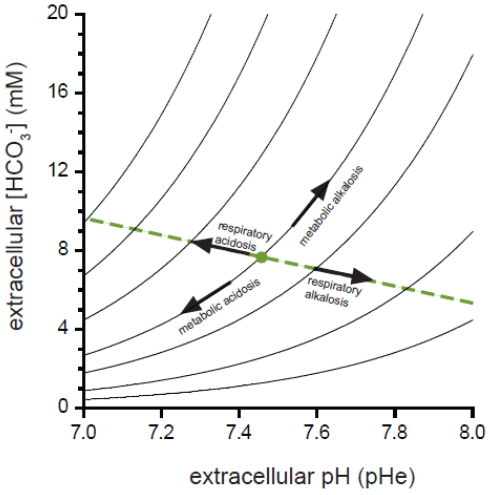

Figure 12 Davenport diagram. The dashed green line represents the non-bicarbonate buffer line which is steeper in active organisms compared to non-active organisms. The x-axis gives pH_e, the y-axis $[HCO_3^-]_e$ and the isobars gives the $(pCO_2)_e$. Starting from the physiological value (green point, species specific) changes of the acid-base status can be caused by metabolic or respiratory disturbances. Source: Melzner et al., 2009

Passive buffering processes

The relevant chemical groups of various non-bicarbonate buffers are protonated amino acid side chains, N-terminal alpha-amino groups or organic/inorganic phosphate groups (Melzner et al., 2009). The extracellular amount of these buffers is species dependent and their effectiveness can be visualised in a Davenport diagram (Figure 12). The non-bicarbonate buffer line is characterised by a negative slope, the steeper the slope the stronger is the buffer capacity of the non-bicarbonate buffers (Melzner et al., 2009). Active organisms with high metabolic rates (*e.g.* teleost fish, cephalopod molluscs) exhibit higher non-bicarbonate buffer values (steep non-bicarbonate buffer line) compared to non-active organisms (*e.g.* sea urchins) (summarised in Melzner et al., 2009).

1.2.6.2 pH compensation in sea urchin

The effect of ocean acidification on pH compensation in sea urchins will be introduced in chapter 1.3.2.

Intracellular pH

Intracellular pH regulation in sea urchin has been studied on larval PMCs. These cells experience a certain acid load due to calcification (Equation 1) which is assumed to be compensated *via* H^+ extrusion mechanisms. Only two studies measured the pH_i of PMCs either by the DMO (5,5-dimethyl-2,4-oxazolidinedione)-method or by microfluorimetry using BCECF (2′,7′-bis-(2-carboxyethyl)-5-(and-6)-carboxcarboxyfluorescein). Interestingly, in *S. droebachiensis* and *Hemicentrotus pulcherrimus* pH_i is maintained at 6.9 *via* a Na^+ and HCO_3^- dependent transporter and an H^+K^+ ATPase (Mitsunaga et al., 1989; Stumpp et al., 2012a).

Extracellular pH

Larvae of *S. droebachiensis* do not regulate their pH_e of the body cavity which is in equilibrium with seawater (Stumpp et al., 2012a). In contrast to this, adult sea urchins (*S. droebachiensis*) maintain their PCF at a pH of 7.5-7.7 (Spicer et al., 2011; Stumpp et al., 2012b). Adult sea urchins are characterised by low metabolic rates and most of the investigated species are characterised by low extracellular HCO_3^- (Spicer et al., 1988; Spicer, 1995; Miles et al., 2007; Spicer et al., 2011; Spicer and Widdicombe, 2012; Calosi et al., 2013; Table 1) which however is maintained at higher levels compared to seawater HCO_3^- (Spicer et al., 2011; Stumpp et al., 2012b; Table 1). The protein concentration of *S. droebachiensis* PCF is 0.28 mg ml^{-1} (Spicer et al., 2011).

Although it is generally believed that echinoderms are poor pH_e regulators their acid-base physiology has not been closely studied. And in contrast to this general hypothesis, recent work by Stumpp et al. (2012b) has shown that *S. droebachiensis* can regulate pH_e during long term incubation in elevated CO_2 (chapter 1.3.2). Understanding the underlying mechanisms was one goal of this thesis.

Table 1 Summary of acid-base status of the PCF in different echinoidea species at control conditions. Recent studies on Baltic *S. droebachiensis* show that the investigated animals had a higher control $[HCO_3^-]_{PCF}$ compared to other sea urchin species.

Species	$(pCO2)_{SW}$ (Pa)	$[HCO_3^-]_{SW}$ (mM)	pH_{SW}	$[HCO_3^-]_{PCF}$ (mM)	$(pCO_2)_{PCF}$ (Pa)	pH_{PCF}	Reference
Strongylocentrotus droebachiensis	69.1 ± 19.3	1.91	8.02	3.96 ± 0.68	160 ± 20	7.76 ± 0.06	(1)
	46.5 ± 4.8	1.99	8.00	5.33 ± 0.54	190 ± 20	7.76 ± 0.05	(1)
Psammechinus miliaris	52		7.96	1.8 ± 0.20	167*	7.4*	(2)
S. droebachiensis				2.63 ± 0.13		7.42	(3)
	46	1.2	7.89	1.96 ± 0.15	< 267*	7.46*	(3)
P. miliaris				2.5*	293*	7.10	(4)
Echinus esculentus				1.3*	120	7.05	(4)
P. miliaris				3.1*	190*	7.22*	(5)
Arbacia lixula				2*	640*	7.0*	(6)
Paracentrotus lividus				5*	1241*	7.24*	(6)

References: (1) Stumpp et al., 2012b, data from summer 2008 and 2010, given ± SD; (2) Miles et al., 2007, data given ± SD; (3) Spicer et al., 2011,freshly collected and experimental control data, given ± SEM; (4) Spicer et al., 1988 (5) Spicer, 1995; (6) Calosi et al., 2013, untreated field collected sea urchins; * values read from figures.

1.3 Ocean acidification

1.3.1 General information

In preindustrial times atmospheric CO_2 levels were at approximately 28.4 Pa. Due to the increase in anthropogenically emitted CO_2 (burning fossil fuels, deforestation) this level has increased to nearly 40.6 Pa until now (Figure 13). The world's oceans have taken up about 30% of the anthropogenically released CO_2 (Sabine et al. 2004, cited in Feely et al., 2004) thus leading to changes in their carbonate chemistry and acidification.

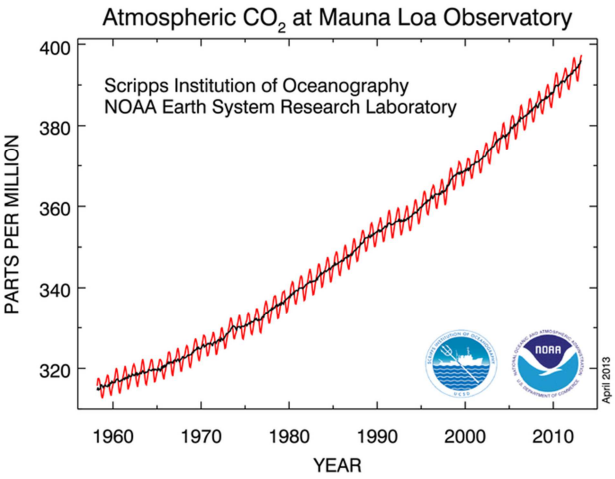

Figure 13 Full CO_2 measurements at Mauna Loa Observatory, Hawaii. The red line gives the mole fraction of CO_2 in dry air and the black line gives data corrected for the seasonal cycle. Source: http://www.esrl.noaa.gov/gmd/ccgg/trends/ (26.04.2013)

CO_2 dissolves in seawater and forms H_2CO_3 which further dissociates to HCO_3^- and H^+ (Equation 2, Zeebe and Wolf-Gladrow, 2001). The dissociation constants of the single steps depend on pressure, temperature and salinity.

The total amount of dissolved inorganic carbon (DIC) is the sum of all carbonate species and at a pH of 8.1, 90% of the oceans' carbon is present as HCO_3^-, 9% is present as CO_3^{2-} and 1% is present as CO_2 (Doney et al., 2009, Figure 14). The increase in dissolved CO_2 in the oceans causes an increase in protons and thus a decrease in pH. Furthermore, protons are buffered with CO_3^{2-} and thus the amount of HCO_3^- increases while CO_3^{2-} decreases (Figure 14). The average ocean pH has already declined by 0.1 units (Orr et al., 2005; Raven et al., 2005; IPPC, 2007) and it is thought that atmospheric CO_2 will reach values of 71-101 Pa until the year 2100 (IPPC, 2007) which would lead to a decline of average ocean pH by 0.3-0.5 units and a decrease in CO_3^{2-} concentration by ~50% (Orr et al., 2005). Proton concentration will be increased by a factor of 2-3 when these values are reached.

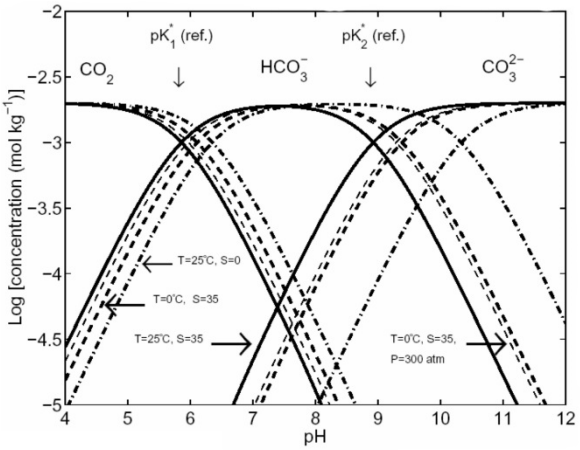

Figure 14 Bjerrum plot illustrating the carbonate system in seawater at different temperatures, pressures and salinities. The reference case is depicted with the solid line (T = 25°C, S = 35, P = 1 atm); DIC = 2 mmol kg^{-1} in all cases (source: Zeebe and Wolf-Gladrow, 2001).

$$CO_2 + H_2O \leftrightarrow H_2CO_3 \leftrightarrow HCO_3^- + H^+ \leftrightarrow CO_3^{2-} + 2H^+ \qquad \text{Equation 2}$$

Concurrent with the decline in pH is the decrease in the calcium carbonate saturation state (Ω). In general, $CaCO_3$ is present at different soluble phases; calcite and aragonite are the most common forms in seawater (Morse et al., 2007). The biogenic forms are produced by various marine invertebrates, *e.g.* sea urchins, bivalves, gastropods and corals. Calcite is abundant in two forms: low Mg-calcite (< 4% $MgCO_3$) and high Mg-calcite (> 4% $MgCO_3$). Depending on the amount of Mg^{2+} the solubility of calcite is lower or higher compared to aragonite (low Mg-calcite is less soluble) (Andersson et al., 2008).

As shown in Equation 3, Ω is dependent on the CO_3^{2-} concentration and the solubility product K_{sp} of either calcite or aragonite (dependent on temperature, salinity, pressure), $[Ca^{2+}]$ is closely related to salinity (Zeebe and Wolf-Gladrow, 2001).

$$\Omega = \frac{[Ca^{2+}][CO_3^{2-}]}{K_{sp}} \qquad \text{Equation 3}$$

Ω < 1 implies that the seawater is undersaturated and that the respective phase is vulnerable to dissolution (Andersson et al., 2008; Feely et al., 2004; Doney et al., 2009). Shells and skeletons are normally protected by external organic coatings or epithelia (Fabry et al., 2008; Doney et al., 2009). However, in contrast to other orders, the order of cidaroida (within the class echinoidea) is characterised by the absence of an epithelial cover on fully grown spines (Märkel and Röser, 1983b). In cidaroid sea urchins, a 60 day incubation in Ω-undersaturated conditions (Ω = 0.54, 290 Pa) resulted in dissolution (Ries et al., 2009; Table 2).

Depending on the environment, ocean acidification can have severe consequences for the ecosystem. Coastal zones, like the Kattegat in the Baltic Sea, belong to more affected regions as eutrophication induces hypoxia and enrichment in CO_2 (Feely et al., 2010; Thomsen et al., 2010; Waldbusser et al., 2011). Hypoxic and hypercapnic conditions in benthic environments are furthermore favoured due to a high degree of stratification and high primary production (Conley et al., 2007; HELCOM, 2009; Beldowski et al., 2010; Thomsen et al., 2010; Cai et al., 2011). Thus, organisms living in these regions are already experiencing acidic conditions and it can be assumed that adaption to variable carbonate chemistry conditions is already occurring.

1.3.2 Effects on calcification and acid-base homeostasis

It has been predicted that the shift in the carbonate system and the associated decrease in CO_3^{2-} will lead to decreases in calcification of calcifying organisms (Orr et al., 2005; Fabry et al., 2008). In several studies it has been shown that calcification is often negatively affected but that the reaction is species dependent. A broad-taxa study investigated the effect of long-term pCO_2 incubation (60 days, up to 290 Pa) on *e.g.* echinoidea, bivalves and crustaceans (Ries et al., 2009). In 10 of 18 investigated species net calcification was negatively impacted by increase in pCO_2, in 3 species it was positively

correlated, 4 species reacted in a parabolic response curve and calcification of 1 species was not affected.

Within echinoids, ocean acidification has been shown to have a negative impact on somatic and gonad growth and energy resource allocation of adult sea urchins (Shirayama and Thornton, 2005; Siikavuopio et al., 2007; Ries et al., 2009; Stumpp et al., 2012b; Table 2). However, in a meta-analysis, Dupont et al. (2010) showed that calcification and growth among several species of adult echinoderms were not negatively affected by ocean acidification whereas these traits were negatively influenced in developmental stages and juveniles.

Table 2 Summary of the %-reduction of growth and calcification in different sea urchin studies. Except of one study, growth of non-cidaroid sea urchins is negatively affected by hypercapnia and the skeleton of cidaroid sea urchin partly dissolves (see table caption for measured parameters).

Species	cidaroid/ non-cidaroid	Incubation time	pCO_2 (Pa)	Reduction	Additional notes	Reference
Strongylocentrotus droebachiensis	non-cidaroid	6 weeks	102	36%		(1)
			284	86%		
Hemicentrotus pulcherrimus	non-cidaroid	26 weeks	59	10-20%		(2)
Echinometra mathaei	non-cidaroid	26 weeks	59	20-35%		(2)
Eucidaris tribuloides	cidaroid	8.5 weeks	61	36%		(3)
			92	36%		
			290		dissolution	
Arabica punctulata	non-cidaroid	8.5 weeks	61		net-calcification was positive in all three CO_2 treatments	(3)
			92			
			290			

All reductions are in relation to the control value; (1) Holtmann et al. 2013 *accepted*; see also chapter 3.3.3.1, measurement of the increment in growth *per* day in ossicles, region aboral II; (2) Shirayama and Thornton, 2005, relative growth rate estimated from wet weight in juveniles; (3) Ries et al., 2009, estimations of net-calcification *per* day after normalisation to initial buoyancy weight.

With regard to the sea urchin skeleton, an increase in the brittleness of spines and test has been reported under long-term hypercapnic seawater conditions (Shirayama and Thornton, 2005; Siikavuopio et al., 2007; Miles et al., 2007; Findeisen *personal communication*).

Strongylocentrotus droebachiensis can regulate its pH_e during incubation under hypercapnic conditions (Stumpp et al., 2012b). The regulation took place *via* an increase in $[HCO_3^-]$ with an unknown uptake mechanism and on a different time scale compared to active organisms with a high acid-base regulatory capacity. Teleost fish, cephalopods or decapod crustaceans can reach a new steady-state of $[HCO_3^-]_e$ within 12-24 h after exposure to hypercapnic conditions (Larsen et al., 1997; Pane and Barry, 2007; Gutowska et al., 2010) whereas *S. droebachiensis* reached the new steady-state after 4 days (Stumpp et al., 2012b). Protein concentration, a possible additional buffer mechanism, is

known to be unchanged under hypercapnic conditions (Spicer et al., 2011).

Acid-base homeostasis in PCF means recruitment of HCO_3^- or removal of H^+. Theoretically, HCO_3^- can originate from the $CaCO_3$ stereom and any dissolution means consumption of H^+ and generation of HCO_3^-. Stereom dissolution and related release of HCO_3^- were hypothesised for hypercapnic associated short-term and studies (12 h to 8 days), as an increase in $[Mg^{2+}]_{PCF}$ and $[Ca^{2+}]_{PCF}$ of *Psammechinus miliaris*, *S. droebachiensis* and *Brissopsis lyrifera* has been shown (Miles et al., 2007; Spicer et al., 2011; Spicer and Widdicombe, 2012). However, Catarino et al. (2012) rejected this hypothesis based on their results on *P. lividus* after 19 day incubation in 54-236 Pa. Mg:Ca ratio of PCF were higher compared to seawater concentrations but did not change between the different treatments. Their results further indicate an unknown compensatory mechanism of pH_{CF} based on the fact that pH_{CF} was higher compared to pH_{SW} in some individuals of the lowest pH_{SW} treatment. Another recently published study further supports the hypothesis that pH_{CF} is actively compensated and not based on stereom dissolution: $[Ca^{2+}]_{PCF}$ and $[Mg^{2+}]_{PCF}$ did not change significantly in two sea urchin species (*Arbacia lixula* and *Paracentrotus lividus*) exposed to a naturally high CO_2 area (155 Pa) for 4 days (Calosi et al., 2013).

In contrast to > 1 day exposures to hypercapnia it has been shown that emersion - like intertidal species experience - can lead to shell dissolution and $[HCO_3^-]$ increase in bivalves and echinoderms to buffer increased organic acids (*e.g.* Akberali, 1980; Jokumsen and Fyhn, 1982; Spicer et al., 1988).

Another source for HCO_3^- could be the digestive tract since digestion is predominantly mediated by fermentation, *e.g.* CO_2 production, and could deliver HCO_3^-. However, not much is known about the involvement of the digestive tract in acid-base regulation. Based on the high density of mitochondria within the intestinal cells it is assumed to actively transport (Tokin and Filimonova, 1977; Santos-Gouvea and Freire, 2007).

In conclusion and as introduced in chapter 1.2.6, pH homeostasis of the extracellular body fluids can be modified by ocean acidification. To better understand the mechanisms of pH_e regulation in *S. droebachiensis* was one goal of this study.

1.4 Research hypotheses

In my thesis I worked on the membrane physiology of larval and adult sea urchins: I examined the cellular mechanisms involved in larval calcification and the processes underlying HCO_3^- accumulation in the coelomic fluid of adult urchins during exposure to hypercapnic seawater conditions. In the subsequent thesis sections I will separate the discussion of these two life stages, except in the description of the materials and methods.

1.4.1 Cellular mechanisms involved in larval calcification

As pointed out in the introduction, the existing cell model for larval calcification (Figure 4) and its pharmacology are discussed controversially. Based on new pharmacological understanding and inhibitor concentration profiles I worked on the following hypotheses:

(1-a) One of the calcification supporting transport molecules in larval sea urchins is the $Na^+K^+Cl^-$ cotransporter.

Based on my finding that NKCC is involved in the process of calcification the following two hypotheses were developed and address the question of NKCC action (see chapter 4.1.4 and 4.1.5 for the development of hypothesis):

(1-b) ACC-rich vesicle production can still occur in the presence of azosemide and NKCC is involved in concentration of ACC within these vesicles which would lead to smaller vesicles with lower calcium content in the presence of azosemide.

(1-c) NKCC is involved in cellular migration and volume regulation and therefore interacts with the location of primary mesenchyme cells within the body cavity and with the formation the cytoplasmic cord.

In addition to the specific question on NKCC action within larval calcification I further addressed the question if the remaining proposed transporters in whole larvae assays could be confirmed on *S. droebachiensis* larvae and if previously reported toxic side effects on development can be reduced by lower concentrations.

To proof the existence of some of the reported transport proteins I applied previously published sea urchin inhibitors against L-type Ca^{2+} channels, DIDS-sensitive anion transport (SLC4-family), H^+K^+ ATPase, and further used inhibitors against a Ca^{2+} ATPase and V-ATPase which might also be involved in calcification related processes. The last hypothesis was formulated as the following:

(1-d) Non-loop diuretic inhibitors are successful in inhibiting the calcification process in sea urchin larvae and previously reported toxic side effects are diminished in accordance to the use of low drug concentrations.

1.4.2 Mechanisms for an increase in the buffer capacity of the coelomic fluid and effects of ocean acidification on skeletal elements of adult sea urchins

I investigated both epithelia which are in contact with the PCF with respect to their involvement in acid-base regulation: the intestine and the peritoneal epithelium. The following hypotheses were developed:

(2-a) The peritoneal epithelium does not form an effective barrier and thus the stroma is not separated from changes in acid-base status and ionic conditions of the coelomic fluid (e.g. undersaturated conditions during the first 4 days of hypercapnic exposure).

(2-b) The intestine is involved in acid-base regulation and transports HCO_3^- towards the PCF.

To understand more about the dissolution patterns and their potential contribution I examined the stereom and addressed the following hypotheses:

(2-c) The inner stereom of sea urchins ossicles dissolves during acute exposure to hypercapnic conditions and contributes slightly to an increase in $[HCO_3^-]_{PCF.}$

(2-d) If dissolution takes place in animals during hypercapnic treatments, their stereom (ossicles and spines) will become instable for fracture forces.

Stumpp et al. (2012b) showed that growth, measured as test diameter, decreased. However, whether ossicle growth at hypercapnic conditions still occurs is not known yet. If so, newly formed sections of the ossicles could differ in their ultrastructure compared to ossicle sections mineralised under control conditions. These skeletal sections could be thinner and compromise the stability of the skeletal structure.

(2-e) If ossicle growth occurs under hypercapnic conditions the newly formed sections will have a changed morphology.

2 Material and Methods

2.1 Animal maintenance, spawning and cultivation

2.1.1 Adult sea urchins

Adult sea urchins (*Strongylocentrotus droebachiensis)* were collected at different time points and at two different locations. In June 2010, the RC Littorina collected adult individuals *via* dredging for the CO_2 perturbation experiments at subtidal depth (17 m) in the Kattegat, Western Baltic Sea (56°21´N, 11°19´E). For the investigation of the peritoneal properties in the adults, individuals were collected at subtidal depth (25 m) in the Kattegat, Western Baltic Sea (55°34'N, 12°24'N) with the RC Ophelia in March 2010. The parental adult individuals used in the larval experiments (2011 and 2012) were collected by divers in the Oslo fjord near Drøback, Norway (in December 2010 and January 2012).
In all cases, the sea urchins were transported to the cooling facilities of the GEOMAR, Kiel, Germany. There, they were maintained in a recirculation aquaculture system (total water volume ~800 l, pH 8.0, $[NH_4^+]$ maintained < 0.05 mM) which was equipped with a protein skimmer, bacterial filter and an UV-lamp. The Kiel fjord seawater (54°20'N, 10°9'E) was set to a salinity of 31.5 by adding sea salt SeequaSal (Münster, Germany) and was allowed to equilibrate for at least 12 hours before it was used to exchange water in the recirculation system. Depending on the batch of adult sea urchins, the cultivation temperature varied: 8.5°C (fertilisation season 2011), 5°C (fertilisation period 2012), and 9-11°C for the adult experiments. The animals were fed *ad libitum* with *Fucus* sp. and, in part, *Mytilus edulis*.

2.1.2 Maintenance during CO_2 perturbation experiments

CO_2 pertubation experiments on adult sea urchins were performed by Meike Stumpp at the Wadden Sea Station Sylt of the Alfred Wegener Institute for Polar and Marine Research and are described in detail in Stumpp et al. (2012b). The collected skeletal elements were used in this study for further investigation.

The animals were incubated at control conditions (10°C) for at least one week prior to the start of the experiment. They were calcein-labelled for 48 h (100 mg l^{-1}; C0875, Sigma-Aldrich, Germany) at 10°C in six tanks with aeration prior to the CO_2 incubation. CO_2 levels (47, 102 and 284 Pa) were achieved by equilibrating experimental aquaria with an air/CO_2 gas mixture generated by a central automatic gas mixing-facility (Linde Gas, HTK Hamburg, Germany) with a ventilation rate of 0.8 l min^{-1}. Before and after the CO_2-incubation period, morphometric parameters (individual test diameter) were quantified and at the experimental end (after 41-45 days) the tests were cleaned, dried, stored in the dark and were available for my experiments.

2.1.3 Spawning and larval cultures

Spawning was induced in adult sea urchins by injection of 0.5 M KCl in FSW (0.2 or 0.3 µm filtered seawater) into the perivisceral coelomic fluid (PCF). Eggs were collected in 50 ml Falcon tubes, sperms were obtained by pipetting.

After washing with FSW, the eggs of one female were fertilised with sperms of one male (1:100,000 dilution) and were gently reared (60 rpm) until they were incubated in FSW in a 1 l Erlenmeyer flasks at a density of 10 larvae ml^{-1}. The flasks were aerated and gently mixed with single air bubbles. In both larval-seasons, the cultures were maintained in a dark cultivation fridge at 10°C (Dinkelberg analytics, Germany). Temperature, salinity and pH were monitored (10.6 ± 0.02°C, salinity 31.4 ± 0.1, pH 8.1 ± 0.01; n = 254-262). The larvae were fed neither during the cultivation nor the experiments except when they were grown up to the juvenile stage for 60 days. Then the larvae were fed with *Rhodomonas* sp.

At day 5, 400-1000 ml of the larvae cultures were fixed with two different methods: for Western Blot and PCR the larvae were concentrated, shock frozen in liquid nitrogen and stored at -80°C. For using larvae in immunohistochemistry, they were pre-fixed in 4% PFA (Paraformaldehyde, dissolved in FSW, pH 8.4) for 15 min and then fixed in ice-cold Methanol for 1 min. Storage was done in 70% Ethanol at -20°C.

2.2 Inhibitor studies

These studies were conducted on larvae in FSW.

2.2.1 Experimental setup

All inhibitor-incubations were conducted in sterile 24-well plates (Nunc Multidishes Nunclon™ Δ, flat bottom, with lid, polystyrene; Germany) with FSW. The end volume was set to 2 ml and 20 larvae were incubated in each well. Incubations were started at three different time points corresponding to different larval stages; points in time, incubation duration and used concentrations are summarised in Table 3 and Table 4. The final vehicle concentration (DMSO or deionised water) was ≤ 0.1% and a vehicle control was performed.

Omeprazole had to be acid-activated before usage: the stock solution was diluted in ¼ of the final volume (pH 5.0) and after 20 min in the dark the volume was filled to the final and pH was adjusted to pH 8.0. Stock solutions of all inhibitors were diluted 1:1000 and were allowed to acclimatise in FSW overnight (10°C) before the experiment started. This led to incubation pH's between 7.97 (omeprazole) and 8.06 (verapamil).

Incubations were stopped by PFA-fixation (4% paraformaldehyde, FSW, pH 8.4) at day 3 (52 h old gastrula stage) or at day 5 (120 h old pluteus larvae). Descriptions of further analysis are given later in this section.

Table 3 Summary of the time points of incubation, the used inhibitors and which parameters have been analysed. Concentrations of the respective inhibitors are given in the text. FSW: filtrated seawater, scale bars are 50 µm (blastula, gastrula and prism stage), 100 µm (pluteus) and 500 µm (juvenile).

time point of incubation	duration of incubation	time point of fixation	analysed inhibitors	year	analysis of	incubation medium
28 h postfertilisation, blastula stage 	24 h	52 h postfertilisation, gastrula stage 	azosemide, inhibitors 2012	2011 2012	gastrulation	FSW
28 h postfertilisation, blastula stage 	92 h	120 h postfertilisation, pluteus larvae 	loop diuretics	2011	calcification (qualitative analysis); morphometrics (azosemide)	FSW
47.5 h postfertilisation, gastrula stage 	72.5 h	120 h postfertilisation, pluteus larvae 	azosemide	2011	calcification (qualitative analysis); morphometrics (azosemide)	FSW
72 h postfertilisation, prism stage 	48 h	120 h postfertilisation, pluteus larvae 	all inhibitors	2011 2012	primary body rod (length, width, calcein incorporation); morphometrics	FSW, calcein-FSW (only azosemide)
72 h postfertilisation, prism stage 	24 h	96 h postfertilisation, early pluteus larvae 	azosemide	2012	calcification vesicle (presence, size, RFU); PMC-flipodial network	calcein-FSW (only azosemide)
72 h postfertilisation, prism stage 	max. 60 days	60 days, juvenile 	azosemide	2012	development	FSW

2.2.2 Inhibitors used in larval calcification experiments

A summary of all used inhibitors, their IC_{50} in various tissues and cells and the maximal used concentration in comparison to my results is given in Table 20. A condensed summary about the target proteins, literature based maximal concentrations and all used concentrations in this study are given in Table 4 .

Table 4 Information about inhibitors used in this study. The target proteins, max. concentrations from the literature and concentrations used in this study are listed.

inhibitor	inhibition of	literature values for max. concentrations (µM)	concentration used in this study (µM)
furosemide	NKCC1	500 [1,2]	50; 200; 500
bumetanide	NKCC1	100 [1,2]	1; 10; 20; 50; 100
azosemide	NKCC1	100 [1,2]	1; 10; 20; 50
concanamycin A	V-ATPase	1 [3]; 0.05 [4]	0.005; 0.01; 0.05; 0. 1
cyclopiazonic acid	Ca^{2+} ATPase (intracellular Ca^{2+} storage sites)	10 [5]	1.5; 3; 15; 30
DIDS	anion exchange *via* SLC4-family	200 [6]	0.5; 1; 5; 10; 20
omeprazole	H^+K^+ ATPase	300 [7]; 10 [8]	2; 25; 50; 100; 200
verapamil	L-type Ca^{2+}channel	10 [9]; 100 [10]	5; 10; 25; 50

[1] Ecke et al., 1996; [2] Warth et al., 1998; [3] Muroi et al., 1993; [4] Nishihara et al., 1995; [5] Uyama et al., 1992; [6] Pappone and Lee, 1995; [7] Mattsson et al., 1991; [8] Morii et al., 1990; [9] Matsuoka et al., 1991; [10] Tambutté et al., 1996.

2.2.3 Investigation of larval development, morphometrics, vitality and swimming behaviour

In some of the described experiments azosemide was used as the loop-diuretic representative.

2.2.3.1 Incubation time: blastula until gastrula

Gastrulation was qualitatively evaluated for azosemide and non-loop diuretics. The length of gastrula, gastrocoel and archenteron was measured (Figure 15a) and GaJ% (the proportion of archenteron elongation into the blastocoel along the animal-vegetal axis during gastrulation; Harkey and Whiteley, 1980) was calculated from gastrocoel and archenteron length.

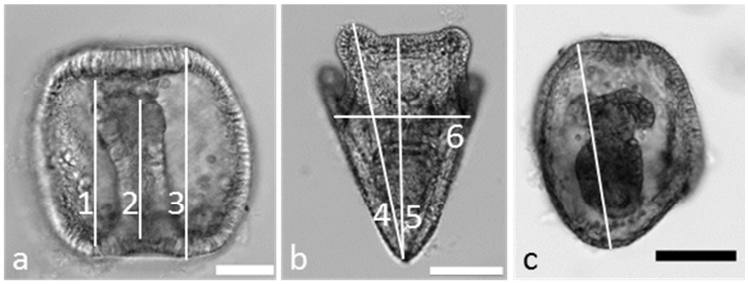

Figure 15 Exemplary pictures of the morphometrics measurements of (a) gastrulation (gastrocoel length (1), archenteron length (2), gastrula length(3)), (b) antero-lateral length (4), body length (5) and width (6) in pluteus larvae (4) and (c) measurement of the antero-lateral length in prism stages. Scale bars: 50 µm for (a), 100 µm for (b) and (c).

2.2.3.2 Incubation time: prism until pluteus

The morphometrics of larvae were measured in frontal pictures of 120 h old larvae in ImageJ. The following parameters were obtained: body length, antero-lateral length and body width as shown in Figure 15b. A ratio was calculated from the antero-lateral and body length (antero-lateral/body length). In prism stages and in pluteus larvae, whose growth was severely affected, the antero-lateral length was measured as shown Figure 15c. Due to not well developed post-oral arms in some inhibitor treatments this parameter was not measured in the investigated larvae.

2.2.3.3 Vitality, swimming behaviour and further development

Vitality of larvae incubated in one of the used inhibitors was qualitatively determined *per* well before fixation following this scheme: (--) dead, (-) inactive/immobile, describing larvae lying to the well bottom, (+) mobile to immobile, describing a state which larvae lying and other larvae swimming, and (++) actively swimming. Dead larvae were distinguished from inactive larvae by their shape: inactive larvae were still shaped like larvae, dead larvae started to lose their larval shape. Swimming behaviour of control and 50 µM azosemide larvae was measured in 120 h old larvae (7 larvae/fertilisation, n = 4-5). Videos (6000 frames) were taken with a digital 5 megapixel colour microscope camera (DFC 450c, Leica Microsystems, Germany) mounted on a stereomicroscope (M165C, Leica Microsystems, Germany). Videos were converted using the "Free Video Converter" (Extensoft) and were imported to ImageJ (version 1.47b). Afterwards, videos were cropped and modified by applying a threshold. This had to be done to obtain black and white pictures for the analysis with the multitracker plugin (captured pixel sizes: 5-25). Movement was measured in arbitrary units (pixels).

Some fertilisations were raised for more than 5 days in the 2 ml incubation wells. They were provided with food (*Rhodomonas* sp.) and fresh water and were monitored for further development.

2.2.4 Measurement of calcification

2.2.4.1 Growth in body rod length

Incubation stages: blastula/gastrula until pluteus

PFA-fixed larvae of five azosemide-experiments were used for this analysis (four larvae *per* experiment). After transferring them to FSW (with 0.1% albumin coated pipettes) pictures were taken with a CoolSNAP-HQ2 (Photometrics, USA) digital camera system mounted on a microscope (Axio Observer.D1, Zeiss, Germany) using MetaFluor (Visitron, Germany). Frontal and lateral pictures of the larvae were taken with transmission and polarised light. All pictures were taken with binning 1 and with a 10x objective. The scaling of the pictures was performed with the freeware program ImageJ (version 1.44p).

Due to the lack of measurable body rods, the analyses were performed qualitatively by introducing categories: (1) normal growth: three normal grown rods, (2) abnormal growth: no classification of the rods possible, (3) no rods: only polarised structures (dots) visible, (4) no skeletal structures: no polarised structures (Figure 16).

Incubation stages: prism until pluteus

The larvae of these experiments (all inhibitors) were handled as described before. In contrast to the previously explained procedure, the body rod of these incubations was developed in all larvae and thus, its length was measured using ImageJ. When IC_{50} values were calculated a nonlinear fit using a logistic model (Equation 4) was used (OriginPro 8G SR4; OriginLab Corporation, Northampton, USA).

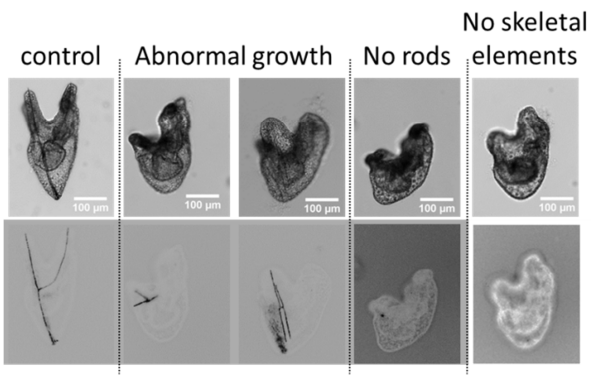

Figure 16 Exemplary pictures of the four categories introduced for skeleton abnormalities. The pictures result from 92 h incubations to azosemide (blastula until pluteus stage). The upper row shows transmission light pictures, the lower row are polarized light pictures with inverted colour and adjusted contrast and brightness to clearly visualise the skeleton (black).

$$y = \frac{A_1 - A_2}{1 + (x/x0)^p} + A_2 \qquad \text{Equation 4}$$

A_1 = initial value, A_2 = final value, x = any value at the x-axis, x0 = calculated IC_{50}, p = power

2.2.4.2 Growth in body rod girth

The larvae used for this measurement were incubated in control-FSW or FSW plus 50 µM azosemide at the age of 72 h (calcein labelled FSW, see later). After 48 h incubation, the larval tissue was

digested using the following protocol: washing 5x in FSW, 2x in 1 M $NaHCO_3$ (pH 8.6, in deionised water; modified after Okazaki and Inoué, 1976), and 1x 3.8% NaOCl (domol "Hygiene-Reiniger", Germany). In the last washing step the larvae were rinsed with a pipette. The spicules were allowed to settle and were photographed with a digital camera system (CoolSNAP-HQ2 (Photometrics, USA) mounted on a microscope (Axio Observer.D1, Zeiss, Germany) using MetaFluor (Visitron, Germany)) with binning 2 and with a 20x objective. The thickness of the body rod region 20 µm above the tip was measured afterwards using ImageJ.

2.3 Fluorescent dyes used in larval and adult experiments

2.3.1 Calcein

Calcein is a fluorescein derivative which fluoresces when Ca^{2+} or other twice positively charged metal cations are present (Wallach et al., 1959). In sea urchin research, this fluorescence marker is often used to tag mineralised parts in individuals to determine calcification or movement patterns (*e.g.* Lamare and Mladenov, 2000; Dumont et al., 2004; Wilt et al., 2008). When calcein is used for staining, active calcification is necessary during the marking period as calcein does not stain already established mineralised material. However, it is unclear how this dye is incorporated into the growing $CaCO_3$ skeleton.

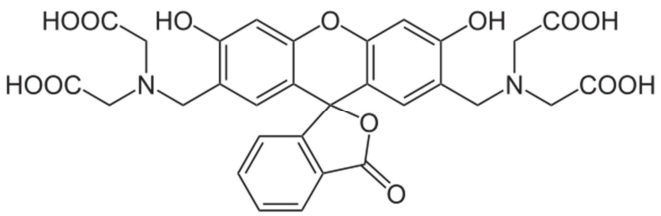

Figure 17 Calcein structure.

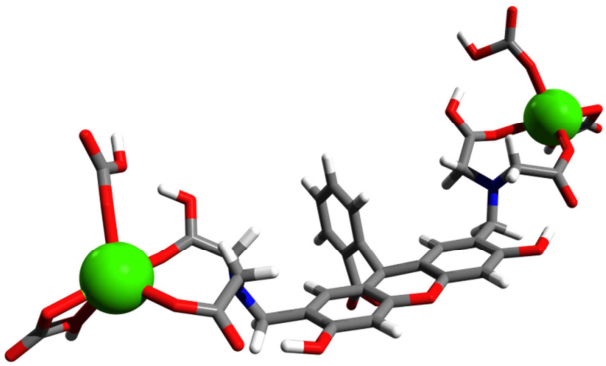

Figure 18 Calculated structural model of the binding HCO_3^-, Ca^{2+} and calcein. The calcein-binding pockets for Ca^{2+} are developed by the deprotonated carboxyl groups. The electrical minimum of the conformation was calculated with Gaussian 09 (Frisch et al., 2009) using the calculation level of B3LYP/6-31+G** at vacuum conditions. Dark grey = carbon, red = oxygen, blue = nitrogen, light grey = hydrogen, green = calcium.

Calcein has four carboxyl-groups which can act as binding sites for Ca^{2+} (Figure 17). At seawater pH 8, two of six possible oxygen-ions are deprotonated (pKa: 2.1, 2.9, 4.1, 5.4, 10.1 and 12.0 (Iritani and Miyahara 1973, cited in Ueberfeld et al., 2001)). By a quantum chemical calculation (see below) it could be shown that calcein binds Ca^{2+} primarily by its carboxyl groups (Figure 18); an additional binding of the amine nitrogen is possible but less favourable in energetic terms under vacuum conditions. The residual Ca^{2+} ligand sites were saturated by HCO_3^- anions. Hydrogen bonds are stabilising the conformation of the calcein as well as the HCO_3^- ligands. Thus, it is likely that calcein could both serve as a chaining within the crystal and it could be attached to Ca^{2+} at the outer edges of the crystal.

Quantum chemical calculation

To elucidate the binding geometries of the calcium calcein complex, quantum chemical calculations using Gaussian 09 (Frisch et al., 2009) where performed. For this purpose, geometry optimisations of a complex consisting of one twice deprotonated calcein, two calcium cations and four HCO_3^- anions were carried out on a DFT level of theory (functional: B3LYP, basis set: 6-31+G**) under vacuum conditions. The resulting structure is shown in Figure 18. This calculation was conducted under vacuum conditions. Thus, solvent and crystallographic effects were neglected just as effects of the organic matrix.

2.3.1.1 General staining and visualising procedure

After two hours, inhibitor- or vehicle-preincubated larvae were transferred to FSW-calcein (100 mg l^{-1}, 160 µM; product no.: C0875, Sigma-Aldrich), with either DMSO or azosemide (same concentrations as in preincubation). The pH of the calcein-FSW was adjusted to pH 8.0 by adding 0.32 mM $NaHCO_3$ *a priori*. All pictures of the latter explained analysis were taken with a CoolSNAP-HQ2 (Photometrics, USA) digital camera system mounted on a microscope (Axio Observer.D1, Zeiss, Germany) using MetaFluor (Visitron, Germany) (binning 1 or 2; excitation 488 nm (320 ms exposure time), Fluo-4 ET-filter (dichroic T495LP, ET 525/50 nm).

2.3.1.2 Calcein incorporation within the body rod of sea urchin larvae

Larvae (prism stage) were calcein-incubated in either control FSW (+0.1% DMSO) or FSW with 50 µM azosemide for 48 h as described. For the analysis the spicule length with incorporated calcein within the body rod was measured as well as the mean intensity of the whole body rod (ImageJ). The relative fluorescence value was corrected for background fluorescence and normalised to 100 μm^2.

2.3.1.3 Calcein incorporation within PMC-vesicles

Larvae (prism stage) were incubated in calcein-FSW enriched with DMSO or 50 µM azosemide as described. After 24 h incubation, so-called bag fractions were isolated, with slight modifications to the method described by Harkey and Whiteley (1980). 5-10 Larvae were transferred to 100 µl FSW and were washed in CMFSW (Ca-Mg-free seawater, Table 7) (3x). Afterwards, the larvae were washed 1-2x in dissociation medium and 3x in bag fraction isolation medium (Table 7). Immediately afterwards, the larvae were washed 3x in FSW. With this method, it was possible to remove the ectodermal cells in a way that the basal lamina ("bag") still remained (Figure 19) but with partial invisible ruptures. Based on these, the not-skeletal-bound calcein within the "bag" could diffuse out and the calcein-stained vesicles within the PMCs were visible.

Pictures of three larvae *per* experiment were taken at a magnification of 20x and 100x. PMCs were identified by their location and size: they had to be in contact with the spicules and exhibit an appropriate diameter (8 µm). Other cells within the bag could not be assigned to any defined cell type. Vesicles of PMCs along the body rod were prioritised but - especially in larvae from the azosemide

treatment - PMCs of other rods were analysed in addition. The pictures were scaled with ImageJ and the diameters of the PMCs and vesicles, as well as the relative fluorescence intensity of the vesicles were measured. Background fluorescence intensity was measured and subtracted from the gained vesicle-intensity.

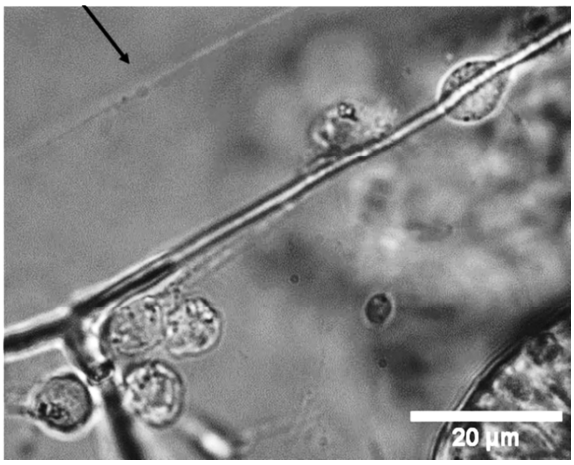

Figure 19 Example of isolated bag fractions. The arrow marks the basal lamina defining the bag.

2.3.1.4 Growth measurements in adult test

Calcein staining is described in chapter 2.1.2 and dissection of the ossicles is explained in chapter 2.5.1. Pictures of the longitudinal ossicle areas were taken at binning 1 and with a 20x objective. Longitudinal and latitudinal growth *per* ossicle was measured in ImageJ (version 1.44p) by measuring the distance between two calcein-marked bands at the growing edge which then was divided by 2. In some ossicle pairs growth measurements were not possible. To classify these measurements, three categories were introduced: (1) growth: calcein was incorporated during the staining phase and two lines (one *per* ossicle) were distinguishable; (2) no growth: a calcein signal was visible but could not be separated into two lines. Thus, growth was set to zero and was included in the analysis. (3) No labelling: no calcein signal along the growing edges was detectable. These ossicles were excluded from the analysis.

2.3.2 Membrane staining with FM® 1-43

The nontoxic FM® 1-43 membrane probe (N-(3-triethylammoniumpropyl)-4-(4-(dibutylamino) styryl) pyridinium dibromide), obtained from Life Technologies GmbH, Germany) was used to stain cell membranes of larvae and adult sea urchin.

2.3.2.1 Larval application

96 h old larvae (control-FSW and 50 µM azosemide-FSW) were stained with 20 $x10^{-6}$ M FM® 1-43 after 24 h incubation in 0.1% DMSO or 50 µM azosemide. For this, the larvae were scratched with a fine needle (hypodermic-needle, 0.4x20 mm, Fine-Ject®, Germany) next to the mouth and incubated in

FM® 1-43 for 3-5 minutes at 10°C. With this procedure a sufficient amount of dye was loaded into the larvae to stain plasma membranes. The larvae were transferred to an objective slide and a few cotton filaments served as spacer between slide and coverslip. The PMC-/SMC-filopodia and the cytoplasmic sheaths were visualised confocally using a LSM510 (Zeiss, Germany) (excitation 488 nm; HFT 488, LP 505). With this analysis, a qualitative determination, if the cytoplasmic cord and filopodia were visible, was possible.

2.3.2.2 Adult application

The peritoneal epithelium was stained with the same concentration to visualise the integrity after dissection. After transfer to a microscope slide, 1 µm z-stacks were performed with the same setup as used for the larval application.

2.4 Epithelial properties

2.4.1 Ussing chamber

Many epithelia (*e.g.* colon rectal gland of sharks, fish gills) secrete or resorb ions to maintain physiological conditions. Electrogenic transport can be measured in an Ussing chamber (chapter 1.2.2): a dissected epithelium (clamped to an insert) separates two chamber halves which can be perfused independently (Figure 20).

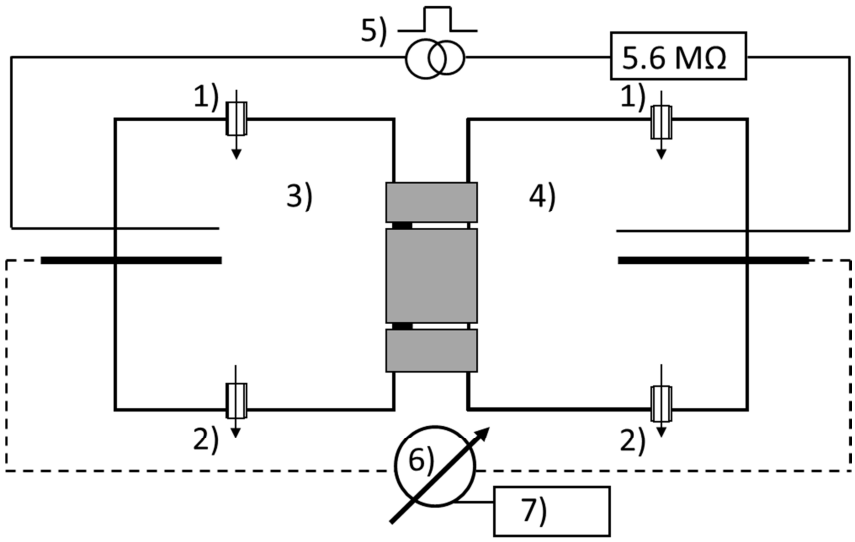

Figure 20 Schematic Ussing chamber with epithelium. 1) inflow for solutions, 2) outflow, 3) luminal chamber side, 4) basolateral chamber side, 5) pulse injection, electrodes in the extension, 6) voltmeter, electrodes in the extension, 7) chart recorder.

The Ussing chamber measurements in this study were performed under open circuit conditions (current clamped to zero, voltage changes due to transporting properties are measured). The basolateral side was defined as the reference side and a continuously applied current pulse (ΔI = 1.41 µA) was applied to the luminal side and resulted in voltage deflections (ΔV_{te}). After subtraction of ΔV_{te}' (deflections measured with the empty chamber) the transepithelial resistance (R_{te}, Ωcm^2) can be

calculated from voltage deflections using Ohms law (Equation 5).

$$R_{te} = \frac{\Delta V_{te} - \Delta V_{te'}}{\Delta I} \qquad \text{Equation 5}$$

If the investigated epithelium is characterised by electrogenic transport, the transepithelial potential (V_{te}) is unequal to zero and a lumen positive or lumen negative potential (referred to the basolateral side) can be measured. The equivalent short circuit current (I'_{sc}, µA $(cm^2)^{-1}$) is calculated using Ohms law (Equation 6) and is defined as the current when voltage is clamped to zero (short circuit).

$$I'_{sc} = \frac{V_{te}}{R_{te}} \qquad \text{Equation 6}$$

The definition for basolateral and luminal in the used tissues was the following: the luminal side of the peritoneal epithelium was the area which originally faced PCF; the luminal side of the intestine was the area which originally faced the intestinal lumen.

2.4.1.1 Dissection of the peritoneal epithelium

To characterise the electrical peritoneal properties a dissection method was developed. The peritoneal epithelium is rather thin and fragile, thus it was not possible to simply cut and transfer it to the Ussing chamber insert.

Sea urchins with an averaged diameter of 3.4 ± 0.1 cm (n = 39) were cut along the ambulacral plates and the inner organs were carefully removed. The outer part of one interambulacral plate was fixed on plasticine and, under the visual control of a dissection microscope (Carl Zeiss, Germany), the peritoneal epithelium of the area aboral II (ossicles 4-6, counting started aborally) was dissected.

The first approach comprised of placing a fine wire (120 µm in diameter) underneath the peritoneal epithelium. When the ring-shaped wire was in place, superglue (UHU super-glue; Germany) was placed around the wire until the epithelium and wire were connected. Immediately after gluing, the epithelium was rinsed with ice-cold seawater to remove waste glue. The frame of superglue was cut from the remaining epithelium with forceps-tips. The isolated peritoneum (plus the wire) was transferred to the insert (circular area of 0.78 mm^2) which was clamped between both Ussing chamber halves. The insert was equipped with additional silicone at the contact area (better sealing qualities). The whole procedure lasted 12 min on average. During this time, the remaining skeletal parts were stored in ice-cold seawater.

After perfecting this procedure, the wire was omitted from the dissection (Figure 21). The remaining part of the described protocol was adopted and the resistance measurements of the epithelium were of better quality.

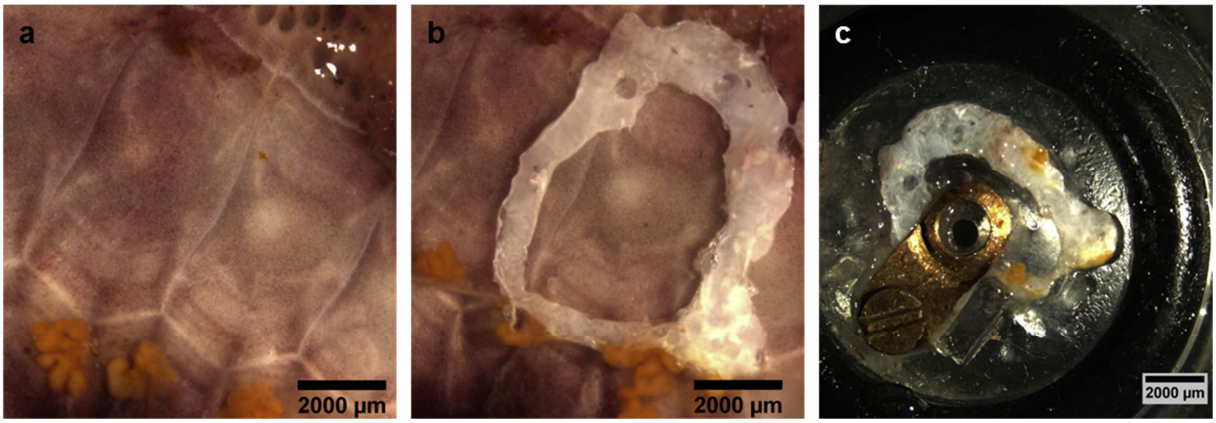

Figure 21 Dissection of the peritoneal epithelium. (a) inner part of the sea urchin test, (b) frame of superglue which is transferred to the Ussing chamber insert (c).

2.4.1.2 Dissection of the intestine

Seventeen sea urchins were cut horizontally at their largest diameter and the intestine was dissected carefully under water using forceps and surgical scissors. The average diameter of the sea urchins was 3.5 ± 0.1 cm (n = 14). The intestine was transferred to ASW enriched with 10% $MgCl_2$, to paralyse the peristaltic movements, and a melted pipette tip was inserted into the intestine lumen. The intestine was cut longitudinally using a scalpel and was clamped into an Ussing chamber insert with a circular exposed area of 0.07 cm^2.

2.4.1.3 Transepithelial resistance measurements

Ussing chamber measurements were performed in a continuously perfused and temperature controlled system (chamber volume 1.8 ml) (*e.g.* Mall et al. 1998).

Peritoneal epithelium

The transepithelial resistance was measured in 39 peritoneal epithelia at 12°C as described above with a flowing rate of 5 ml min^{-1} (ASW recipe see Table 6). In addition, fluorescein isothiocyanate (FITC)-dextran conjugates of different molecular sizes (4, 10, 40, 150 and 500 kDa dextran, Sigma-Aldrich, Germany) or fluorescein sodium salt (0.376 kDa, Sigma-Aldrich, Germany) were applied to the luminal side to confirm epithelial integrity (chapter 2.4.2).

Intestine

The transepithelial resistance, voltage and the short circuit current (I'_{SC}) of the intestine was measured in 17 animals according to the described method at 10°C (ASW recipe see Table 6).

The intestine was allowed to acclimatise to the experimental conditions for at least 6 min under the given conditions before drugs or solution changes were applied. In order to pharmacologically test for the presence of an electrogenic member of the SLC4 family within the epithelium 50 µM DIDS (basolateral and luminal) were applied after 14-48 min. This drug was dissolved in DMSO at a final concentration of 0.1%. In some experiments FSK/IMBX (0.1 µM/100 µM) or 100 µM ATP were applied basolaterally to stimulate V_{te} and 5 mM glucose was applied luminally. Diffusion potential

measurements were performed in the presence of low NaCl-ASW solution (Table 6) on either the luminal or basolateral side. This value was measured 50 s after application of the solution and used to estimate the paracellular selectivity properties (chapter 1.2.2.2).

2.4.2 FITC dextran measurements

In adult sea urchins the integrity and diffusion properties of the peritoneal epithelium was determined by applying fluorescein isothiocyanate (FITC)-dextran conjugates of different molecular sizes or fluorescein-sodium salt on the luminal side. Dissection, mounting to the Ussing chamber and used dextran-sizes was previously described in chapter 2.4.1.

Fluorescein is a negatively charged dye which is used in determination of the barrier function of the paracellular pathway in epithelia (Matter and Balda, 2003). For this, the dye is applied at the luminal side and the fluorescence of basolateral samples is measured after specified time intervals (excitation and emission wavelengths: fluorescein sodium salt: excitation 460 nm, emission 515 nm; FITC-dextran: excitation 490 nm, emission 520 nm).

Stock solutions of the dye (10 mg ml^{-1} for FITC-dextran conjugates, 0.1 mg ml^{-1} for fluorescein sodium salt) were prepared in artificial seawater (ASW) and all FITC-dextran solutions were dialysed overnight in artificial seawater in MWCO-dialysis tubing (MWCO of 2000 and 12000, obtained from Sigma-Aldrich, Germany; MWCO of 8000-10000 obtained from Roth, Germany) to remove potential detached fluorescein molecules.

Before the measurement started, Ussing chamber flow was stopped, the agar bridges were removed and the bath volume was increased to 2 ml. A background sample (200 µl) was taken on each side simultaneously and the volume was refilled simultaneously as follows: basolateral 200 µl of ASW and luminal 200 µl of one particular FITC-stock solution. Immediately after adding FITC to the luminal side, a start sample ("0 min") was taken followed by additional 200 µl samples every 30 min. In case of tissue damage, the basolateral signal was already increased in the 0 min-sample and the measurement was stopped. The baths were covered with aluminium foil during the experiment.

The samples were measured immediately after sampling in a 96-well plate (Fluoronunc™/Luminunc™, untreated, non-sterile, black from Nunc, Germany) with a Tecan Genios (Tecan Group Ltd., Switzerland) using an 485/20 nm excitation filter and a 535/25 nm emission filter. The number of flashes was set to 10 and all samples were measured at a gain of 45. The data (relative fluorescence units) were normalised to the starting molarity of FITC.

After 90 min, the experiment was stopped and the epithelium was examined visually for integrity under the dissection microscope. Only intact epithelia were accepted for analysis.

2.4.3 HCO_3^- permeability of the intestine

Diffusion permeability of HCO_3^- was measured in the intestine. For this, the concentration of HCO_3^- on the basolateral side was raised to 284 mM HCO_3^- (Table 6) (no water flow, slight bubbling of the

chamber halves, 5% CO_2 basolateral, 0.03% CO_2 luminal). HCO_3^- concentration of the luminal side was measured every 5 min during the first 30 min and at 30 min intervals for the following hour (Corning 965, calibrated with 0 and 10 mM $NaHCO_3$, accuracy 0.1 mM).
The HCO_3^- flow rate was calculated using Equation 7.

$$Js = \frac{\Delta C}{\Delta t} V \qquad \text{Equation 7}$$

Js is the flow rate, $\Delta C/\Delta t$ the change of HCO_3^- concentration over time and V the chamber volume (2 ml). The corresponding permeability coefficient (P) was determined by using Equation 8:

$$P = \frac{Js}{S\Delta C'} \qquad \text{Equation 8}$$

S is the surface area of the monolayer and $\Delta C'$ is the concentration differential of HCO_3^- across the monolayer.

2.5 Scanning electron microscopy

2.5.1 Sample dissection and preparation

To determine the effect of hypercapnia on the surface of adult sea urchin skeletons, the ossicles and spines of the animals from the CO_2-experiments were prepared for a scanning electron microscopy analysis. Ossicles and spines of 6-12 adult individuals *per* CO_2 treatment were analysed. The growth of these animals was previously measured with the described calcein-method.
The interambulacral plates of sea urchins were divided into three zones: the aboral I (ossicle 1-3), aboral II (ossicle 4-6) and oral zone (ossicle 10-13) (counting started aborally). Ossicles (length: 4.07 ± 0.19 mm and width: 2.47 ± 0.10 mm, n = 9) from the region aboral II were dissected under visual control (dissection microscope, SZ40, Olympus, Germany) with scalpels by cutting the adjacent ossicles. They were bleached in 3.8% NaOCl (domol "Hygiene-Reiniger", Germany) either overnight (13 h) or for 1 min (light shaking) and washed 2x in distilled water for 5 min. Thereafter, they were dehydrated (2x 70%, 1x 80%, and 2x 96% ethanol), 5 min *per* step. After air-drying (at least one day), each ossicle was mounted on double-sided adhesive tape on SEM-stubs with the coelomic-side facing upwards and then plated with gold-palladium. The different bleaching times had no influence on the surface structure of the ossicles and served as a method to remove remaining organic parts within the stereom.
Spines whose resistance was previously measured (chapter 2.6.3) were prepared in a similar way for the SEM analysis. The base was cut with a scalpel and this area was glued to the SEM-stubs (double-sided adhesive tape). Afterwards, spines were bleached for 30 s and washed in distilled water and were transferred through an ascending ethanol series (2 min each step). The following procedure was

similar to the one described for the ossicles.

2.5.2 Pictures and analysis

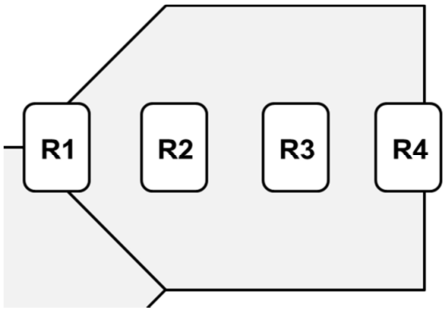

Figure 22 SEM-analysed regions of single ossicles. Within each region one area was magnified to characterise the ossicle surface as smooth or pitted.

All pictures were taken with a CamScan-CS-44 SEM at different magnifications.

2.5.2.1 Ossicles

Along the horizontal line four regions *per* ossicle were defined (Figure 22). *Per* region a highly magnified area was characterised for their ossicle surface (smooth or pitted). The pitted structures were characterised by a rough surface with granular structures. The diameter of these granular structures was measured in six high magnification pictures (30 structures were measured in an area of 20 μm^2). The percentage of smooth or pitted structures *per* CO_2 treatment or digestive system filling was calculated, respectively.

Furthermore, the longitudinal growing edge of the ossicles was analysed in terms of differences between old and new built stereom. To investigate any changes of the parts grown under the experimental conditions, the measured increment of growth of a respective sea urchin was applied for the investigated ossicle of the same individual.

2.5.2.2 Spines

The outer surface of spines was characterised by smooth or dissolved structures and the appearance of one of those structures was noted and the percentage appearance *per* CO_2 treatment was calculated for 6 spines *per* treatment. Furthermore, the thickness of spines and their radially arranged septa was measured in ImageJ.

2.6 Measurements of mechanical resistance of adult skeletal elements

To determine the resistance to an applied force of single ossicles, ossicle junctions and primary spines, a TA-XT2 texture analyser (stable micros systems LTD., UK) was used and the tests of CO_2-incubated sea urchins were dissected as described previously (chapter 2.5.1).

2.6.1 Single ossicles

Single ossicles (length: 4.2 ± 0.1 mm, width: 2.8 ± 0.03 mm, n = 67) were isolated as described previously. For measurement, they were placed in a fixture: the force metering needle (2 mm diameter) perforated the sample through a 3 mm diameter hole at the bottom plate at a speed of 1 mm s^{-1}.

2.6.2 Ossicle junctions

For analysis of the ossicle junctions, two connected aboral ossicles (length of dissected pieces: 5.3 ± 0.1 mm, width: 4.7 ± 0.1 mm, *n* = 62) were separated from the interambulacral plate under visual control. The dissected pieces were placed on a piece of neoprene with the coelomic side upwards. The force metering needle was placed upon the latitudinal junction connection between two ossicles and the measuring speed of the needle was set to 1 mm s^{-1}.

2.6.3 Primary spines

Primary spines were dissected under visual control from the tests by gently breaking them with scissors, holding their base (Figure 5c). For measurement of spine hardness, the spines were placed on styrofoam and the indenter (2 mm in diameter) was placed on top of the spine, next to the base. The measurement speed was set to 1 mm s^{-1}. A maximum of three primary spines were measured *per* urchin and spine hardness was averaged *per* urchin. Furthermore, only measurements of spines within the length classes 5-8.6 mm were used for the further analysis. This was due to the length differences between the different CO_2 treatments (control: 8.6 ± 0.1cm, *n* = 80; intermediate: 8.5 ± 0.2 cm, *n* = 85; high: 7.1 ± 0.1 cm, *n* = 55).

Before and after the measurement they were photographed with a CCD-camera (ProgRes®CF, Jenoptik, Germany) which was mounted on a stereomicroscope (WILD Heerbrugg) using ProgRes®CapturePro 2.7.7 (Jenoptik, Germany).

2.7 Molecular biology

The following nomenclature of *S. purpuratus* and *S. droebachiensis* specific sequences or transporters is used in the following text: *sp*- and *sd*-, respectively are used as a prefix.

2.7.1 Identification of NKCC-sequences

Three *sd*-NKCC associated transcriptome reads of 2- and 6-day old larvae (Findeisen, Stumpp, Melzner, *unpublished*) were identified when the *sp*-NKCC sequence (NM_001113236.1, Ji et al. 2008; Tu et al., 2012) was blasted (blastn) against the transcriptome database. These reads and the *sp*-NKCC nucleotide sequence were used to create primer pairs for RT-PCR.

Protein sequences (NKCC1 and 2) of human, mouse, rat, spiny dogfish, tobacco hornworm and sea urchin were aligned with CLC Sequence Viewer (version 6.7; Aarhus, Denmark; gap cost = 10, gap extension cost = 1, and end gap cost = as any other). Phylogenetic trees were calculated in CLC Sequence Viewer (version 6.7) using the UPGMA-algorithm (unweighted pair group method using arithmetic averages) and 100 replicates for a bootstrap analysis and the NKCC sequence of the tobacco hornworm was used as an outgroup.

Furthermore, the *sp*-NKCC nucleotide and protein sequence (NM_001113236.1 and NP_001106707 respectively) and the *sd*-sequence product 4 and 6 were used to identify sea urchin NKCC in the EST library of *S. purpuratus* using either blastn 2.2.27+ or tblastn 2.2.27+ (Zhang et al., 2000; Altschul et al., 1997).

2.7.2 Reverse-transcription PCR

Primer pairs for this method were generated using NCBI Primer-Blast (Ye et al. 2012). All three transcriptome reads, the *sp*-NKCC sequence and the sequence information of *sd*-NADH dehydrogenase subunit 5 (DQ917076.1; Addison and Pogson, 2009) were used as templates (Table 5). Shock frozen larvae (day 1 and day 5; stored at -80°C) were treated according to the RNeasy® Micro or Mini Kit protocol (Qiagen, Germany) to extract total RNA. RNA was eluted and the RNA amount was measured using a NanoDrop 1000 spectrophotometer (PeqLab Biotechnology GmbH, Germany). 1 µg RNA was translated to cDNA *via* a reverse transcription reaction (QuantiTect reverse transcription, Qiagen). The samples were stored at -80°C until usage.

Each mastermix was mixed according to the instruction manual (Fermentas, ThermoScientific Molecular Biology, Germany) with 1 µl template, 0.5 µl primer (forward and reverse), 2.5 µl dNTPs and DreamTaq buffer, 17.75 µl RNA-free water and 0.25 µl DreamTaq polymerase.

Table 5 Summary of the used primer pairs. All sequences are given in 5'->3' direction. Primers written in italics are generated with transcriptomal reads or sequence information of *S. droebachiensis* (see Figure 23 for their location), the rest is based on sequence information of *S. purpuratus* (NCBI Reference Sequence: NM_001113236.1, Ji et al., 2008; Tu et al., 2012). The 8th primer pair is a combination from NKCC1_3 rev and NKCC1_7 fwd (reverse complement sequences). Nad5 is based on the *sd*-NADH dehydrogenase subunit 5 (NCBI Reference Sequence: DQ917076.1; Addison and Pogson, 2009).

Primer No.	Primer forward	Primer reverse
NKCC1_1	AGATACGACACGCCACCATC	CCATCTGGGCATCGTAGTCC
NKCC1_2	TTGAGATACGACACGCCACC	GGAGAAGATCAGCCCGATGG
NKCC1_3	*GTCGCTCTCCTGCTAAGGATATG*	*CCTTTGCAGCTTTAGCCTCTG*
NKCC1_4	CGGTCATCTGCGTAGGAGTC	ATGGACCAACGCTGTGGATT
NKCC1_5	AGAGAAACTGGAGTGCCTGC	TTCCTGGGCATCGGTAGAGA
NKCC1_6	GTTGGTTTCTCGGAGACGGT	CCAGCCTGGTGACTTTGCTA
NKCC1_7	*AACGCCAAGGAATCCACCTC*	*GCGTTCAGTCTGCCTGAGAT*
NKCC1_8	*CAGAGGCTAAAGCTGCAAAGG*	*GAGGTGGATTCCTTGGCGTT*
NKCC1_9	*ATGATGCCCAGAAGGCCATC*	*GTCTTGATGACGGAGCCGAT*
NKCC1_10	*CTATGGGCCATCCTCATCTCC*	*CTGGTCAATAGAGGGCGTGA*
nad5	*GAACTACCCGAAACGATGCC*	*TAAACACTCCGGCGACTACC*

A no-template control was conducted. PCR was performed in a mastercycler, epgradient S (Eppendorf, Germany) under the following conditions: activation of DreamTaq polymerase (fermentas, Germany) at 94°C for 3 min, each PCR run was repeated 35x at 94°C for 30 s, 56°C for 30 s and 72°C for 3 min. An electrophoresis was conducted in a 1.8% agarosegel containing SYBRsafe DNA gel stain (Life

Technologies GmbH, Germany) at 120 V, 500 mA and 150 W for 45 min. The used PCR ladder was GeneRuler 100 bp Plus DNA ladder (Fermentas, Germany).

The products of the primer pairs 3, 4, 5, 6, 7, and 8 were used for an additional sequencing step (performed by Seqlab, Gernany). For this, the amount of product was amplified by repeating the PCR reaction with the gained product. The product was cut off the gel and cleaned according to the protocol of PCR-clean up NucleSpin® (Machery-Nagel GmbH & Co, Germany).

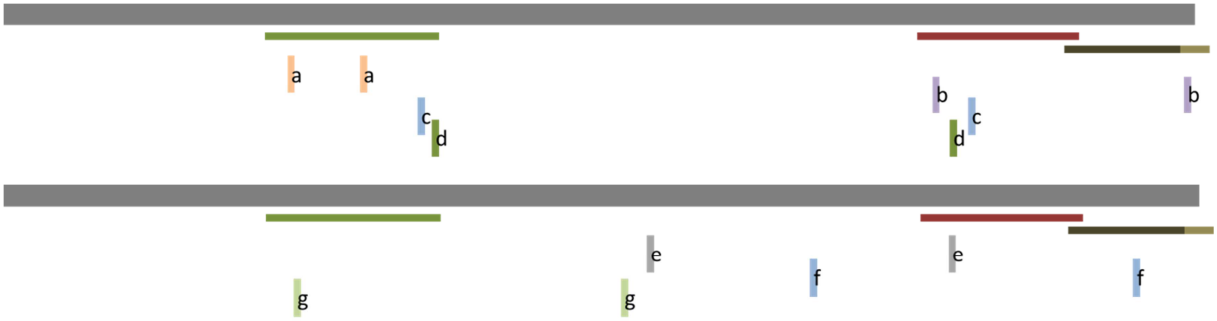

Figure 23 Localisation of three transcriptomal reads (green, red, olive) and NKCC primers in relation to the *sp*-NKCC (in grey; NCBI Reference Sequence: NM_001113236.1, Ji et al., 2008; Tu et al., 2012). The primers of the upper picture were generated with the *sd*-transcriptome reads, the lowers with the *sp*-NKCC sequence. a = NKCC1_3, b = NKCC1_7, c = NKCC1_9, d = NKCC1_10, e = NKCC1_4, f = NKCC1_5, g = NKCC1_6. Localisation was conducted with CLC Sequence Viewer, version 6.7.

Translation of nucleotide sequences into protein sequences was conducted using ORF Finder (http://www.ncbi.nlm.nih.gov/projects/gorf/). The resulting reading frames were translated into Fasta protein sequences and blasted in NCBI (blastp 2.2.27; Altschul et al., 1997, 2005) against non-redundant protein sequences (nr). Nucleotide and protein alignments were done with CLC sequence Viewer 6.7.

2.7.3 Western Blot

4000-10000 larvae (120 h old) were shock frozen in liquid nitrogen and stored at -80°C. To isolate the proteins the larvae were defrosted on ice, diluted in lysis buffer and homogenised using a Teflon-glass-homogeniser (B.Braun, Germany). After 20 min resting on ice, the homogenate was centrifuged at 4°C with 14000 rpm for 30 min (centrifuge 5417R, Eppendorf, Germany). Some of the supernatant was frozen at -20°C for a protein determination; the rest was diluted 5:1 with 5x Laemmli and denaturated at 56°C for 30 min. These samples were either stored at -20°C or used directly for a Western blot.

For Western blotting self-made gel (6-6.5% SDS-page and 4% stacking gel) and 4 µl of the marker (PageRuler Plus Prestained Protein Ladder #SM1811, Fermentas, Germany) were used. Colon tissue (origin: *Mus musculus*, protein amount: 5 µg μl^{-1}) served as a positive control (fixation and preparation as described for the larvae) and 0.18-0.8 µg μl^{-1} protein isolated from sea urchin tissue were applied to the gel.

The proteins were separated *via* electrophoresis using 100-120 V for 80 min. After this, the Western Blot-equipment was mounted (0.45 µm nitrocellulose membrane, Bio-Rad, Germany) and blotting was

achieved by 600 V for 75 min. After finishing this process, the membrane was washed with TBS-T, blocked with 5% skim milk powder for 60 min and the first antibody (either T4-supernatant, stored in glycerol (1:2) from DSHB,USA, dilution 1:50 or GTX107304 from GeneTex, USA, 1:1000; both in 5% BSA/TBS-T) was applied overnight at 4°C with slight shaking. The next day, the membrane was washed three times in TBS-T and the second antibody (donkey anti-rabbit, either Santa Cruz Biotechnology Inc, USA or Dianova, Germany, dilution 1:10,000 or 1:80000, respectively in 1% BSA/TBS-T or sheep-anti mouse, GE Healthcare, Germany, dilution 1:5000 in TBS-T) was applied for 60 min followed by washing (TBS-T, three times, each 10 min). Pictures were taken by an Image Reader (Fuji-Film Las-3000 mini, R&D Systems, USA) with ECL-advanced (Amersham Biosciences, ECL advanced Western Blotting Detection Kid). All recipes are given in chapter 2.9.3.

2.8 Histology

2.8.1 Paraffin

Aboral interambulacral pieces of normal grown adult urchins were fixed in 4% PFA (paraformaldehyde, obtained from Merck, Germany; solved in PBS, obtained from PAA Laboratories GmbH, Austria) before the skeleton was dissolved in EDTA (20%; obtained from Walter, Germany, solved in distilled water). The remaining epithelia were dehydrated in an ascending ethanol series (2x 50, 2x 70, 2x 80, 2x 90 and 2x 99%). After this, they were transferred to methylbenzoate and then to paraplast before pouring them into moulds. Cuts (5 µm slices) were generated using a microtom (Leica RM 2165, Germany), mounted on microscope slides and were standard stained with HE (Meyers Hämalaun, Eosin obtained from Merck, Germany). Pictures were taken with a CCD-camera (ProgRess®CF, Jenoptik, Germany) mounted to an Axiovert 200M (Zeiss, Germany) and peritoneal epithelium thickness was measured in ImageJ.

2.8.2 Immunohistochemistry

4000-10000 larvae (120 h old) were fixed in 4% PFA for 15 min and afterwards post-fixed in ice cold methanol at room temperature (1 min). They were washed three times in 70% Ethanol and stored in ethanol at -20°C until usage. Besides larvae cultivated in 2012 freshly fixed larvae from 2013 (cultivated in Sweden by Dr. Sam Dupont) were used for immunohistochemistry

After washing five times in 1x PBS (PAA Laboratories GmbH, Germany) the larvae were blocked in PBS-T-F (0.1% tween, 5% fetal bovine serum (FCS) in 1x PBS) for 2 h at room temperature. Two different first antibodies were used: either the polyclonal GTX107304 from GeneTex Inc., (USA), (dilution 1:100 in PBS-T-F) or the monoclonal T4 from DSHB (Iowa City, USA) (supernatant, stored in glycerol (1:2), dilution 1:2.5 in PBS-T-F). Larvae were incubated at 8°C overnight. After five washing steps (PBS-T-F), the second antibody (AlexaFluo 488, donkey anti-rabbit; AlexaFluo 633,

goat anti-rabbit or AlexaFluo 488, goat anti-mouse; Life Technologies GmbH, Germany) was applied for 1 h at room temperature. Larvae were washed again in PBS-T-F (3x) and 1x PBS (3x) and were either embedded in Moviol-Dabko or transferred to an imaging bath prior to imaging. Images were taken confocally using an LSM510 (Zeiss, Germany) at 488 nm and/ or 633 nm excitation (HFT 488/545/633, NFT 545, BP 505-530, LP 650 or HFT 488, LP 505) and stack sizes of 1-2 µm were conducted.

2.9 Experimental solutions and chemicals

2.9.1 Chemicals

All chemicals were of highest purified grade and purchased from Sigma, SERVA Electrophoresis and Merck (Germany) unless stated differently.

2.9.2 Artificial seawater

Artificial seawater solutions were prepared for the Ussing chamber experiments following Table 6. Further, the recipes for the bag fraction isolation protocol used in larval experiments are given in Table 7.

Table 6 Composition of different seawater solutions. The pH of the ASW used for the peritoneum studies was adjusted by additional HCl. The high HCO_3^- ASW solution was gased with 5% CO_2 prior to its usage.

	mM			
	ASW (peritoneum)	**ASW (intestine)**	**ASW (low NaCl)**	**ASW (high HCO_3^-)**
Na^+	504.4	448.8	188.8	424
K^+	9.9	9.9	9.9	9.9
Cl^-	545.1	527.0	267.0	449.9
SO_4^-	28.2	28.2	28.2	-
Mg^{2+}	53.3	53.3	53.3	-
Ca^{2+}	10.3	10.3	10.3	-
HCO_3^-	2.4	2.4	2.4	284
gluconate	37.6	-	-	-
sorbitol	-	-	966	-
NMDG	-	-	-	300
pH	7.2	8.2	8.2	8.3
mOsmol kg^{-1}	1031 ± 1.2	977.5 ± 3.0	983	1134

Table 7 Solutions for bag fraction isolation. Bag fraction isolation medium was produced as following: 200 ml of calcium-magnesium free seawater (CMFSW) was mixed with 200 ml 1M glucose and 40 ml deionised water. All recipes are according to Harkey and Whiteley (1980).

		mM	
	CMFSW	**dissociation medium**	**bag isolation medium**
Na^+	582.9	-	262.3
K^+	9.9	-	4.5
Cl^-	534.0	-	240.3
SO_4^-	28.2	-	12.7
Mg^{2+}	0	-	0.0
Ca^{2+}	0	-	0.0
HCO_3^-	2.4	-	1.1
glycin	-	1000	-
EDTA	-	0.1	-
TRIS	-	10.0	10.0
glucose	-	-	450
pH	8.0	8.0	8.0

2.9.3 Western Blot

The following recipes were used for the Western Blot analysis.

Table 8 Summary of Western Blot related recipes.

4x transfer buffer	
1.5 M	Tris/HCl
0.4%	SDS
in deionised water, pH 8.8	

4x stacking gel buffer	
0.5 M	Tris/HCl
0.4%	SDS
in deionised water, pH 6.8	

SDS-page, transfer gel (20 ml)		
6%	6.5%	
3 ml	3.25 ml	40% acrylamid
5 ml	5 ml	4x SDS-page buffer
12 ml	11.75 ml	deionised water
150 µl	150 µl	10% APS
60 µl	60 µl	TEMED

SDS-page, stacking gel (10 ml)		
4%	10%	
1 ml	2.5 ml	40% acrylamid
2.5 ml	2.5 ml	4x collection gel buffer
6.4 ml	5 ml	deionised water
75 µl	75 µl	10% APS
30 µl	30 µl	TEMED

5x Laemmli buffer	
1.25 mM	Tris
87%	glycerol
357 mM	SDS
519.5 mM	DTT
	bromphenol-blue
dissolved in deionised water	

TBS-T	
77.05 mM	Tris/HCl
300 mM	NaCl
0.05%	Tween
dissolved in deionised water; pH 7.6	

10x electrode buffer	
19.2 mM	glycin
250.3 mM	Tris
10%	SDS
dissolved in deionised water	

PonceauS	
1%	acetic acid
0.5%	ponceauS

Tank Blot buffer	
192 mM	glycin
20 mM	Tris
20%	Methanol
dissolved in deionised water	

Lysis buffer	
0.5%	TritonX100
1/10 ml	tablet "Roche complete protease inhibitor tablet"
dissolved in PBS	

2.10 Statistics

2.10.1.1 Larval results

Each fertilisation (one female, one male) was counted as one experiment and it was strived to use each male as rarely as possible to ensure a broad genetic variability. Within each experiment and the associated inhibitor concentrations, three to four larvae were analysed with respect to their development, primary body rod length, calcein incorporation and vesicle calcein fluorescence. These sub-replicates were averaged and their mean was treated as a true replicate. GaJ% data were arcsine transformed prior to statistical analysis.

Normality of distribution was tested using the Kolmogorov-Smirnov test. With a two-sample t-test (two groups) or a one-way ANOVA and an adjacent post-hoc Tukey test, differences between the inhibitor concentrations were tested (threshold for significance: $p < 0.05$) and the homogeneity of variances was tested with a Levene's test. Due to inhomogeneity of variances the Welch-test (2 groups) or a Kruskal-Wallis ANOVA was used. In case of the KANOVA the Mann-Whitney test was used instead of a post-hoc test because a non-parametric post-hoc test could not be performed with Origin 8G. To overcome the problem of multiple comparisons a Bonferroni correction was done at the 0.05 level (0.05/amount groups).

2.10.1.2 Adult results

For growth increment and breaking force measurements data from ossicles and spines of several sea urchins *per* tank were averaged and treated as a true replicate. In the case of breaking force measurements of spines, a maximum of three spines were measured *per* animal and averaged. Ossicles and spines of 6-12 animals *per* treatment were used for the SEM analysis. Percentage values of surface alterations in SEM pictures were arcsine transformed prior to statistical analysis.

Testing for normal distribution was done by using the Kolmogorov-Smirnov test and for homogeneity of variances using Levene's test. With a one-way ANOVA followed by a Tukey post-hoc test, differences between the CO_2 treatments were tested (threshold for significance: $p < 0.05$). Data for 4 and 500 kDa were reciprocally transformed. HCO_3^- diffusion and FITC-diffusion data were tested with the one-factorial repeated measures ANOVA, using the Greenhouse-Geisser correction. A subsequent post-hoc Tukey test was used. Differences in transepithelial potential were tested using a Students t-test.

All data are presented as mean values ± SEM. All statistical analyses were performed in OriginPro 8G SR4 (OriginLab Corporation, Northampton, USA).

3 Results

Most of the presented results will be part of one of the research articles or the review summarised in Table 9.

Table 9 List of submitted original research articles and articles in preparation as outreach of this thesis.

Title	comment
Maintenance of coelomic fluid pH in sea urchins exposed to elevated CO_2: the role of body cavity epithelia and stereom dissolution	original research article, accepted, journal: Marine Biology,
A sea urchin $Na^+K^+2Cl^-$ cotransporter is involved in the maintenance of the calcification-relevant cytoplasmic cords in sea urchin larvae	original research article, in preparation
Pharmacology and toxicology of sea urchin calcification	review article, in preparation

3.1 Inhibitory studies on larval calcification

In the following sub-chapters, I will present the results on the effects of several pharmacological channel and transporter inhibitors on sea urchin larvae. The main focus hereby lay on the ability of the compounds to inhibit calcification. This was analysed by measuring the length of the primary body rod. In addition, vitality and morphometric parameters were investigated to detect any toxic side effects on sea urchin larvae.

Mainly, the involvement of a sea urchin NKCC equivalent was tested by the application of three different loop diuretics (azosemide, bumetanide and furosemide) and, to understand more about the function of NKCC within calcification, the effect of 50 µM azosemide was studied in more detail for some of the presented parameters. Additionally used inhibitors were concanamycin A (target protein: V-ATPase), cyclopiazonic acid (target protein: Ca^{2+} ATPase), DIDS (target protein: SLC4 -family), omeprazole (target protein: H^+K^+ ATPase) and verapamil (target protein: L-type Ca^2 channels).

3.1.1 Effects of drug vehicle on measured parameters

The drugs were dissolved in DMSO which reached a maximal concentration of 0.1% in all treatments. To exclude any effects of DMSO on larval development or primary body rod calcification, a vehicle control (FSW+0.1% DMSO) was conducted. As shown in Figure 24, no differences between FSW- and FSW+0.1% DMSO incubation could be observed on larval development. Also no differences were

visible in primary body rod calcification (FSW: 166.2 ± 2.2 µm and FSW+0.1% DMSO: 166.9 ± 1.6 µm, *n* = 8-9, two sample t-test, t_{15} = -0.3, p = 0.8).

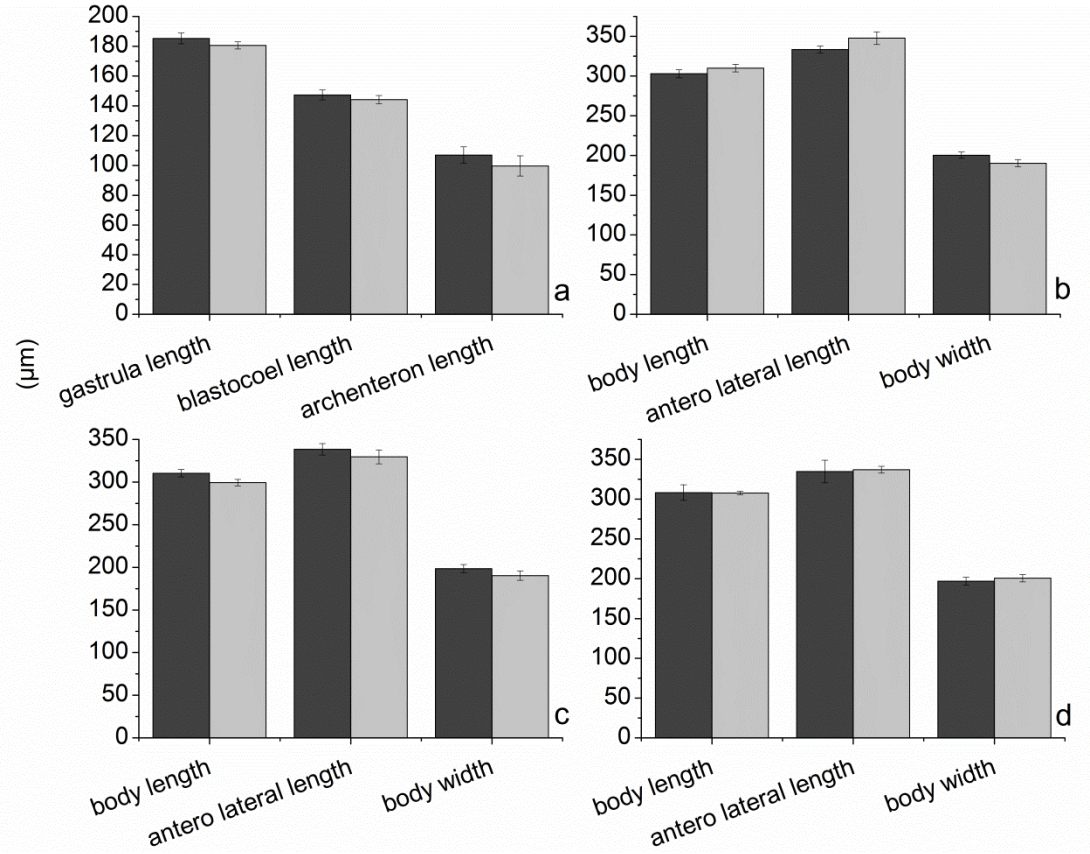

Figure 24 Effect of 0.1% DMSO on morphometrics of 48 and 120 h old larvae incubated for different time spans. Dark grey shows the respective length of larvae incubated in FSW, light grey shows the respective length of larvae incubated in FSW+0.1% DMSO; a) 24 h incubation of blastula stage, b) 92 h incubation of blastula stage, c) 72.5 h incubation of gastrula stage and d) 48 h incubation of prism stage. No significant difference were found (two sample t-test), mean values are given ± SEM (*n* = 5-9).

3.1.2 Effects of inhibitors on vitality

To estimate any toxic side effects of the used inhibitors, vitality of 120 h old pluteus stages was qualitatively determined by an estimate of their swimming behaviour *per* incubation well before they were fixed for later analysis (chapter 2.2.3). Larvae grown in FSW and FSW+0.1% DMSO were either actively swimming or at least mobile as were the larvae grown in loop diuretics (Table 10). In contrast to these groups, higher concentrations of cyclopiazonic acid (30 µM), DIDS (≥ 1 µM), omeprazole (200 µM) and verapamil (≥ 5 µM) resulted in larvae which were inactive (Table 10). Larval death was caused by ≥ 10 µM DIDS and ≥ 25 µM verapamil. The L-type Ca^{2+} channel inhibitor was most toxic for larvae as 50 µM caused larval death in 100% of the cases.

Table 10 Mobility of larvae after 48h incubation in the presence of the respective inhibitor, *per* well estimations were conducted for the total appearance of the larvae. The categories are the following: --: dead larvae, -: inactive, immobile, +: mobile and immobile, ++: actively swimming (*n = 5-23* incubation wells).

inhibitor	concentration (µM)	% --	% -	% +	% ++
FSW	-	0	0	18	82
DMSO (0.1%)	0.16	0	0	13	87
azosemide	1	0	0	44	56
	10	0	0	40	60
	20	0	0	20	80
	50	0	0	50	50
concanamycin A	0.005	0	0	0	100
	0.01	0	0	0	100
	0.05	0	0	10	90
	0.01	0	0	36	64
cyclopiazonic acid	1.5	0	0	0	100
	3	0	0	0	100
	15	0	0	9	91
	30	0	60	30	10
DIDS	0.5	0	0	10	90
	1	0	18	18	64
	5	0	56	22	22
	10	18	27	45	9
	20	17	67	17	0
omeprazole	2	0	0	0	100
	25	0	0	14	86
	50	0	0	0	100
	100	0	0	71	29
	200	0	86	14	0
verapamil	5	0	17	67	17
	10	0	57	43	0
	25	44	44	11	0
	50	100	0	0	0

Swimming behaviour of FSW + 0.1% DMSO and 50 µM azosemide-treated larvae was studied in addition. No differences in swimming behaviour (average swimming-length within 1 min of pluteus larvae, incubated at prism stage (arbitrary units): control = 614.2 ± 112.0 AU, 50 µM azosemide = 748.7 ± 156.7 AU, one-way ANOVA, $F_{(1,7)} = 0.44$, $p = 0.53$, $n = 4\text{-}5$) was found.

3.1.3 Effects of inhibitors on development and morphometrics

This analysis was used to detect any toxic side effects of the used inhibitors. The morphometrics of 120 h old pluteus larvae were analysed by determining their body length, antero-lateral length, the body width and by calculating the antero-lateral/body length ratio (chapter 2.2.3.2). Also, the early development in form of gastrulation was investigated.

3.1.3.1 24 h incubation of blastula stages to loop diuretics and further inhibitors

The GaJ%, which is the proportion of archenteron elongation into the blastocoel (Harkey and Whiteley, 1980), was measured after 24 h incubation in in azosemide and non-loop diuretics. Control values were 69 ± 4 (2011) and 75 ± 5 (2012) (n = 5-7) and loop diuretics slightly increased GaJ% after 24 h incubation (82 ± 4 at 50 µM azosemide, one-way ANOVA $F_{(4,21)} = 2.91$, $p = 0.05$, $n = 5$; Figure 25 and Figure 26). In contrast, the other inhibitors reduced GaJ% significantly (Figure 26). The gastrula length was only significantly reduced in the presence of 50 µM azosemide and 10 µM DIDS (Table 11).

3.1.3.2 92 h and 72.5 h incubation of blastula and gastrula stages to loop diuretics

Whether azosemide caused any disturbance on development, was also investigated in larvae which were incubated for 72.5 h and 92 h (starting stages: gastrula and blastula, respectively) until the pluteus stage. Development resulted in quasi normal pluteus with developed arms; however, all measured parameters were significantly shorter in the presence of ≥ 10 µM azosemide (Table 12) but the calculated ratio was > 1 in all cases indication the development of antero-lateral arms.

3.1.3.3 48 h incubation of prism stages to loop diuretics and further inhibitors

Larvae grown under loop diuretics developed into normally shaped pluteus larvae (Figure 28). However, their body length, total antero-lateral length and body width were significantly affected by higher concentrations of azosemide (Figure 27). In contrast to other inhibitor-experiments, the antero-lateral/body length ratio remained stable, indicating that arms were still being developed (Figure 28).

The non-loop diuretic inhibitors significantly affected morphometric parameters (Figure 27). Interestingly, the antero-lateral/body length ratio did not exceed 1 in higher concentrations of non-loop diuretics, indicating that the antero-lateral arms were not being developed and that the larval shape is rather spherical which is also shown in Figure 28. Moreover, the body and antero-lateral length and body width decreased to a value lower than the initial value in the presence of high concentrations of concanamycin A, cyclopiazonic acid, DIDS and verapamil (Figure 27).

3.1.3.4 Further development and settling (50 µM azosemide)

Some larvae were raised longer than 5 days and fed when *Rhodomonas* sp. was provided. In these larvae settlement and metamorphosis into juveniles was observed. The juveniles of three different fertilisations were raised from three different batches: control seawater conditions revealed normal developed juveniles; incubation in 50 µM azosemide for 72 h (incubated at an age of 72 h) again revealed normal development; however, incubation in 50 µM azosemide for 60 day revealed juveniles without spines (Figure 29).

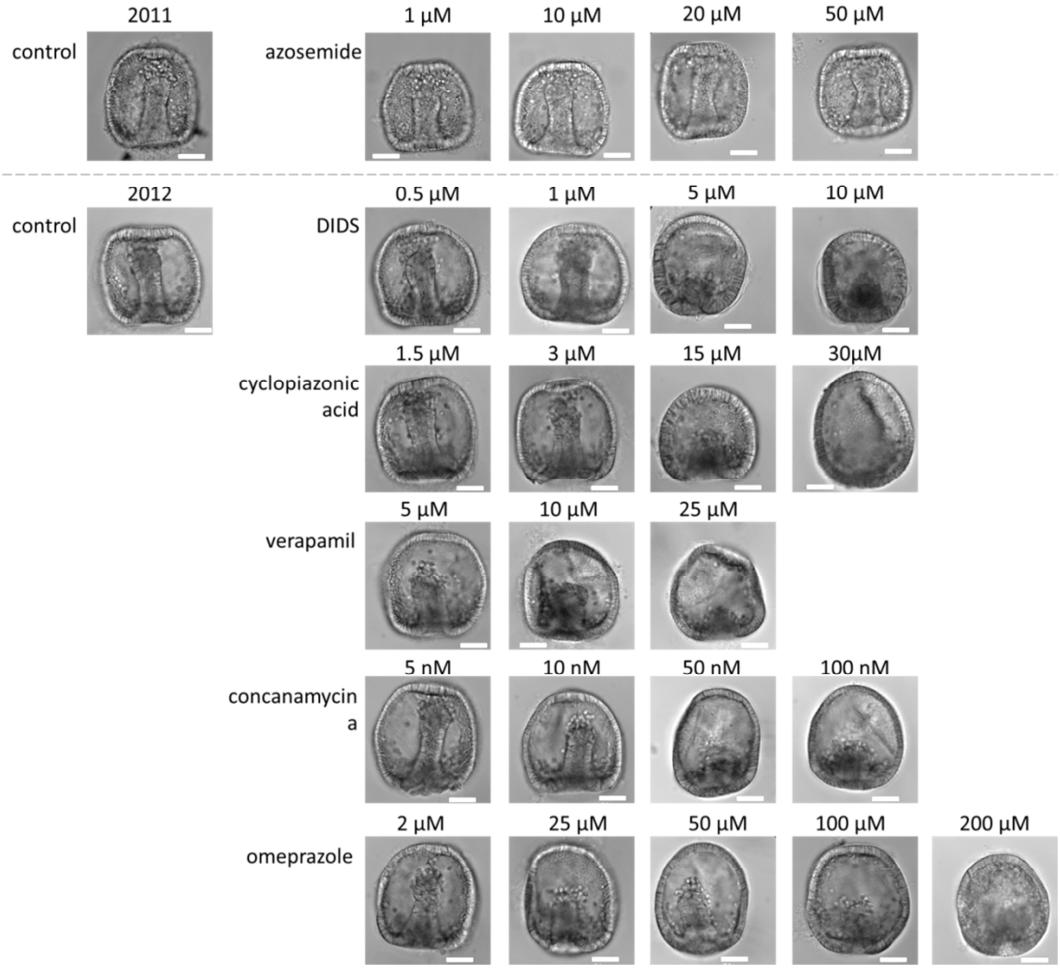

Figure 25 Effect of inhibitors on gastrulation. Azosemide-incubations were conducted 2011, the others 2012 as indicated. Normal gastrulation resulted in a GaJ% of 69-75 (Figure 26). Azosemide-treatment resulted in normal shaped gastrula stages; all other inhibitors show a concentration dependent loss in development. Scale bar = 50 µm.

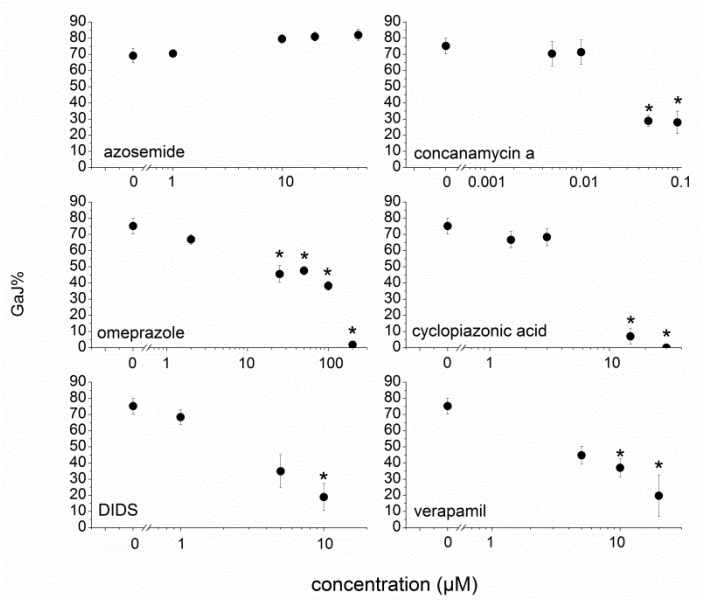

Figure 26 Effect of inhibitors on gastrulation. Azosemide did not change GaJ% but all non-loop diuretics caused a significant reduction of this parameter which are marked by an asterisk; mean values are given ± SEM (*n* = 5-8). One-way ANOVAs revealed the following F-, and p-values: azosemide $F_{(4,21)} = 2.91$, $p = 0.05$; DIDS $F_{(4,22)} = 9.81$, $p = 1.0 \times 10^{-4}$; concanamycin a $F_{(4,23)} = 9.73$, $p = 9.3 \times 10^{-5}$; verapamil $F_{(3,17)} = 11.76$, $p = 2.1 \times 10^{-4}$; Kruskal-Wallis ANOVA: omeprazole $H_{(5)} = 25.11$, $p = 1.3 \times 10^{-4}$; cyclopiazonic acid $H_{(4)} = 19.01$, $p = 7.81 \times 10^{-4}$

Table 11 Effect of different inhibitors on gastrula length after 24 h incubation. A one-way ANOVA was performed except of the DIDS-data, here a Kruskal-Wallis ANOVA and Mann-Whitney tests were performed. Significant differences ($p < 0.05$ and 0.01 in case of Mann-Whitney test) are indicated by different letters. Mean values are given ± SEM (n = 4-8).

				One Way ANOVA		Kruskal Wallis ANOVA	
inhibitor	µM	length gastrula (µm)		F	p	H	p
				$F_{(4,21)}$			
azosemide	0	180.5 ± 2.4	a	3.35	0.03		
	1	182.2 ± 3.9	a				
	10	177.8 ± 2.6	a				
	20	175.8 ± 1.2	a				
	50	169.7 ± 2.7	b				
				$F_{(4,23)}$			
concanamycin A	0	196.2 ± 3.5	a	1.27	0.31		
	0.005	194.4 ± 2.9	a				
	0.01	188.2 ± 5.4	a				
	0.05	182.0 ± 7.2	a				
	0.1	187 ± 7.2	a				
				$F_{(4,23)}$			
cyclopiazonic acid	0	196.2 ± 3.5	a	1.56	0.22		
	1.5	195.7 ± 3.7	a				
	3	193.5 ± 3.4	a				
	15	189.0 ± 3.6	a				
	30	180.3 ± 9.9	a				
						$H_{(4)}$	
DIDS	0	196.2 ± 3.5	a			8.96	0.06
	0.5	194.4 ± 1.4	a				
	1	188.5 ± 1.4	a				
	5	184.0 ± 7.4	a				
	10	177.8 ± 6.2	b				
omeprazole				$F_{(5,27)}$			
	0	196.2 ± 3.5	a	1.20	0.33		
	2	200.4 ± 4.0	a				
	25	207.7 ± 6.7	a				
	50	207.1 ± 6.5	a				
	100	197.8 ± 3.8	a				
	200	196.7 ± 3.6	a				
verapamil				$F_{(3,18)}$			
	0	196.2 ± 3.5	a	1.39	0.28		
	5	192.0 ± 4.8	a				
	10	183.8 ± 3.1	a				
	25	200.4 ± 8.2	a				

A) body width

B) body length

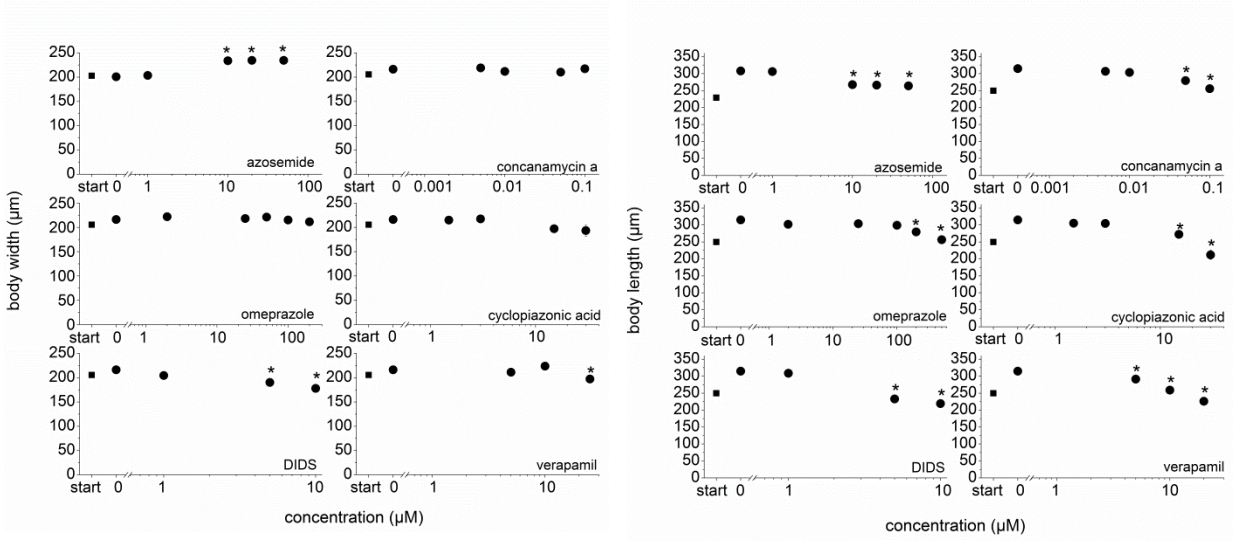

C) antero-lateral length

D) ratio antero-lateral/body length

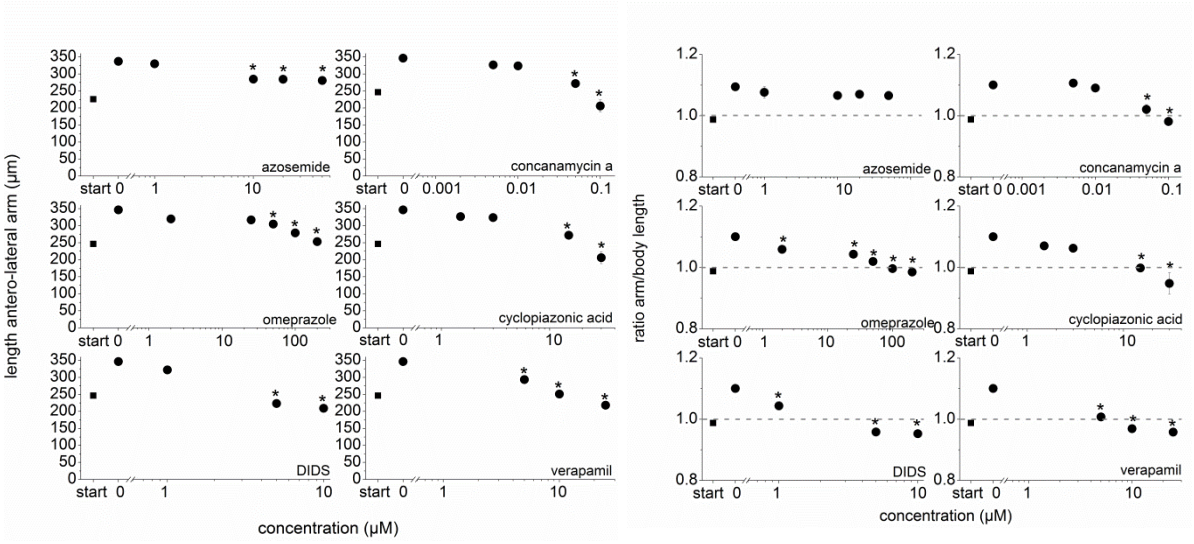

Figure 27 Summary of inhibitor effects on larval morphometrics. A shows the change in body width, B the effect on body length, C the total antero-lateral arm length and D the effects on the arm/body length ratio where 1 is marked by a dotted line. In all graphs the start values (72 h old prism stages) are shown as a filled square, the values of 120 h pluteus larvae are shown as filled dots. All mean values are given ± SEM (n = 4-10). In most cases the SEM is not visible due to the size of the symbols. Significant differences between 0 µM and any inhibitor concentration are indicated by an asterisk; F- and p-values are given in Table 13.

Table 12 Morphometrics of 120 h pluteus larvae incubated for 92 and 72.5 h to different azosemide concentrations. 92 h incubated larvae were incubated as blastula stages (28 h old), 72.5 h incubation started at gastrula stage (47.5 h old). Bl = body length, al = antero-lateral length, r = ratio antero-lateral/body, w = width. One-way ANOVA was done and significant differences are indicated by different letters; in case of inhomogeneous variances a Kruskal-Wallis ANOVA was conducted. Significant differences ($p < 0.05$ and 0.01 in case of Mann-Whitney test) are indicated by different letters. Mean values are given ± SEM (n = 5-7).

	azosemide (µM)										One Way ANOVA		Kruskal Wallis ANOVA	
	0		1		10		20		50		F	p	H	p
92 h incubation of blastula stage														
											$F_{(4,21)}$		$H_{(4)}$	
bl	309.9 ± 4.7	a	308.7 ± 6.8	a	275.7 ± 7.8	b	262.4 ± 3.0	b	255.7 ± 3.8	b	26.3	6.6×10^{-8}		
al	347.7 ± 4.6	a	344.5 ± 7.8	a	304.1 ± 11.6	b	279.1 ± 2.9	b	264.4 ± 4.8	b	34.5	5.9×10^{-9}		
r	1.1 ± 0.02	a	1.1 ± 0.01	a	1.1 ± 0.01	a	1.06 ± 0.01	a	1.04 ± 0.01	b			15.2	0.004
w	190.2 ± 4.6	a	194.8 ± 6.4	a	205.9 ± 7.9	b	225.6 ± 1.5	b	215.0 ± 2.0	b	11.5	4.2×10^{-5}		
72.5 h incubation of gastrula stage														
											$F_{(4,22)}$		$H_{(4)}$	
bl	299.4 ± 3.7	a	313.7 ±2.6	b	266.4 ± 8.4	b	254.5 ± 2.3	b	260.6 ± 3.5	b			20.4	4.3×10^{-4}
al	329.5 ± 8.0	a	343.9 ± 5.3	b	281.1 ± 8.2	b	274.1 ± 2.7	b	273.2 ± 3.8	b			19.6	5.9×10^{-4}
r	1.1 ± 0.02	a	1.1 ± 0.01	a	1.06 ± 0.01	a	1.08 ± 0.01	a	1.05 ± 0.01	a	3.2	0.03		
w	190.3 ± 5.5	a	198.1 ± 5.3	a	218.3 ± 4.9	b	229.7 ± 4.6	b	227.4 ± 1.1	b	14.6	5.9×10^{-6}		

Table 13 Summary of one-way ANOVA F- and p-values for morphometric data given in Figure 27. For the antero-lateral length of azosemide treated larvae no values are given as the variances of these data were not homogenous. Alternatively, a Kruskal-Wallis ANOVA was done and resulted in a $H_{(4)}$ of 21.2 and a p = 0.0003. (n = 4-10)

	body width		body length		antero-lateral length		ratio	
	F	p	F	p	F	p	F	p
	$F_{(4,24)}$		$F_{(4,24)}$				$F_{(4,24)}$	
azosemide	13.78	5.7×10^{-6}	47.91	4.2×10^{-11}	-	-	0.99	0.43
	$F_{(5,39)}$		$F_{(5,39}$		$F_{(5,39)}$		$F_{(5,39)}$	
omeprazole	0.63	0.68	12.25	3.6×10^{-7}	17.30	5.3×10^{-9}	27.9	6.7×10^{-12}
	$F_{(4,29)}$		$F_{(4,29)}$		$F_{(4,29)}$		$F_{(4,29)}$	
DIDS	6.59	6.7×10^{-4}	62.28	8.1×10^{-14}	78.88	3.7×10^{-15}	51.26	9.7×10^{-13}
	$F_{(4,33)}$		$F_{(4,33)}$		$F_{(4,33)}$		$F_{(4,33)}$	
concanamycin A	0.49	0.75	18.74	4.0×10^{-8}	29.91	1.5×10^{-10}	23.4	3.1×10^{-9}
	$F_{(4,26)}$		$F_{(4,27)}$		$F_{(4,26)}$		$F_{(4,26)}$	
cyclopiazonic acid	3.33	0.02	30.07	1.4×10^{-9}	27.34	5.6×10^{-9}	21.41	6.5×10^{-8}
	$F_{(3,23)}$		$F_{(3,23)}$		$F_{(3,23)}$		$F_{(3,23)}$	
verapamil	4.54	0.01	41.44	1.9×10^{-9}	58.46	6.5×10^{-11}	98.04	3.0×10^{-13}

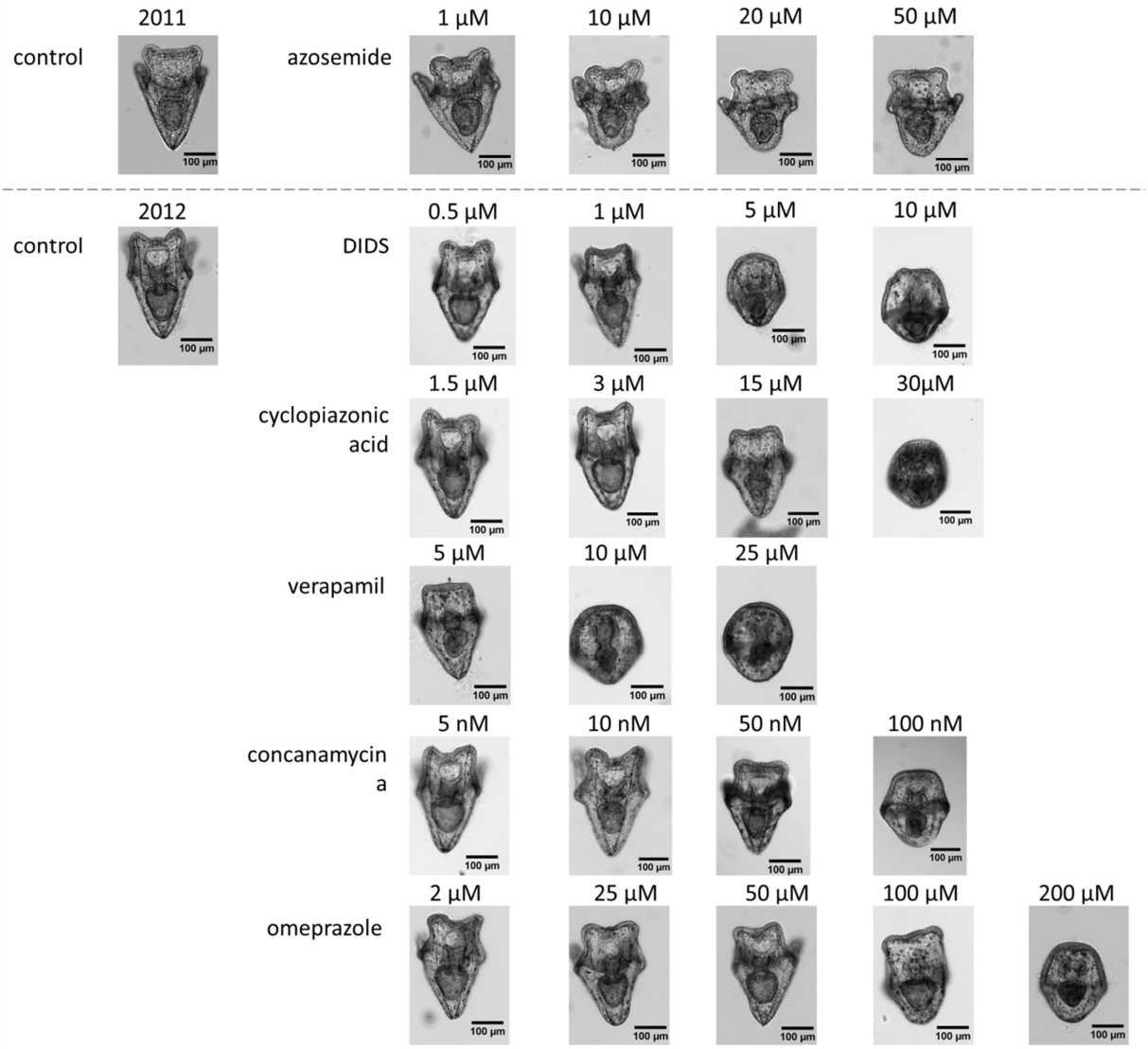

Figure 28 Effect of inhibitors on pluteus development. Larvae were incubated for 48 h to the respective conditions and were fixed at the age of 120 h. Normal development resulted in four distinguishable arms and a digestive system. Azosemide-treatment resulted in normal shaped larvae; all other inhibitors showed a concentration dependent loss in development.

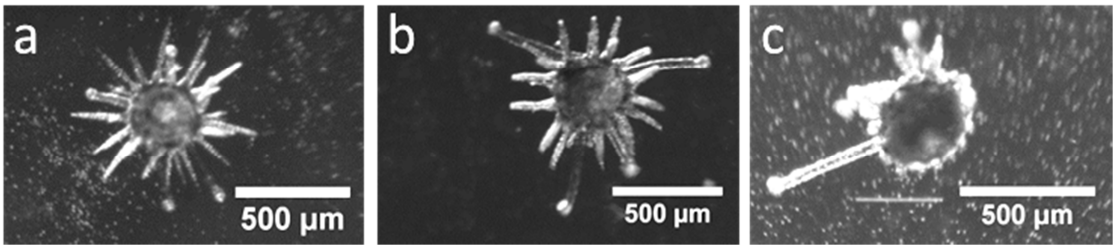

Figure 29 Juveniles fertilised 60 days prior to the photographs. Under control conditions (a) they developed spines, when pluteii (6 days old) were incubated into FSW after 72 h incubation in 50 µM azosemide, they developed spines, too (b). Pluteii grown under 50 µM azosemide while the prism stage developed into juveniles without spines (c). In all pictures, one can see tube feet of the juveniles (for example in (c) on the left part of the juvenile).

3.1.4 Effects of inhibitors on calcification

The main focus of the inhibitory studies was to investigate and confirm ion transporters and channels which are involved in larval calcification. Larvae were incubated for different time spans (Table 3) and the primary body rod was measured (chapter 2.2.4.1).

3.1.4.1 92 h and 72.5 h incubation of blastula and gastrula stages to loop diuretics

Calcification was severely disturbed in a concentration dependent matter when sea urchin larvae were incubated early in development. Based on the abnormal growth of the skeleton body rod, length was not measurable and categories for calcification judgement were introduced: (1) normal growth, (2) abnormal growth (3) no rods, (4) no skeletal structures (chapter 2.2.4.1, Figure 16).

The analysis revealed that 65% of the 50 µM azosemide incubations, started at the blastula stage, were characterised by completely undeveloped skeletons, whereas at the same treatment of the gastrula stage, visible skeleton parts were developed (Figure 30).

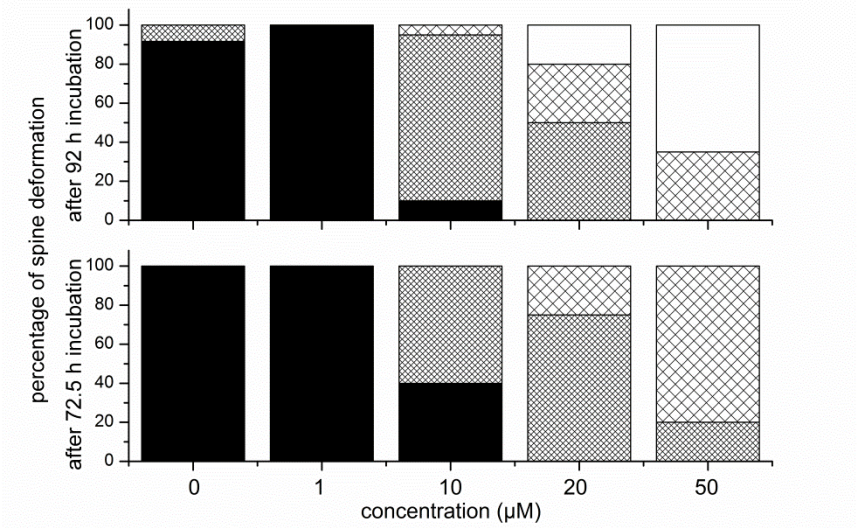

Figure 30 92 h (upper diagram) and 72.5 h (lower diagram) incubation of blastula and gastrula stages to azosemide. The deformations are shown in percentages (normal growth = black, abnormal growth = dense grid, no rods = light grid, no skeletal structures = white), (*n* = 20-28).

3.1.4.2 Growth of the primary body rod in 48 h incubations

When larvae were incubated at prism stage for 48 h, the skeletons did not show any abnormalities and thus, growth of the primary body rod was measured in all inhibitor treatments.

The initial body rod length of inhibitory studies was 44.3 ± 4.6 µm (*n* = 9) in 2011 and 65.8 ± 4.7 µm (*n* = 10) in 2012. In all loop diuretic treatments, the primary body rod length decreased in a concentration dependent manner and IC_{50} values were estimated. They were calculated to be 6.4 µM for azosemide, 26.5 µM for bumetanide and 315.3 µM for furosemide (Figure 31). Also, the non-loop diuretic inhibitors caused a decrease in primary body rod calcification, dependent on the used

concentration (Figure 32). Significant reductions were again caused by higher concentrations but even under highest concentrations, calcification was not as reduced as it was in the presence of azosemide. Based on the impact of non-loop diuretics on development and morphometrics (chapter 3.1.1 and 3.1.3) no IC_{50} values for the decrease of primary body rod length were calculated.

The growth in primary body rod thickness was studied for 50 µM azosemide. As shown in Table 14, the thickness increased significantly under control conditions from 1.3 ± 0.05 µm to 8.4 ± 0.3 µm (Welch test, $t_{6.2}$ = -21.2, p = 4.65 x10^{-7}, *n* = 6-7). In the presence of 50 µM azosemide the thickness was 2.2 ± 0.1 µm after 48 h incubation and thus significantly lower compared to the control thickness (Welch test, $t_{7.12}$ = 17.9, p = 3.54 x10^{-7}, *n* = 7).

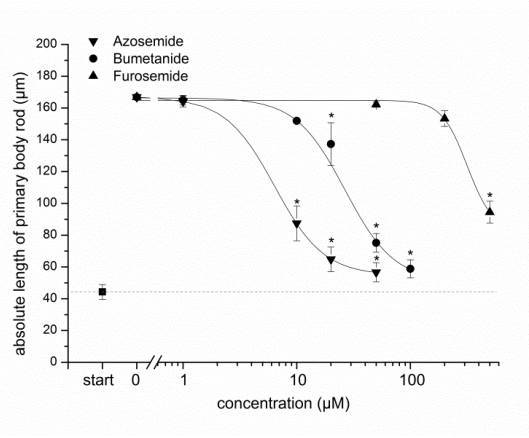

Figure 31 Concentration dependent inhibition of primary body rod length caused by a 48 h incubation of prism stage to loop diuretics. Mean values are given ± SEM (*n* = 5-9). One-way ANOVA: azosemide $F_{(4,21)}$ = 67.6, p = 1.1 x10^{-11}; Kruskal Wallis ANOVA bumetanide $H_{(5)}$ = 27.7, p = 4.1 x10^{-5}; furosemide $H_{(3)}$ = 15.2, p = 0.002.

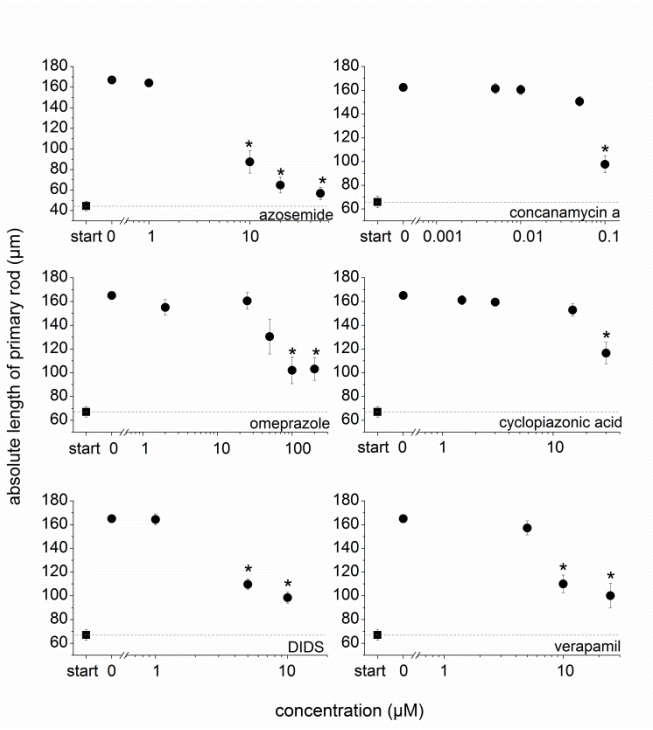

Figure 32 Effect of non-loop diuretics on primary body rod calcification. The effect of azosemide is again shown in this figure for comparison. Mean values are given ± SEM (*n* = 5-10). One-way ANOVAs revealed the following F-, and p-values: azosemide $F_{(4,21)}$ = 67.6, p = 1.1 x10^{-11}; omeprazole $F_{(5,36)}$ = 9.38, p = 8.6 x10^{-6}; DIDS $F_{(4,28)}$ = 62.2, p = 1.6 x10^{-13}; concanamycin A $F_{(4,32)}$ = 49.58, p = 2.9 x10^{-13}; cyclopiazonic acid $F_{(4,28)}$ = 15.2, p = 1.0 x10^{-6}; verapamil $F_{(3,23)}$ = 33.4, p = 1.5 x10^{-8}.

3.1.4.3 Azosemide-inhibition of calcein incorporation into the primary body rod

Analysing the calcein incorporation into the primary body rod in the presence of 50 µM azosemide, revealed that less calcein was incorporated during the incubation compared to the control treatment (Table 14). The length of the primary body rod was 90.5 µm in azosemide treated larvae and along 66 % of this length calcein was detectable. However, the intensity of this calcein was rather low as shown by the area-normalisation (100 µm^2) (Table 14) and by comparing two pictures taken with the same settings (Figure 33).

Table 14 Effect of azosemide incubation on calcein incorporation and primary body rod thickness. The length and thickness of the primary body rod, the length of calcein incorporation and the area-normalised fluorescence decreased significantly in the presence of 50 µM azosemide. Data were obtained in 2012 which explains the differences in the starting primary body rod compared to other azosemide data. Significant differences ($p < 0.05$) are indicated by different letters (One-way ANOVA and Welch-test); mean values are given ± SEM (n = 6-7).

	start (72h old)		0 µM azosemide (120h old)		50 µM azosemide (120h old)		Welch-test	One-way ANOVA	
							p	F	p
primary body rod								$F_{(1,12)}$	
length body rod	84.4 ± 3.4		167.8 ± 1.9	a	90.5 ± 5.6	b	2.3×10^{-6}		
length calcein incorporation			166.1 ± 2.3	a	60.0 ± 8.6	b		143.18	5.0×10^{-8}
fluorescence *per* 100 µm² (RFU)			12.5 ± 1.0	a	3.1 ± 1.5	b		25.93	2.7×10^{-4}
thickness body rod (20 µm from tip)			8.4 ± 0.3	a	2.2 ± 0.1	b	3.5×10^{-7}		
	1.3 ± 0.05	a	8.4 ± 0.3	b			4.7×10^{-7}		
	1.3 ± 0.05	a			2.2 ± 0.1	b	3.0×10^{-5}		

3.1.5 Investigations of functional involvement of NKCC

The functional understanding of NKCC in calcification was addressed by two investigations: on the one hand the occurrence of calcein stainable calcification vesicles in the presence of 50 µM azosemide was tested and on the other hand the effects of 50 µM azosemide on the PMC-filopodia were investigated (chapter 1.4.1).

3.1.5.1 Effect of azosemide on calcification vesicle size and calcein-intensity

In both treatments, control and 50 µM azosemide, calcein stained vesicles were visible (Figure 34). These vesicles did not change in terms of size (0.8 ± 0.1 µm and 0.9 ± 0.0 µm; two sample t-test $t_{(16)} = -0.78$, $p = 0.4$, $n = 9$) but in calcein intensities (Table 15). Interestingly, vesicles of azosemide-treated larvae showed a significantly higher calcein intensity (43 ± 6 RFU) compared to vesicles of control-treated larvae (25 ± 2 RFU) (Welch test, $t_{(9.6)} = -2.6$, $p = 0.02$, $n = 9$).

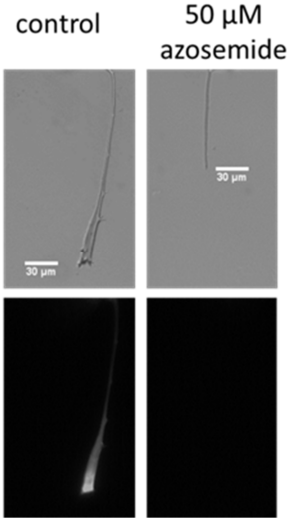

Figure 33 Comparison of calcein incorporation within the primary body rod under control conditions and in the presence of 50 µM azosemide. Both fluorescence pictures are taken with the same settings.

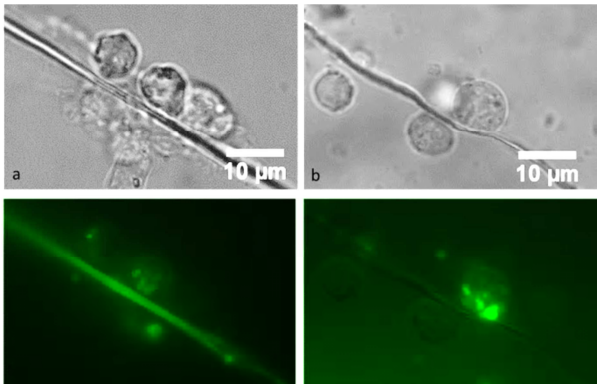

Figure 34 Calcein incorporation within calcification vesicles. (a) shows vesicles of control-treated larvae where also calcein incorporation within the spicule is visible. In contrast, azosemide-treated larvae (b) did not show calcein corporation within the spicule but calcein stained vesicles were also observed.

Table 15 Calcein staining of calcification vesicles of 48 h incubated larvae. The size of PMCs and vesicles did not change in the presence of azosemide but the intensities of calcein stained vesicles did. Significant differences ($p < 0.05$) are indicated by different letters (two sample t-test and Welch-test). Mean values are given ± SEM ($n = 9$).

	0 µM azosemide (120h old)		50 µM azosemide (120h old)		Welch-test	t-test
					p	p
calcification vesicles						
size PMCs (µm)	7.8 ± 0.2	a	7.8 ± 0.3	a		0.92
size vesicles (µm)	0.8 ± 0.1	a	0.9 ±0.0	a		0.44
vesicle-intensities (RFU)	25.4 ± 2.0	a	42.9 ± 6.4	b	0.03	
n experiments	9		9			
n larvae	22		22			
n PMCs	57		42			
n vesicles	151		98			

3.1.5.2 Effect of azosemide on PMC-filopodia

Under control conditions, the filopodial network of PMCs was visible and the cytoplasmic cord around the spicules was stained (Figure 35c). In azosemide treated larvae, thin filopodia were still visible (Figure 35e); however, the cytoplasmic cord was absent in the investigated larvae (Figure 35d).

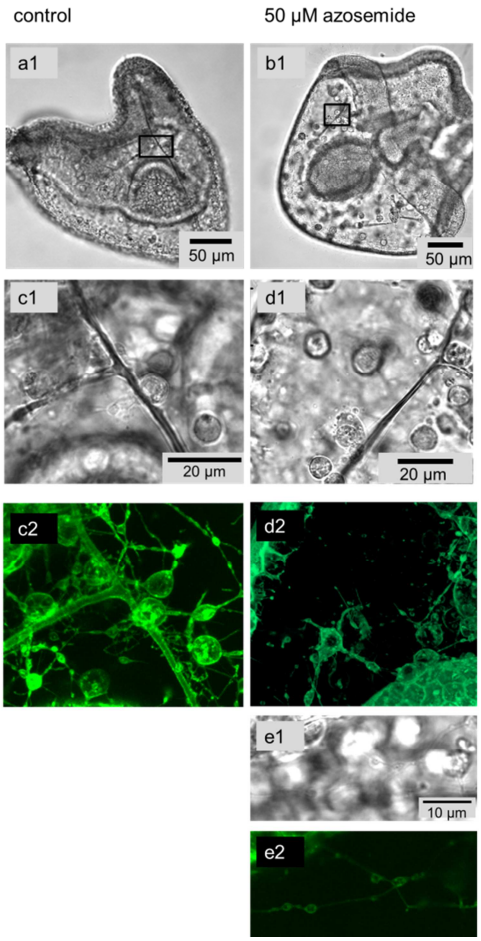

Figure 35 FM 1-43 staining of the filopodial network and cytoplasmic cord. In control treated larvae (a,c) both parts are visible whereas in 50 µM azosemide treated larvae (b,d,e) only the filopodial network is visible.

3.1.6 Molecular proof of NKCC within sea urchin larvae

Besides the pharmacological proof of NKCC within *S. droebachiensis* larvae, its expression and localisation within larvae was also addressed with molecular biology methods. The abbreviations *sd*- (*S. droebachiensis*) and *sp*- (*S. purpuratus*) are used.

3.1.6.1 RT-PCR

In the *sd*-larval transcriptome three NKCC-associated reads were located and were used to generate primer pairs. Additionally, primer pairs were generated by using the known *sp*-NKCC sequence (Table 5).

The primer pairs no. 1, 3, 4, 5, 6, and 7 were successful in creating a product although the product length of no. 1 did not match the expected product length of 824 bp. The primer pairs 2, 9, and 10 failed in producing any PCR-product. The non-NKCC related primer pair nad5 produced an expected product length.

Furthermore, forward and reverse primers were combined to produce products beyond the known transcriptome reads but failed to produce any product except for the combination of no. 3 (rev) and no. 7 (fwd). However, the ~650 bp long product was shorter than the calculated product of 1591 bp (calculated on the base of the *sp*- NKCC sequence).

All sequenced products (primer pairs no. 3, 4, 5, 6, and 7) resulted in sequences identical to *sp*-NKCC (e-value of 0.0-4 $x10^{-73}$). The sequences are summarised in the appendix and their location along *sp*-NKCC is shown in Figure 36.

The sequence product of primer pair 8 did not result in any NKCC-related homology but revealed identities with uncharacterised mRNA of sea urchin sperm (XM_778283.3, XM_001186058.2).

Figure 36 Localisation the sequenced areas (blue) along the *S. purpuratus* nucleotide sequence (grey). The product number is in alignment with the primer pair numbers.

3.1.6.2 Western Blot

In all of these attempts (either with the monoclonal or polyclonal antibody), no protein band was found of the predicted size (119 kDa for *sp*-NKCC); only faint bands of approximately 70 kDa were detected (Figure 37). In contrast to this, the positive control (colon tissue, *Mus musculus*) showed several strong bands. Nearest to the expected size of mouse NKCC1 (130 kDa) are the strong bands at > 130 kDa (polyclonal) and 190 kDa (monoclonal antibody).

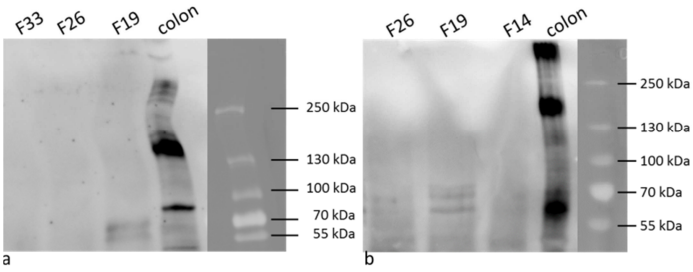

Figure 37 Exemplary Western Blot for the polyclonal (a) and monoclonal (b) antibody of mouse colon and larval tissue (numbers indicate different samples). The expected size of NKCC1 is 130.67 kDa for *Mus musculus* and 119.27 kDa for *S. purpuratus* (http://www.encorbio.com/protocols/Prot-MW.htm).

3.1.6.3 Immunohistochemistry

Antibody specificity

Two different antibodies were used; the monoclonal antibody revealed a specific and clear staining in contrast to the polyclonal antibody (Figure 38). However, the recombinant protein fragments of both antibodies were identical to the same protein fragment in three different organisms (*Homo sapiens*, *Danio rerio* and *S. purpuratus*) (Figure 39).

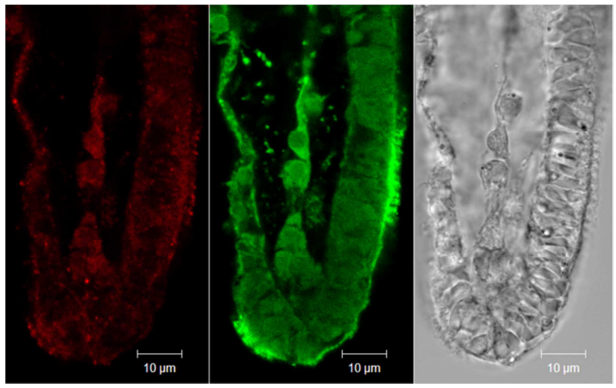

Figure 38 Comparison of the polyclonal (633, red) and the monoclonal (488, green) antibody; embedded larvae.

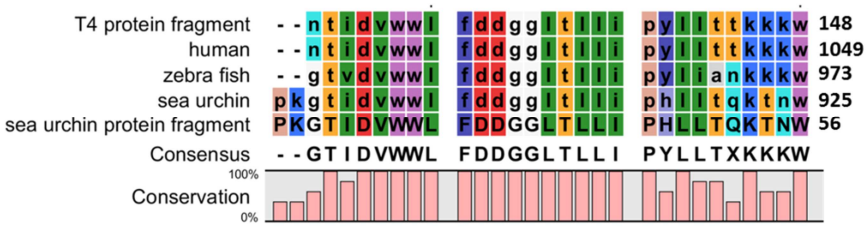

Figure 39 Alignment of the recombinant protein fragment of the monoclonal antibody (T4) with protein sequences of *Homo sapiens* (P55011.1), *Danio rerio* (NP_001002080) and *S. purpuratus* (NP_001106707). The T4 fragment is known to be located at AS 902-1212 on the human protein sequence (P55011.1). The sea urchin protein fragment originates from *S. droebachiensis* after translating the transcriptomal read no 2 and 3. The same result is gained when the recombinant protein fragment of the polyclonal protein fragment (AS 897-1174) is aligned to the sequences.

Monoclonal antibody

Successful staining was detected in embedded and free floating larvae fixed in 2012 and freshly fixed larvae from 2013 (Figure 38; Figure 41). In both stainings, the ectoderm, digestive system and PMCs were stained (Figure 40; Figure 41). Detailed pictures of the PMCs show a staining within PMC cytoplasm and a dominant staining of the associated cytoplasmic cords (Figure 41).

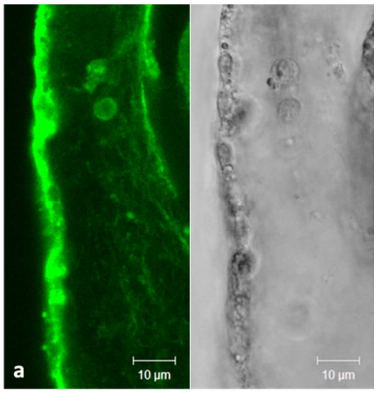

Figure 40 Staining of the ectoderm and the thin filopodial network within the larvae body cavity; free floating larvae.

In addition to the cytoplasmic cord, thin filopodia or parts of the body cavity-extracellular matrix were also stained (Figure 40). However, this staining was rather weak and only visible occasionally.

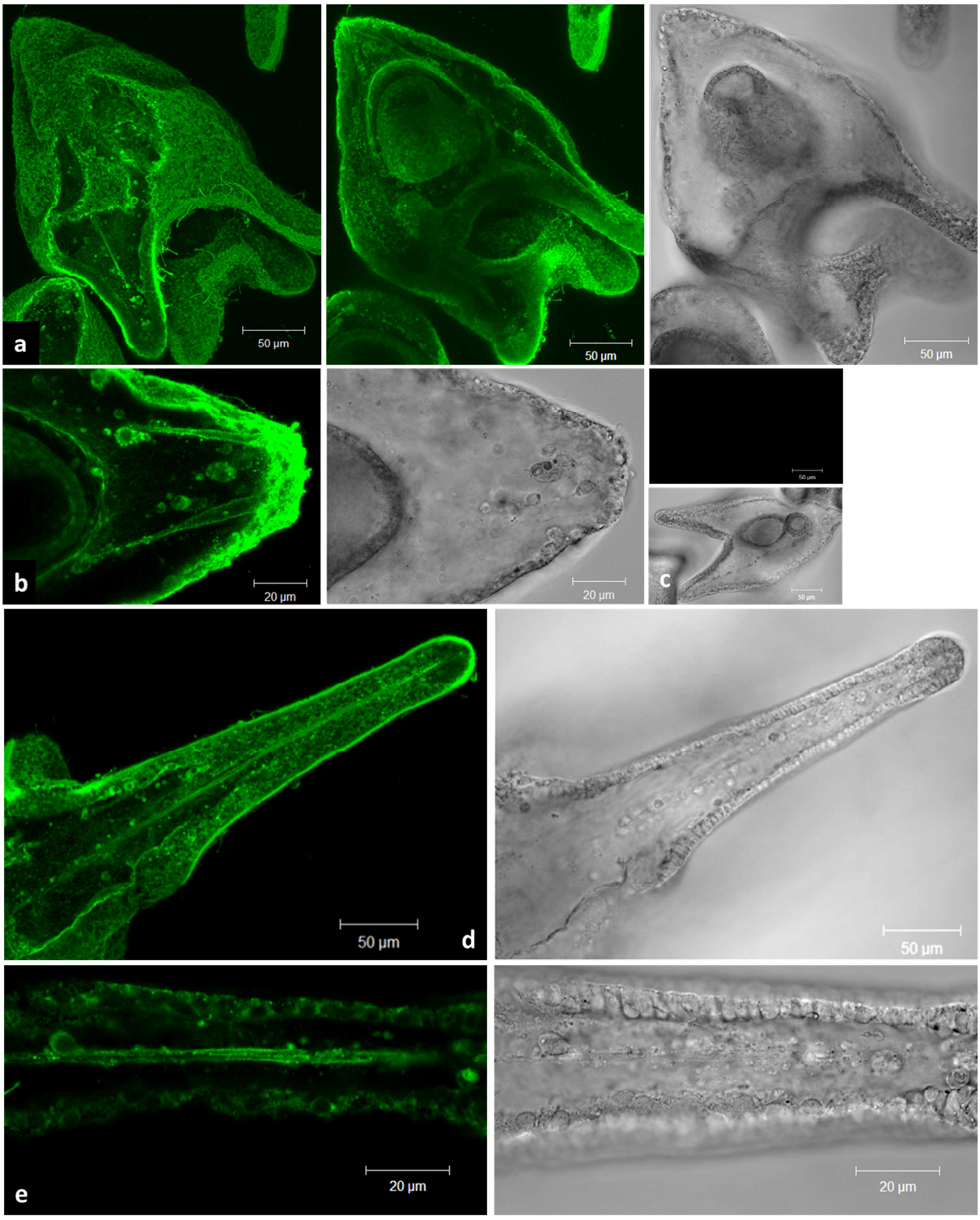

Figure 41 Immunohistochemistry of *S. droebachiensis* using T4 antibody against NKCC. In (a) two projections, generated from 1 µm stacks are given. Both projections show cytoplasmic cord staining's of the antero-lateral arm rods. In (b) the cytoplasmic cord of the primary body rod is visible. Detailed view of one arm of fed larvae (8 days old, already fed). (d) Projections of the arm generated from 1 µm stacks; in (e) the structure of the cytoplasmic cord is visible. Autofluoresence and unspecific stainings with the second antibody (goat anti-mouse) are negligible (c); free floating larvae.

3.1.6.4 Homologies of sea urchin NKCC to other NKCC isoforms of other species

The phylogenetic tree, calculated for the protein, revealed that *sp*-NKCC is not related to NKCC1 or NKCC2 as it is separated early in evolution before the separation into NKCC1 and NKCC2 (Figure 42).

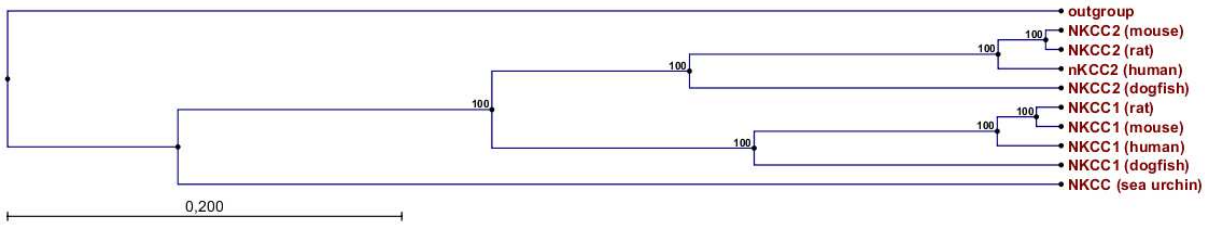

Figure 42 SLC12-family phylogenetic tree, protein level, calculated with UPGMA algorithm. The NKCC sequence of the tobacco hornworm (AAA75600) were used as outgroup, the other used NKCC isoforms derived from rat (NKCC1: NP_113986; NKCC2: NP_062007), human (NKCC1: NP_001037; NKCC2: NP_00032), spiny dogfish (NKCC1: AAB60617; NKCC2: AAM74966), mouse (NKCC1: NP_033220; NKCC2: NP_899197.2) and sea urchin (NP_001106707). Numbers at the nodes show the bootstrap analysis result (100 bootstrap replicates), the scale shows the fraction of amino acid substitution.

Using *sp*-NKCC nucleotide sequence to search within the EST library of *S. purpuratus* resulted in the best fit for a cDNA clone which originated from whole 2-3 week old *S. purpuratus* larvae (gb|CD306566.1|) (Poustka et al., 2003) having a maximal identity of 91% and an e-value of 2 $x10^{-64}$ (blastn and tblastn). Within the cDNA library from primary cultured PMCs (Zhu et al., 2001) no homology was found for *sp*-NKCC. Also the *sd*-sequence products 4 and 6 did not reveal any *S. purpuratus* related hits, only an mRNA sequence of *Paracentrotus lividus* (AM204441) was found with product 4.

3.2 Epithelial properties of adult tissue

The following sub-chapters present the transcellular and paracellular properties of two adult tissues, the intestine and the peritoneal epithelium. I investigated both tissues on the background of their involvement in acid-base homeostasis in adult sea urchins. For this, I examined their electrical properties using the Ussing chamber technique and their diffusional properties in terms of either HCO_3^- (intestine) or molecular sizes (peritoneal epithelium).

3.2.1 Properties of the intestine

3.2.1.1 Electrical properties

The initial electrical properties of the intestine revealed a resistance (R_{te}) of 6.2 ± 1.3 Ωcm^2, a lumen negative potential (V_{te}) of -0.9 ± 0.2 mV and a respective short circuit current (I'_{sc}) of -181 ± 26 µA cm^{-2}. These values changed so that after 10 min an average R_{te} of 14.2 ± 1.4 Ωcm^2, a lumen negative

V_{te} of -0.3 ±0.1 mV and a respective I'_{sc} of -20 ± 4 µAcm^{-2} (*n* = 11) was determined (Figure 43). The luminal applications of either 0.1% DMSO (vehicle control) or 50 µM DIDS led to a significant decrease in V_{te} and were not different from each other. Basolateral application of these substances did not change the electrical properties (Figure 43).

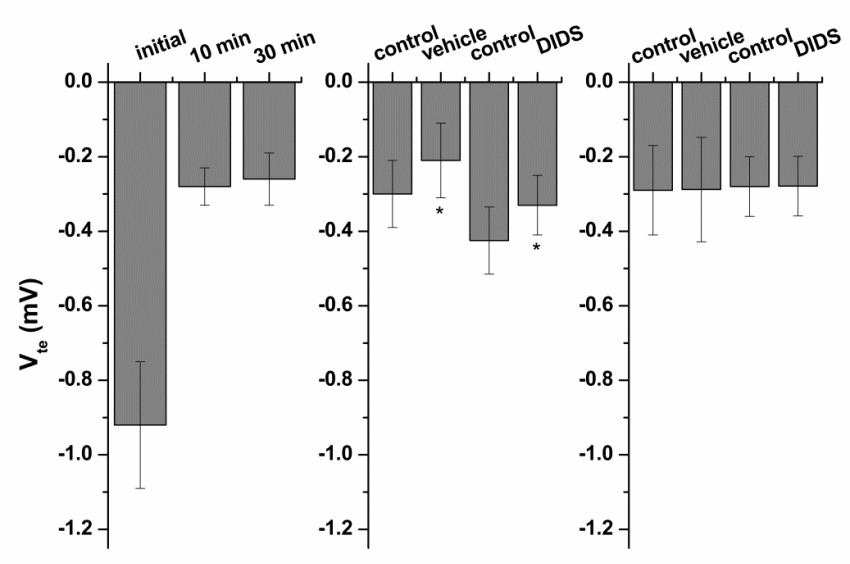

Figure 43 Electrical properties, depicted as V_{te}, of the intestine under control conditions at three time points. The initial lumen-negative potential decreased rapidly and remained stable for at least 30 min. In paired experiments the effects of vehicle (0.1% DMSO) and DIDS (50 µM in 0.1% DMSO) application from either the luminal or basolateral side are shown and resulted in significant differences when substances were applied luminally. Significant differences between control and vehicle/drug are marked with an asterisk (mean values are given ± SEM; *n* = 4-7, paired t-test, $p < 0.05$).

3.2.1.2 HCO_3^- diffusion

The measurements of HCO_3^- tightness of the intestine showed that within the first 30 min the intestine was virtually tight for HCO_3^- with a calculated permeability coefficient P_{HCO3} in this period of 1.0 ± 2.0 x10^{-5} cm s^{-1}, (*n* = 6). Within the last 60 min the HCO_3^- concentration increased significantly (repeated measurement ANOVA, $F_{(8,23)} = 11$, $p = 0.02$, Greenhouse Geisser corrected) (Figure 44) and the permeability coefficient P_{HCO3} increased to 3.1 ± 0.6 x10^{-5} cm s^{-1} (*n* = 2).

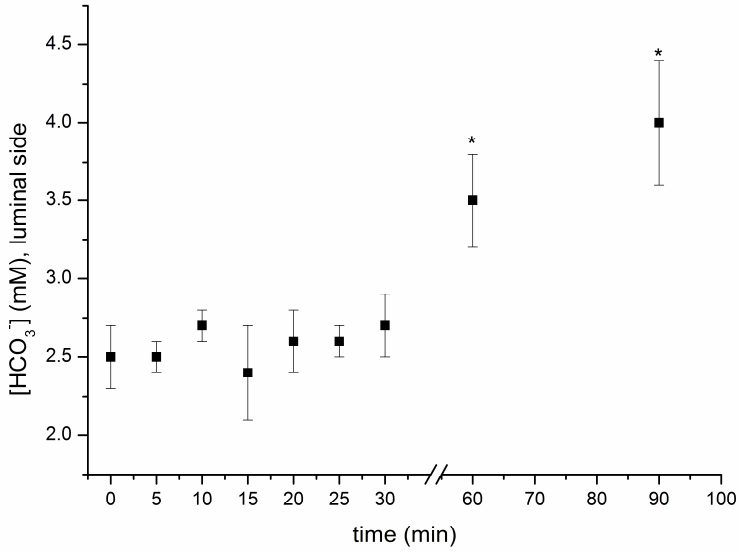

Figure 44 Luminal HCO_3^- concentration during 90 min application of a 118 fold HCO_3^- gradient. After 60 min the concentration became significantly different from the control value. The permeability coefficients were determined for the first 30 min (n = 6) and for the last 60 min (n = 2). The coefficient increased from 1.0 ± 2.0 x10^{-5} cm s^{-1} to 3.1 ± 0.6 x10^{-5} cm s^{-1}. Mean values are given ± SEM (*n* = 4), repeated measurement ANOVA ($F_{(8,23)} = 11$, $p = 0.02$, Greenhouse Geisser corrected).

3.2.1.3 Diffusion potential measurements

The slight lumen negative transepithelial potential was shifted by 4.6 ± 0.6 mV (n = 7) to a positive value when low NaCl-ASW was applied on the luminal side (Figure 45). Basolateral application of this solution shifted the V_{te} by -1.3 ± 0.2 mV (n = 7) (Figure 45).

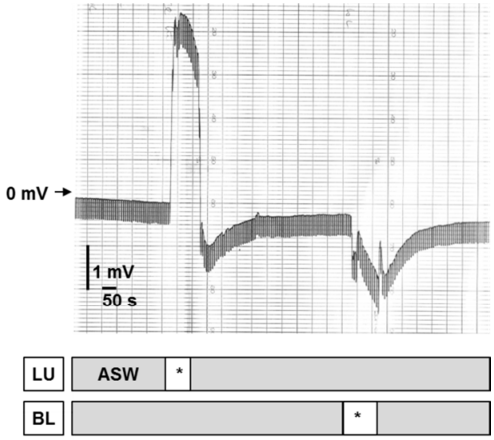

Figure 45 V_{te} changes of the intestine caused by an application of low NaCl-solution, marked by an asterisk (lu = luminal, bl = basolateral).

3.2.1.4 Stimulation of V_{te}

The basolateral stimulation of the transepithelial potential with FSK/IBMX (0.1 µM/100 µM) and 100 µM ATP was not continued as they were insignificant in pilot experiments (Table 16).

The intestine exhibited a change in electrogenic transport when glucose was applied on the luminal side (Figure 46). As a result, the transepithelial potential decreased to -0.6 ± 0.1 mV, the resistance increased to 16.6 ± 3.8 Ωcm^2 and I'_{SC} was changed to -37.6 ± 5 µA cm^{-2} (n = 8).

Table 16 Effect of basolateral and luminal stimulation on the intestine electrophysiological parameters. The following concentrations were used: FSK/IMBX: 0.1 µM/100 µM, basolateral (n = 2), 100 µM ATP, basolateral (n = 2), glucose: 5 mM, luminal (n = 8). Mean values are given ± SEM and significant differences are indicated by different letters (paired t-test, t_1 =-1 - 1.3, t_7 = 4.1, $p < 0.05$).

	Resistance (Ωcm^2)		Transepithelial voltage (mV)		Short circuit current (µA (cm^2)$^{-1}$)	
Control	11.3 ± 3.8	a	-0.1 ± 0.01	a	-11.6 ± 5	a
FSK/IBMX	10.0 ± 2.5	a	-0.2 ± 0.05	a	-17.3 ± 9.3	a
Control	11.3 ± 3.8	a	-0.1 ± 0.1	a	-5 ± 5	a
ATP	9.4 ± 1.9	a	-0.1 ± 0.1	a	-4.4 ± 4.4	a
Control	12.1 ± 0.1	a	-0.3 ± 0.1	a	-22.5 ± 5	a
Glucose	16.6 ± 3.8	a	-0.6 ± 0.1	b	-37.6 ± 5	b

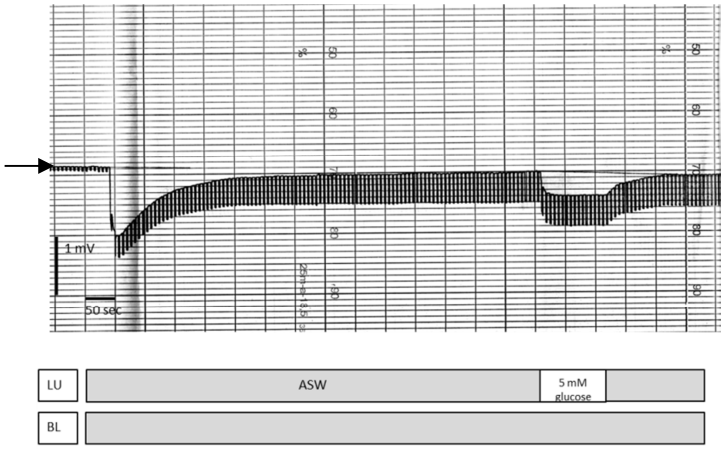

Figure 46 5 mM glucose application on the luminal side revealed a lumen negative potential. The arrow indicates 0 mV (lu = luminal, bl = basolateral).

3.2.2 Properties of the peritoneal epithelium

3.2.2.1 Histology

The peritoneal epithelium appeared as a thin (± 5 µm thick) epithelium with a dominant basal membrane and processes towards the stroma (Figure 47). The FM®1-43 staining showed that the dissection method did not damage the thin tissue and that the cells possess cilia on the luminal side (Figure 48) marking them presumably as peritoneocytes as known in ophiuroidea (Byrne, 1994).

Figure 47 HE-staining of the peritoneal epithelium. The basal membrane (basolateral) is stained in rose, the peritoneocytes are purple.

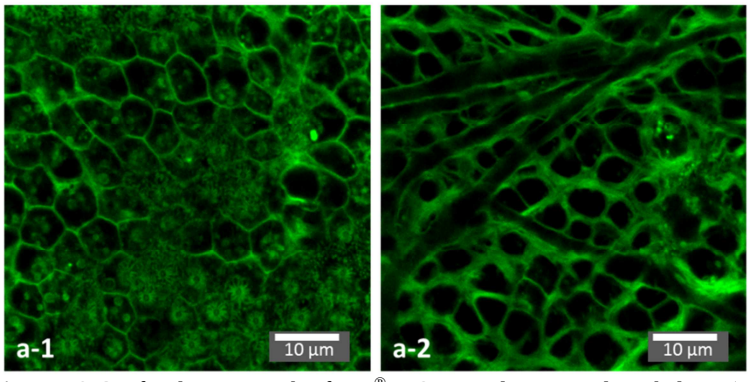

Figure 48 Confocal micrograph of FM®1-43 stained peritoneal epithelium (1 µm stacks). (a-1) gives an example of the luminal side (PCF facing) where cilia are visible and (a-2) shows the connective tissue of the basolateral side (stereom facing).

3.2.2.2 Electrical properties

The peritoneal epithelium was characterised by a small R_{te} of 0.8 ± 0.1 Ωcm^2 (n = 39) which is almost at the detection limit of the Ussing-chamber technique. The low R_{te} reflects a virtually leaky epithelium for ions and therefore no measurements of V_{te} as calculation of active ion transport were done.

3.2.2.3 Barrier properties

Barrier property investigations were conducted with differently sized-FITC dextrans and free FITC. The peritoneal epithelium revealed size selectivity: no molecules > 0.3 kDa could pass the barrier. For 90 min the size selectivity remained stable (Figure 49) and the epithelium was not damaged by the dissection method.

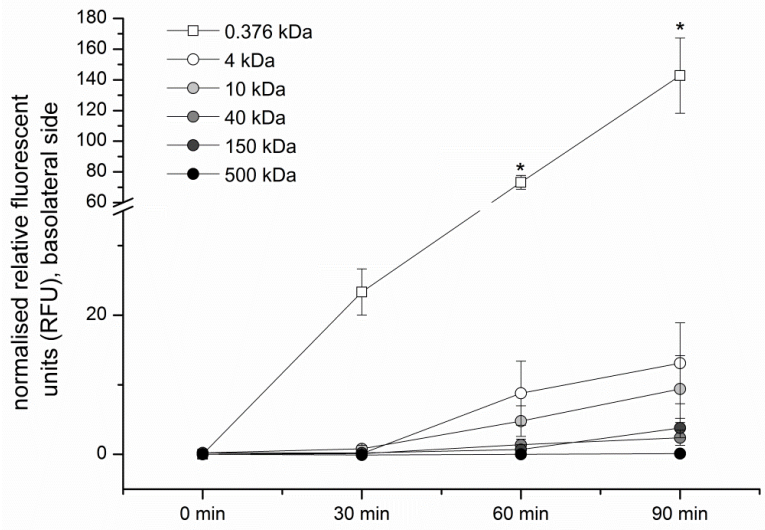

Figure 49 FITC-diffusion properties across the peritoneal epithelium after 30, 60 and 90 min. FITC and its dextran-derivatives were applied on the luminal side and the relative fluorescence intensity (RFU) at the basolateral side was measured. Mean values are given ± SEM (n = 4-6). Significant differences are marked with an asterisk, repeated measurement ANOVA ($F_{(4,11)} = 11$, $p = 0.01$ for 0.3 kDa, Greenhouse Geisser corrected).

3.3 Effects of ocean acidification on adult skeletal elements

I addressed the question whether dissolution of inner ossicle parts could contribute to the acid-base regulation of PCF in hypercapnic stressed sea urchins. In addition to ossicles, also the spine surface was analysed with SEM. In addition to this, the stability of skeletal elements was investigated in control and hypercapnically-stressed animals and I examined the effect of increased pCO_2 on ossicle growth.

3.3.1 Scanning electron microscopy

3.3.1.1 Ossicles

Under all treatments, the overall appearance of ossicles did not change. Thus, no visible differences in the stereom structure were detectable and also newly calcified parts of the longitudinal growing zones were not distinguishable from older stereom parts (Figure 50).

When the different regions along the latitudinal ossicle axis were highly magnified, differences of the ossicle surface appeared in form of small granular structures (height = ± 0.1 µm; diameter = 0.09 ± 0.0 µm, n = 180; Figure 50). Under control conditions, 12 % of the ossicles were characterised by these

structures and the proportion increased to 50% (Table 17). In the following calculation I assumed the amount of released CO_3^{2-} to be able to increase $[CO_3^{2-}]_{PCF}$ by 0.21 mM in control and 0.84 mM in intermediate and high CO_2 treatment.

Calculation of dissolution

Assumptions:

Sea urchin diameter:	3.2 cm (based on *n* = 10)
Volume of perivisceral coelomic fluid:	2.6 ml (based on *n* = 10)
Height of granular structures:	100 nm (based on *n* = 180)

First, the volume of dissolved material was calculated under the assumption that 100 nm of ossicle thickness over the whole surface is dissolved and that 50% of ossicle volume consists of $CaCO_3$.
The density of calcite is 2.71 g $(cm^3)^{-1}$ and was used to calculate the amount of dissolved $CaCO_3$ and the respective concentration increase of CO_3^{2-} (Equation 9 and 10).

$$CaCO_3\ mass\ (g) = volume \times density$$

$$CO_3^{2-}(M) = \frac{\left(\frac{CaCO_3(g)}{molar\ mass\ CaCO_3\ (g\ mol^{-1})}\right)}{CF\ volume\ (L)}$$

Equation 9 and 10

This would result in a concentration increase by 1.68 mM of dissolved CO_3^{2-} if the whole surface was eroded.
Taking into account that the SEM analysis revealed that 50% of the highest, 50% of the intermediate and 12.5% of the control CO_2 treated ossicles exhibited pitted surfaces, the following increases in CO_3^{2-} concentration were calculated:

High CO_2 treatment, released CO_3^{2-} :	0.84 mM
Intermediate CO_2 treatment, released CO_3^{2-} :	0.84 mM
Control CO_2 treatment, released CO_3^{2-} :	0.21 mM

At the given pHs of PCF for the three CO_2 treatments, it can be further assumed that most of the released CO_3^{2-} is available as HCO_3^-.

3.3.1.2 Spines

In spines, the outer surface was also altered dependent on pCO_2. The alterations were more prominent compared to the inner ossicle surface and increased from 17% (control) to 100% (high pCO_2) (Figure 50, Table 17). The thickness of whole spines and the spine septa did not change between the

treatments (Table 17).

Table 17 Distribution of surface alterations and spine thickness in response to CO_2-treatment (control = 47 Pa, intermediate = 102 Pa, high = 284 Pa). Data for the surface integrity is given as percentage distribution for either whole ossicles or for spines in response to pCO_2 (ossicles = summarised from four measured regions; $n_{control}$ = 6, $n_{intermediate}$ = 9, n_{high} = 12; n_{spines} = 6). Different letters in a row indicate significant differences (one-way ANOVA), mean values are given ± SEM.

		pCO_2						One-way ANOVA	
		control		intermediate		high		F	p
percentage distribution of surface alteration (%)								$F_{(2,9)}$	
whole ossicles	smooth	88	a	50	b	50	b	7.92	0.01
	pitted	12	a	50	b	50	b	9.48	0.01
spine surface	smooth	83		50		0			
	dissolved	17		50		100			
spine thickness (µm)								$F_{(2,15)}$	
	total spine	514 ± 20	a	512 ± 23	a	529 ± 22	a	0.19	0.83
	spine septa	53 ± 5	a	52 ± 3	a	51 ± 4	a	0.04	0.96

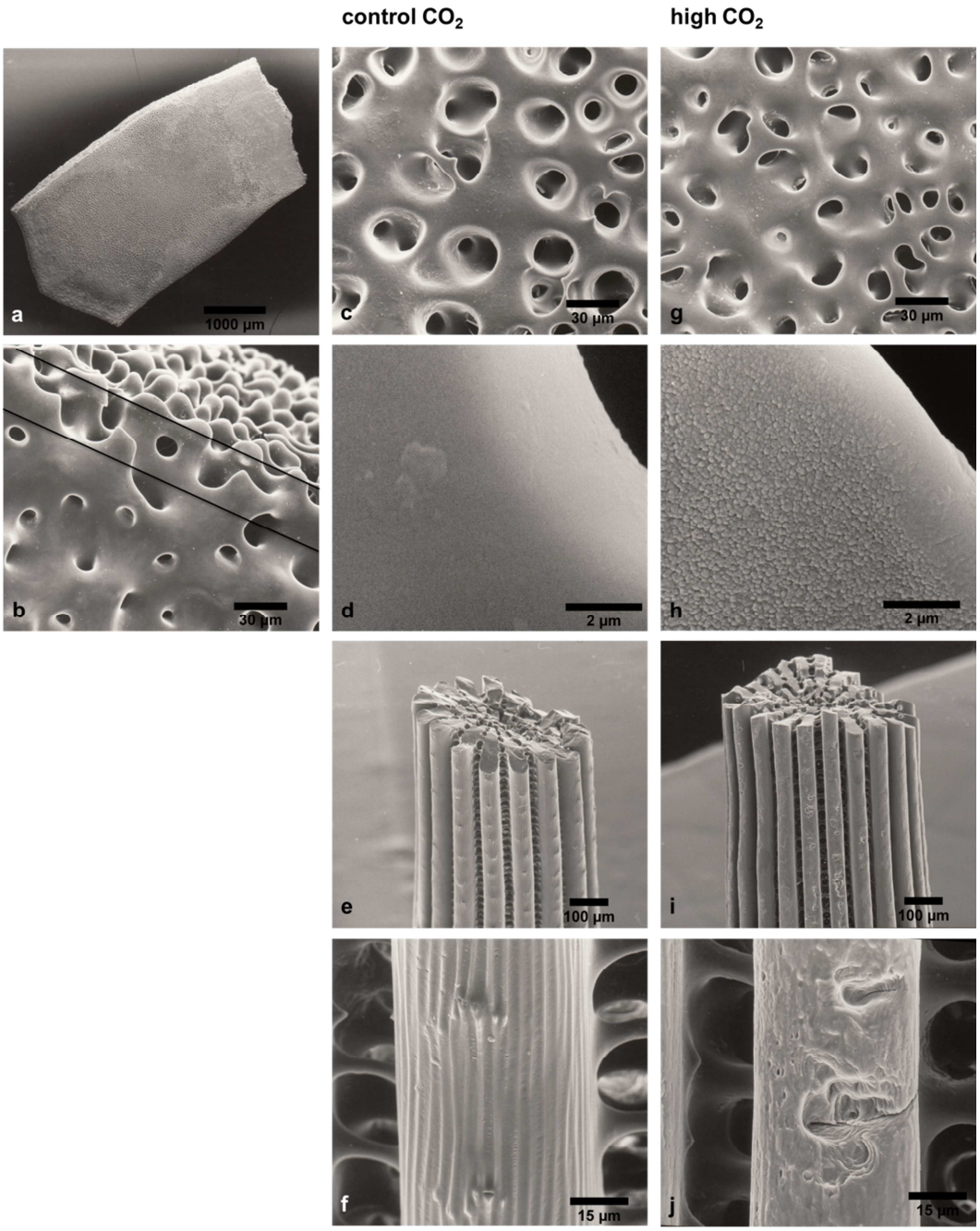

Figure 50 SEM-analysis of ossicles and spines after 6 week exposure to different pCO_2 (47, 102 and 284 Pa). (a) and (b) give a typical ossicle and stereom structure. (b) Growth increment (region between lines) of one ossicle under intermediate pCO_2 (102 Pa) incubation within 6 weeks. (c), (d), (e) and (f) examples of ossicle and spine surface structure for control condition (47 Pa); (g), (h), (i) and (j) show the same for high CO_2 conditions (284 Pa). In (d) a typical smooth surface of the control treatment is shown in contrast to the pitted structure which is found in 50% of the ossicles grown under high CO_2 conditions (h) (Table **17**). Spine surface structure of a sea urchin maintained at control conditions (e, f) appears smooth compared to the surface structure of spines from sea urchins maintained at high pCO_2 (i, j). The thickness of the radially arranged septa was not significantly different from each other (Table 17).

3.3.2 Mechanical resistance of adult skeletal elements

3.3.2.1 Ossicles

Single ossicles

Stability of single ossicles was not changed between the treatments; however, a slight trend of decreased stability was observed (Figure 51, Table 18). The breaking force ranged from 5.3 ± 0.3 N (*n* = 6, control pCO_2) to 4.8 ± 0.3 N (*n* = 6, high pCO_2) (one-way ANOVA, $F_{(2,15)} = 0.50$, p = 0.61).

Ossicle junctions

The mechanical resistance measurements of the ossicle junctions revealed the following: under control conditions 4.1 ± 0.6 N (*n* = 6) had to be applied before the junctions broke. The needed force was reduced in both hypercapnia conditions (2.1 ± 0.4 N, *n* = 6; 2.9 ± 0.4 N, *n* = 6; intermediate and high pCO_2, respectively) but based on the large scattering of single measurements (Figure 51) only the intermediate pCO_2 force was significantly different from the control value (one-way ANOVA $F_{(2,15)}$ = 4.9, p = 0.02; Table 18).

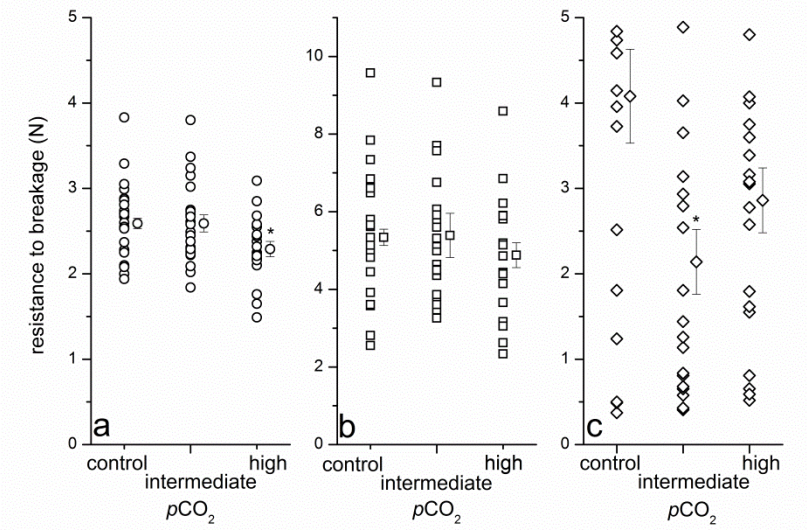

Figure 51 Distribution of the breaking force of all measured spines (a, open circles; only lengths of 5-8.6 mm were used for the analysis), ossicles (b, open squares) and ossicle junctions (c, open diamond). The mean values, given ± SEM, of true replicates are shown next to the respective distributions. *n* for distribution data: spine = 20-24, single ossicles =18-23, ossicle junctions = 18-20; *n* for mean values = 6. Significant differences are indicated by an asterisk, one-way ANOVA, spines: $F_{(2,15)} = 3.98$, p = 0.04, single ossicles: $F_{(2,15)} = 0.5$, p = 0.61, ossicle junction: $F_{(2,15)} = 4.9$, p = 0.02.

3.3.2.2 Spines

The highest pCO_2 treatment caused a significant drop in spine stability (2.3 ± 0.1 N compared to 2.6 ± 0.1 N under control conditions; one-way ANOVA $F_{(2,15)} = 3.98$, p = 0.04) (Figure 51, Table 18).

These measurements were only conducted with spines in the range of 5-8.6 µm. This was due to the fact that initial spine lengths in the three treatments were significantly different from each other

(control: 8.5 ± 0.2 mm (n = 28), intermediate: 8.6 ± 0.2 mm (n = 28), high: 7.0 ± 0.1 mm, n = 20, one-way ANOVA, $F_{(2,73)} = 17.76$, $p = 5.2 \times 10^{-7}$).

Table 18 Fracture force as a measure of breaking resistance in response to CO_2-treatment (control = 47 Pa, intermediate = 102 Pa, high = 284 Pa). The breaking force-data are given as true replicates for single ossicles and spines (n = 6). For the raw data distribution of ossicles and spines see Figure 51.

	pCO_2						one-way ANOVA	
	control		intermediate		high		$F_{(2,15)}$	p
fracture force (N)								
single ossicles	5.3 ± 0.2	a	5.4 ± 0.6	a	4.9 ± 0.3	a	0.50	0.61
ossicle junctions	4.1 ± 0.6	a	2.1 ± 0.4	b	2.9 ± 0.4	a	4.9	0.02
spines	2.6 ± 0.1	a	2.6 ± 0.1	a	2.3 ± 0.1	b	3.98	0.04

3.3.3 Ossicle growth

Ossicles grow along the longitudinal and latitudinal zones. These zones were investigated independently from each other and will be presented in two distinct sub-chapters.

3.3.3.1 Longitudinal ossicle growth

The longitudinal growth of ossicles was first assigned to three different categories describing whether calcein incorporation was visible or not and if growth was detectable. The proportion of ossicles within the non-labelled category was low (< 13% in the regions aboral I and II, < 21% in the oral region) in all treatments whereas the proportion of non-detectable growth was increasing towards the oral ossicles and with increasing pCO_2 (Table 19).

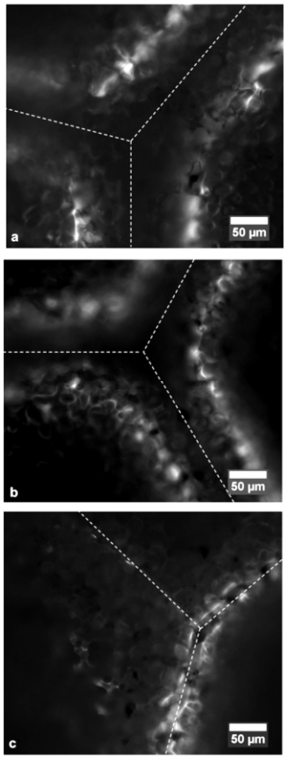

Figure 52 Calcein incorporation into ossicles. The calcein labelling is given in white; the dotted lines indicate the junctions between two plates (compare with c). (a) Increment of growth under control conditions (47 Pa) in the region aboral I; (b) shows the increment at intermediate pCO_2 (102 Pa) in the same region and the increment under high CO_2 (284 Pa) is shown in (c) for the region aboral II.

However, in all treatments ossicle growth was detectable by separate calcein bands as depicted in Figure 52. Growth of *e.g.* region aboral II revealed a daily growth of 1.4 ± 0.2 µm d^{-1} (n = 6) under control conditions which decreased significantly under intermediate and high pCO_2 (0.9 ± 0.1 µm d^{-1}, 0.2 ± 0.1 µm d^{-1}, respectively, n = 6 in each treatment, one-way ANOVA $F_{(2,15)} = 26.83$, $p = 1.1 \times 10^{-5}$; Figure 53). Similar results were achieved for the region aboral I, the oral region showed virtually no growth under intermediate and high pCO_2 and was only detectable in 6% of the analysed ossicles (Table 19).

3.3.3.2 Latitudinal ossicle growth

During the measurement of latitudinal ossicle growth the categories for growth and labelling were applied (chapter 2.3.1.4). The general pattern, already described in the previous chapter, could be confirmed. However, the amount of "no fluorescence" increased and in the oral ossicles no successful measurements could be observed, independent of the pCO_2 treatment (Table 19).

The increment in growth was also lower compared to longitudinal ossicle growth (Figure 53) but showed the same general pattern in terms of pCO_2 dependency.

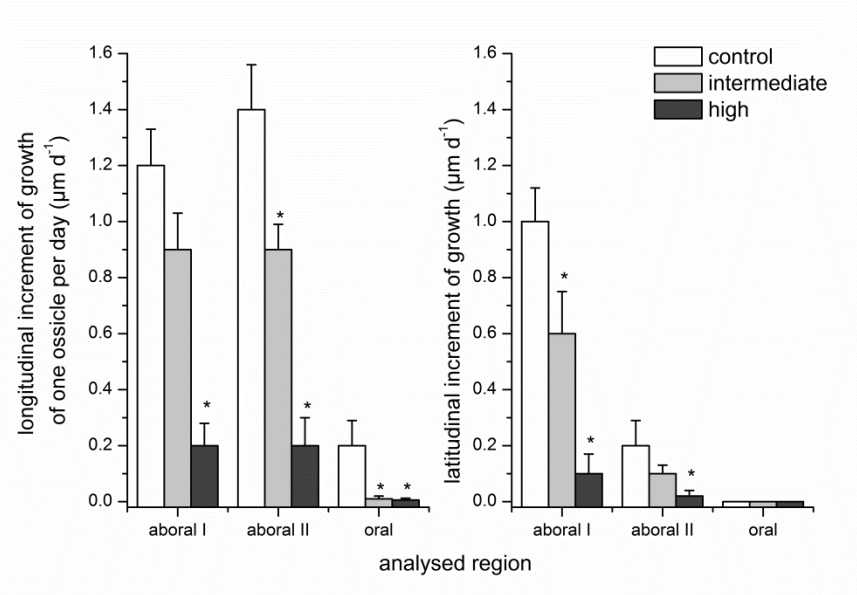

Figure 53 Comparision of longitudinal and latitudinal growth of ossicles according to region and CO_2 treatment. In general, growth of the longitudinal region was higher compared to the latitudinal region. In addition, growth decreased towards the oral part of the test and was negatively affected by hypercapnia. Mean values are given ± SEM; $n_{long.} = 6$, $n_{latit.} = 6$ (one-way $ANOVA_{longitudinal}$, $F_{(2,15)} = 5.5$ -26.8, $p < 0.05$; one-way $ANOVA_{latidunial}$, $F_{(2,15)} = 3.7$-15.3, $p < 0.05$).

Table 19 Category assignment of ossicle longitudinal and latitudinal growth measurements and percentages of ossicles falling under the three categories “growth”, “no growth” and “no labelling” in the three regions aboral I, II and oral. The first category “growth” described successful calcein labelling and detectable growth. In “no growth” calcein labelling was successful, however, growth could not be measured. The third category “no labelling” included ossicles without a calcein signal at the growing side. The category “growth” decreased from aboral to oral and with increasing pCO_2. The percentage of "no growth" increased with increasing pCO_2. Calcein labelling was not dependent on these conditions. (n =15-19)

	longitudinal growth aboral I			latitudinal growth aboral I		
	control pCO_2	intermediate pCO_2	high pCO_2	control pCO_2	intermediate pCO_2	high pCO_2
growth (%)	84	83	38	84	76	19
no growth (%)	11	11	50	5	18	69
no labelling (%)	5	6	13	11	6	13
	aboral II			aboral II		
	control pCO_2	intermediate pCO_2	high pCO_2	control pCO_2	intermediate pCO_2	high pCO_2
growth (%)	89	89	50	53	44	6
no growth (%)	5	6	50	42	50	56
no labelling (%)	5	6	0	5	6	38
	oral			oral		
	control pCO_2	intermediate pCO_2	high pCO_2	control pCO_2	intermediate pCO_2	high pCO_2
growth (%)	37	6	6	0	0	0
no growth (%)	42	78	88	78	83	67
no labelling (%)	21	17	6	22	17	33

4 Discussion

In the following paragraphs I will first discuss the cellular processes involved in larval calcification before discussing the perivisceral coelomic fluid (PCF) buffering and the effect of ocean acidification on adult *S. droebachiensis*.

4.1 Cellular mechanisms involved in larval calcification

To study the effect of loop diuretics and other transport protein inhibitors, sea urchin larvae were incubated with different inhibitors blocking NKCC, L-type Ca^{2+} channel, Ca^{2+} ATPase, V-ATPase, anion transport mediated by the SLC4-family and H^+K^+ ATPase. The incubations were predominantly conducted for 48 h, starting at the prism stage, but also other larval stages were incubated (Table 3). I could show that incubation with loop diuretics inhibited the elongation of the primary body rod and the maintenance of the cytoplasmic cord covering the spicules but did neither affect the vitality, swimming behaviour nor the overall shape of the larvae. In contrast to this, the treatment of larvae with other inhibitors resulted in an affected development and vitality, combined with an impaired calcification. In addition, I could demonstrate the expression of a *sd*-NKCC homolog on the mRNA level.

4.1.1 Methodological discussion

4.1.1.1 Measured parameters and identification of toxic side effects

To address the cellular mechanisms, I incubated larvae to different drugs and measured primarily the length of the primary body rod. As this rod, in contrast to both arm-rods, is not affected by different food regimes (McEdward and Herrera, 1999; Miner, 2005; Adams et al., 2011), the non-feeding of larvae was considered not to cause any artefacts on the calcification measurements.

Based on the concentration response experiments I have done for loop diuretics, I used azosemide for more detailed studies in a supra-maximal concentration of 50 µM because it was a major goal of this study to understand the involvement of NKCC within the process of calcification.

Besides the measurement of calcification I monitored the vitality of larvae prior to fixation and measured the gastrulation index (GaJ %) and the morphometrics of 120 h old larvae. These diverse methods allowed the detection of a broad range of possible toxic side effects caused by the different drugs. To evaluate the applicability of the different drugs in whole larvae assays, it was essential to detect non-calcification related toxic side effects and to exclude certain drugs from further investigations.

I could show that treatments with loop diuretics did not cause any toxic side effects. However, toxic side effects were caused by the non-loop diuretic drugs indicated by the concentration-dependent

immobility, decreased vitality and death when the larvae were incubated in one of these drugs used (Table 10). The presence of toxic side effects of non-loop diuretics was further confirmed by the inhibition of gastrulation (Figure 25, Figure 26) and by the strong impact on pluteus development (Figure 27, Figure 28). Loop diuretics also caused significant changes of the body and antero-lateral length and width; however, the larvae were still shaped normally as shown in the antero-lateral/body length ratio (Figure 28). These changes in the measured parameters were presumably related to the reduced spicule length and to minor effects of NKCC-inhibition on cell migration/volume regulation of ectodermal cells. Specifically for azosemide, the swimming behaviour, feeding and metamorphosis into juveniles was also investigated and was not different between control and azosemide treatment (Table 10, Figure 25, Figure 28, Figure 29).

Concluding, these results indicate that loop diuretics do not cause severe metabolic side effects and are therefore appropriate to be used in whole larvae assays. In contrast, non-loop diuretics cannot be used in whole larvae assays to address their impact on calcification as they cause severe and most likely unspecific effects on development and vitality. Based on this non-specificity, no IC_{50} were calculated for non-loop diuretic drugs.

4.1.1.2 Drug concentrations

So far, rather high concentrations of different drugs have been used in sea urchin research (in case of furosemide up to 4 mM, Yasumasu et al., 1985; Table 20). However, the risk of side effects increases with increasing concentration as unspecific bindings to other proteins or transporters are more likely. For example, ethacrynic acid, a loop diuretic which has been used in sea urchin experiments, inhibits NKCC specifically, but at concentrations > 100 µM it also blocks ATPases (Beyer et al., 1965; Burg and Green, 1973a).

Toxic side effects on development have been reported for the inhibition of L-type Ca^{2+} channels (Fujino et al., 1985; Yasumasu et al., 1985; Dale et al., 1997), DIDS applications (Fujino et al., 1985; Yasumasu et al., 1985) and the inhibition of H^+K^+ ATPase *via* omeprazole (Fujino et al., 1987). Although I worked with lower, pharmacologically more relevant concentrations, all non-diuretic drugs induced severe toxic effects on larval vitality and development whereas loop diuretics specifically targeted spicule calcification.

Table 20 Summary of used inhibitors in this study and in previous sea urchin studies. In addition, IC_{50} gained in sea urchin studies and in other model systems are summarised as well as maximal concentrations. Due to side effects on development, no IC_{50} values are given for non-loop diuretic drugs. The increment in primary body rod growth refers to the initial body rod length. Previous sea urchin studies used high concentrations to determine effects on calcification. Although in case of DIDS the maximum concentrations are similar to other literature values the concentration used for determining the effect on $^{45}Ca^{2+}$ uptake into embryos was beyond IC_{50} values (100 µM DIDS, 100 µM verapamil Fujino et al, 1985)

inhibitor	inhibition of	literature values for IC_{50} (µM)	IC_{50} (µM) (this study)	literature values for max. concentrations (µM)	maximum concentration used in sea urchin larvae before (µM)	used maximum concentration (µM) (this study)
furosemide	NKCC2	3 [4]; 7 [5a]	315.3	500 [6,17]	1000 [2]; 2000 [1]; 4000 [3]	500
	NKCC1	9.1 [5b]; 14.8 [17]				
bumetanide	NKCC2	0.2 [4]; 0.3 [5a,b]	26.48	100 [6,17]		100
	NKCC1	0.3 [5a,b]; 7.4 [17]				
azosemide	NKCC2	3 [4]	6.38	100 [6,17]		50
	NKCC1	20 [6]; 1.2 [17]				
concanamycin A	V-ATPase	0.009 [7]; 0.009 [8a]; 0.01 [8b]		1 [7]; 0.05 [8]		0.1
cyclopiazonic acid	Ca^{2+} ATPase (intracellular Ca^{2+} storage sites)	0.6 [9]		10 [9]		30
DIDS	anion exchange	50 [10]; 0.08 - 2 [11a]; 0.43 - 280 [11b]		200 [10]	300 [1]; 40 [3]	20
omeprazole	H^+K^+ ATPase	0.25 [12a]; 200 [12b]; 0.47 [13]		300 [12]; 10 [13]	400 (non-activated)[18]	200 (pre-activation)
verapamil	Ca^{2+}channel	0.6 [14]; 16 [15]		10 [14]; 100 [15]	300 [1]; 100 [3]	25

[1] Fujino et al., 1985; [2] Mitsunaga et al., 1986c; [3] Yasumasu et al., 1985; [4] Greger, 1995, NKCC2 in TAL; [5] Hannaert et al., 2002, a NKCC2 in mTAL, b by hypertonic medium activated NKCC1 in erythrocytes; [6] Ecke et al., 1996, isolated colon crypts; [7] Muroi et al., 1993, yeast vacuole membrane culture; [8] Nishihara et al., 1995, ED_{50}-values, a B-lymphoma cell culture, b Myeloma-cell; [9] Uyama et al., 1992, skinned smooth muscle of guinea-pig ileum; [10] Pappone and Lee, 1995, rat brown adipocytes; [11] summarised by Cabantchik and Greger, 1992, a human red blood cells, b various systems; [12] Mattsson et al., 1991, a isolated rabbit gastric glands, b hen medullary bone membrane vesicles; [13] Morii et al., 1990, hog gastric vesicles; [14] Matsuoka et al., 1991, guinea-pig ventricular myocytes; [15] Tambutté et al., 1996, warm-water coral branches; [17] Warth et al., 1998, inhibition of I_{SC} in renal gland tubules of *Squalus acanthias*; [18] Fujino et al., 1987

4.1.1.3 Identification of sea urchin NKCC homologies to other known NKCC1-sequences

Based on the incompleteness of the *sd*-NKCC sequence, a phylogenetic tree was calculated with the known *sp*-NKCC sequence. However, the identified *sd*-fragments have been shown to be closely related to *sp*-NKCC (chapter 3.1.6) and thus no severe differences in aligning *S. purpuratus* or *S. droebachiensis* with NKCC-isoforms of other species are expected. This was further proven by aligning the translated protein sequence of product 6 to the corresponding fragments of other species and a similar phylogenetic tree compared to Figure 42 resulted.

The homology of *sp*-NKCC to other NKCC sequences of different vertebrata species revealed that sea urchin NKCC presumably diverged early in the evolution of NKCC as it has also been shown for insect NKCC (Delpire et al., 1996; Pullikuth et al., 2003; Gillen et al., 2006). Thus no relation of sea urchin NKCC to the first or second NKCC isoform is found. An early evolutionary diversion is also known for sea urchin Na^+K^+ ATPase alpha-subunit which diverged before the splitting of three known Na^+K^+ ATPase isoforms (Mitsunaga-Nakatsubo et al., 1996).

Using *sd*- and *sp*-NKCC sequences did not result in any NKCC-related hit in EST-library searches. The EST-library may be incomplete with regard to NKCC based on presumably low expression of the target mRNA.

In situ hybridisation failed in *S. droebachiensis* larvae. Two explanations for this are possible: either the gene expression is too low to be detected by *in situ* hybridisation during larval development or another, yet unknown, isoform of this gene may generate the phenotype observed in the inhibition experiments.

4.1.1.4 Calcein staining of vesicles

To test if ACC-rich vesicles can still be produced in the presence of azosemide, I adopted the calcein-staining method from Wilt et al. (2008) and the bag fraction production from Harkey and Whitney (1980) since it has been reported that unbound calcein within the body cavity of whole larvae cannot be washed out (Wilt et al., 2008). This adoption worked well as the bag isolation presumably produced small ruptures within the basal lamina and thus calcein was washed away.

The assumption that the calcein labelled vesicles are rich in calcium or ACC is based on the observations of Wilt et al. (2008) and was not further proven in this studies with methods like Raman spectroscopy in case of ACC (Weiner et al., 2003). However, during analysis, the vesicles were observed to be trafficking along the cytoplasmic cords and, similar as in Wilt et al. (2008), calcein staining of the spicules was observed. This allows the conclusion, in accordance to Wilt et al. (2008), that calcium is precipitated in vesicles prior to spicule elongation.

4.1.1.5 Western blot analysis and immunohistochemistry

The monoclonal antibody (T4, DSHB) revealed a clear signal in sea urchin larvae, whereas the polyclonal antibody (GeneTex) showed a rather diffuse pattern, although the same structures had been stained. Thus, the monoclonal antibody was shown to work better in sea urchin larvae. A clear signal in ectodermal cells could be detected. This is in alignment with the intracellular volume regulatory function of NKCC; due to changes in seawater salinity the ectodermal cells might have to activate RVI. Also the digestive tract, PMCs, cytoplasmic cord and filopodia were stained.

The signal in PMCs and cytoplasmic cord plasma membrane is in alignment with the assumed function of NKCC in sea urchins; however, the Western blot analysis with the DSHB antibody and the GeneTex antibody failed to generate a signal for sea urchin NKCC at the expected size of 119 kDa. This can be based on the denaturation of proteins during sample preparation or on the total protein

concentration used, which might have been too low for the antibody detection, although 5 µg protein was used for the colon sample and 4-32 µg protein for the different larval samples were used.

Both antibodies were able to stain protein in mouse colon, although major bands were not detected at the expected size (130 kDa). Staining bands of different sizes can be based on different phosphorylation states of the cotransporter and formation of dimers. In addition, N-linked glycosylation can cause smears (Matskevich et al., 2005). However, without having control tissue of an NKCC-knockout it can only be assumed that the monoclonal antibody stains NKCC in the tested tissues.

The antibody T4 has been shown to specifically stain NKCC in sea urchin coelomocytes (D'Andrea-Winslow et al., 2001) and thereby it is assumed that it is also useful in sea urchin larvae. By generating an intensity profile (Figure 54) it becomes visible that the cytoplasmic cord intensity is similar to the ectoderm intensity. In other pictures (Figure 41e) the cytoplasmic cord intensity was even brighter compared to the ectoderm.

Concluding, the immunohistochemistry signal of the GeneTex antibody cannot be used for NKCC localisation but the DSHB-antibody nicely shows the probable location within sea urchin larvae. However, the signals have to be taken with caution since the confirmation of antibody-protein binding was not successful in Western Blot analysis.

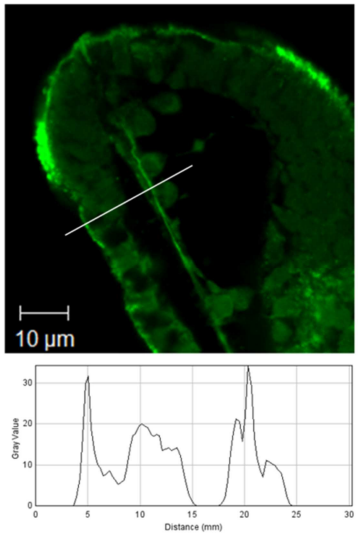

Figure 54 Intensity profile (grey scale) of T4-staining. The profile is given for the white line and was conducted in ImageJ.

4.1.2 NKCC vs. $Cl^-HCO_3^-$ ATPase in sea urchin calcification

Based on inhibition studies with loop diuretics (furosemide and ethacrynic acid; Mitsunaga et al., 1986b, 1986c, 1987a), Mitsunaga et al. (1987a) proposed that a $Cl^-HCO_3^-$ ATPase contributes to calcification in sea urchin larvae. It has been shown in mammalian TAL studies that such an ATPase does not exist (Greger, 1981; chapter 1.2.3) and that loop diuretics target the NKCC cotransporter. However, these findings have never been transferred to sea urchin calcification research.

Interestingly, most of the data, which were interpreted as evidence for the ATPase, would also be compatible with the NKCC cotransporter as the primary target of the drug. In the following some arguments are presented which speak against the theory of a $Cl^-HCO_3^-$ ATPase.

Ethacrynic acid was used in concentrations up to 1 mM (Mitsunaga et al., 1986b, 1987a) and was shown to inhibit Ca^{2+}-incorporation (measured as $^{45}Ca^{2+}$ incorporation in spicules) and ATPase activity (measured as the rate of P_i liberation in the presence of ouabain and in the presence or absence of ethacrynic acid). However, ethacrynic acid unspecifically inhibits ATPases at concentrations > 100 µM (Beyer et al., 1965; Burg and Green, 1973a). This could explain the measured effect on ATPase activity, *e.g.* Na^+K^+ ATPase or a putative vesicular Ca^{2+} ATPase, seen by Mitsunaga and coworkers.

It has been shown that the measurable "Cl^- ATPase activity" is dependent on Cl^- and can be enhanced by the addition of $KHCO_3$, $NaHCO_3$, NaCl, KCl and NH_4Cl (Mitsunaga et al., 1986b, 1986c). These additions involved ions which are needed for the function of NKCC (Na^+, K^+, Cl^-) or can be transported (NH_4^+) (Kinne et al., 1985; Loong et al., 2012). Although NKCC does not accept HCO_3^-, the additional uptake of a calcification relevant substrate could stimulate a putative vesicular Ca^{2+} ATPase.

The ATPase-activity was measured in a standard reaction mixture containing ouabain which normally inhibits Na^+K^+ ATPase. The activity of this ATPase is coupled to the NKCC: inwardly transported sodium is pumped out of the cell *via* the ATPase (Figure 10). However, an unspecific Na^+K^+ ATPase inhibition by loop diuretics is also favourable as 2-3 mM ouabain seems to have no effect on sea urchin calcification (Mitsunaga et al., 1987b, 1989). This is astounding as the Na^+K^+ ATPase is known to be essential for cellular physiology (chapter 1.2.1). A possible explanation might be that some Na^+K^+ ATPase isoforms are insensitive to the ouabain. In mammals, the tissue specific isoform of the alpha-subunit of the Na^+K^+ ATPase is determining the sensitivity to this drug (Sweadner, 1985, 1989; Lingrel, 1992). As mentioned above, the sea urchin Na^+K^+ ATPase alpha-subunit genetically diverged early in evolution before the splitting into the three isoforms (Mitsunaga-Nakatsubo et al., 1996). The IC_{50} for ouabain of sea urchin Na^+K^+ ATPase of ~1 mM (Mitsunaga et al., 1986b, 1991) is higher compared to the IC_{50} of 320 µM of rat kidney (ouabain-insensitive alpha 1 isoform; Lingrel, 1992). This correlates to a ouabain insensitivity of this Na^+K^+ ATPase isoform.

In conclusion, the hypothesis of a $Cl^-HCO_3^-$ ATPase, also for sea urchin physiology, has to be abandoned in favour of an NKCC cotransporter. Whereas there has never been a molecular proof for the existence of the ATPase, NKCC cotransporters are well established members of the SLC12 family (*e.g.* Hebert et al., 2004) and sea urchin homologous have been described at the expression and functional level (D'Andrea-Winslow et al., 2001; Ji et al., 2008; Todgham and Hofmann, 2009; Tu et al., 2012).

4.1.3 NKCC is involved in larval calcification of *Strongylocentrotus droebachiensis*

Having discussed the molecular identity of the loop-diuretic inhibitable ion transport and assuming that the respective ion transport is mediated by an NKCC homolog (chapter 4.1.1.3), the physiological role of this transporter in sea urchin larval calcification will be discussed in the next sections.

That loop diuretics act specifically on sea urchin calcification could be confirmed by the incubation experiments. In addition, I could show that *sd*-NKCC is most sensitive for azosemide and less sensitive for bumetanide and furosemide - a characteristic sequence for mammalian NKCC1 (Ecke et al., 1996; Warth et al., 1998; Greger, 2000). However, a phylogenetic tree analysis has shown that *sd*-NKCC cannot be assigned to one of the two mammalian isoforms (chapter 4.1.1.3). Nevertheless, *sp*-

NKCC and *sd*-NKCC sequences revealed typical NKCC protein domains (based on PFAM database search). To further clarify the involvement of sea urchin NKCC in calcification, I addressed two hypotheses (chapter 1.4.1; Figure 55) which will be discussed in more detail in the following two chapters.

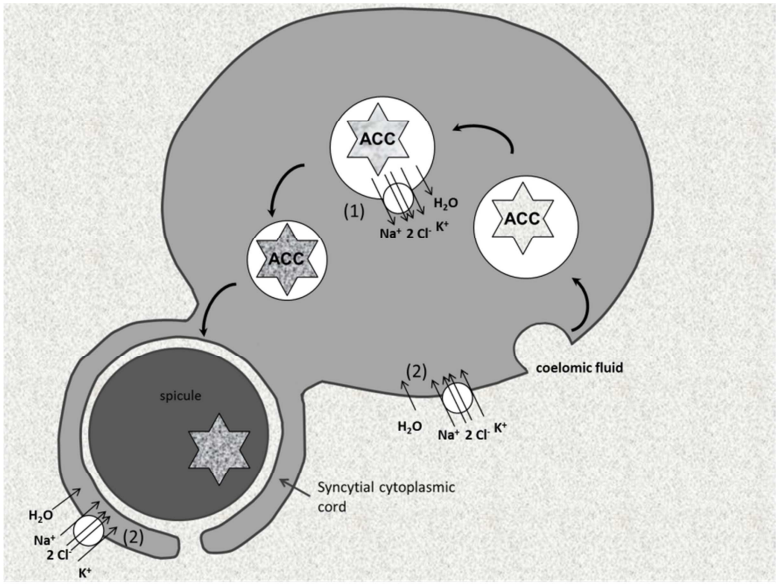

Figure 55 Two hypothesised sites of involvement of NKCC within the process of calcification. One PM-cell of the syncytium and the associated cytoplasmic cord are shown in cross-section, ACC-density (amorphous $CaCO_3$) is indicated by different structures (light = less dense, dark = dense) and the coelomic fluid is indicated by a structural background. (1) ACC-concentration hypothesis in calcification vesicles, (2) PMC-migration and cell volume regulation hypothesis. To focus only on NKCC-involvement in calcification none of any hypothesised ion channels or transporters supporting the transport of $CaCO_3$-substrates is shown.

4.1.4 NKCC involvement in the formation of calcification vesicle

Calcification vesicles carry the precursor phase of $CaCO_3$ to the site of spicule elongation (chapter 1.1.3). Emerging vesicles endocytose body fluid of the larvae (Weiner and Addadi, 2011) and their membrane may carry some of the plasma membrane proteins of the PMCs. Assuming that NKCC is located within the PMC-plasma membrane, the protein would also be incorporated into the vesicle membrane and its ion flux would be directed towards the intracellular compartment which is in favour of Na^+ and Cl^- concentration gradients (Figure 55). Water would follow the ion transport due to osmolality changes which would lead to a decrease in vesicle volume and a concentration of ACC. Alternatively, NKCC could be introduced into calcification vesicles *via* the secretory pathway of the membrane transport system (Wilson et al., 2011; Benarroch, 2012).

4.1.4.1 NKCC inhibition does not prevent the formation of Ca^{2+}-rich vesicles

I was able to show that calcein-stained vesicles were still produced when NKCC was inhibited (Figure 34), but calcein incorporation into the spicule was severely reduced (Figure 33, Table 14). Interestingly, the fluorescence of azosemide-derived vesicles (Table 14) increased by a factor of 1.7

compared to control-derived vesicles. Thus ACC precipitation may still occur within vesicles but spicule elongation is inhibited and the vesicular concentration of ACC increases.

My results confirm previous results of Mitsunaga et al. (1986c) although they have been interpreted in a different way. They measured ^{14}C incorporation in cells and spicules of isolated primary mesenchyme cells in the presence of 0.1 mM ethacrynic acid and 1 mM furosemide and showed that the ^{14}C-radioactivity in cells was increased in the presence of loop diuretics by a factor of 4-5. In contrast, the inhibition of L-type Ca^{2+} channels resulted in low ^{14}C values within the PMC and spicule fraction but high ^{14}C values in the medium. This result was interpreted in the way that the CO_2 release from the cells was affected in the presence of loop diuretics. A reinterpretation of these data and a combination with my data allows the following conclusion: in the presence of loop diuretics ACC can still be formed but cannot be exocytosed; inhibition of L-type Ca^{2+} channels prevent ACC formation and spicule elongation.

In addition, I could show that the size of vesicles is not different among the treatments which led to a rejection of the developed hypothesis about an ACC-concentration prior to exocytosis.

4.1.5 NKCC involvement in volume regulation and cellular migration of PMCs

The involvement in PMC-migration and/or volume regulation could be another possible action of *sd*-NKCC. For this, the protein would be located in the plasma membrane of PMCs (Figure 55) and, as known for migrating cells (Haas and Sontheimer, 2010; Garzon-Muvdi et al., 2012; Cuddapah and Sontheimer, 2011), ions would be transported into the cell and, passively, water would follow.

The cotransport could also be located within the cytoplasmic cords which are the platform for ACC- and organic matrix carrying vesicles. In the development of these cords, migration and volume regulation mechanisms could be needed. For example, NKCC1 is known to be essential for the process of volume increase prior to bone formation in chondrocytes, cells needed for cartilage matrix formation during bone formation in *e.g.* rats (Bush et al., 2010). Without this process, bone formation is stopped. A similar mechanism might be relevant for sea urchin larval calcification.

4.1.5.1 NKCC inhibition inhibits the development of the cytoplasmic cord

To investigate the appearance of the filopodia network and cytoplasmic cord, Dr. M. Gutowska and I stained larvae (24 h azosemide and control incubation of prism stage) with the membrane dye FM®1-43. Interestingly, we could show that the filopodial networks seem not to be affected by the presence of azosemide (see chapter 4.1.5.2) but the cytoplasmic cords were not covering the spicules of azosemide treated larvae (Figure 35).

The cytoplasmic cord has to cover all growing areas of spicules because ACC-rich vesicles are transported within this cord towards the elongation area at the tips no matter where the respective PMC is located within the syncytium (Wilt et al., 2008). Furthermore, the cytoplasmic cord is not only needed to supply the tips with new ACC-material, it is also needed to supply the growing spicule with

organic matrix material. This material is also transported *via* vesicles (Wilt et al., 2008; Ingersoll et al., 2003). The loss of cytoplasmic cord around the spicules in the presence of azosemide supports the hypothesis that NKCC-transport mechanisms are an essential mechanism for spicule calcification. The specific mechanism would be the cotransporter role in volume regulation and/or cellular migration. In both cases, the ion flux is directed towards the cytoplasm (Figure 10). My results further show that the NKCC-involvement is not only limited to the expansion of the cytoplasmic cord but is also involved in its maintenance. Otherwise one would expect cytoplasmic cord along the total length of already built spicules (Figure 35).

The loss of cytoplasmic cord coverage in the presence of azosemide is a new and important finding for the field of calcification and it further explains the calcein fluorescence increase by a factor of 1.7 in calcification vesicles of azosemide treated larvae. By the loss of the vesicle-transport-platform, the exocytosis of ACC-rich vesicles cannot occur at the site of spicule elongation. Moreover, organic matrix containing vesicles cannot be transported towards the spicule.

The favoured function of NKCC, the support of a calcification platform, is also known for another biomineralisation related model, the rat chondrocytes (Bush et al., 2010). There, NKCC is known to be essential for the volume increase of the chondrocytes.

Interestingly, loop diuretics did not show any effect on gastrulation (Figure 25, Figure 26). In short, gastrulation takes place during the gastrula stage. After ingression of the mesodermal cells the endoderm forms the archenteron by invagination. The first invagination (GaJ 1/3) comprises several mechanisms like the formation of bottle cells, apical secretion and swelling, as well as constriction (Wessel and Wikramanayake, 1999). The second invagination (GaJ 2/3) is independent of secondary mesenchyme cells which are needed for the final 1/3 of elongation as they connect the archenteron with the ectoderm and stretch the archenteron *via* contractions (Hardin, 1988; Wessel and Wikramanayake, 1999).

The fact that loop diuretics do no interact with gastrulation strengthens the specific effectiveness of loop diuretics and the fact that they do not inhibit an essential mechanism of development. However, this finding is interesting related to the assumption that NKCC is involved in volume regulation or cellular migration of the cytoplasmic cord. If this transporter is also involved in the elongation of the archenteron (cell swelling and final 1/3 elongation) some effect of loop diuretics should have been recognised. As this is not the case, it could be either that other volume and migration relevant transporters like Na^+H^+ exchangers (NHE/ SLC9-family; Hoffmann et al., 2007, 2009), AE's or Na^+ and Cl^- channels (Lang et al., 1998) are upregulated to achieve the needed ion fluxes or that NKCC is not expressed in archenteron cells as it is known for a few other cell types (Hoffmann et al., 2009) where volume regulation is mediated by NHE's and AE's. The results on DIDS-related inhibition support this. DIDS is an inhibitor of all three known AE's (Romero et al., 2004) and 5 µM DIDS did significantly reduce GaJ% but did not affect the length of the gastrula (Table 11).

4.1.5.2 PMC-ectoderm connection may be disturbed by NKCC

The thin filopodia were not affected in the stages stained with FM®1-43 (96 h old after 24 h incubation). However, the results of 92 h and 72.5 h incubation in azosemide point towards an involvement of NKCC in filopodia maintenance which could not be seen by the staining method. PMC-ectoderm connection *via* thin filopodia is needed for the localisation of PMCs within the larvae (Harkey and Whiteley, 1980; Armstrong and McClay, 1994; Miller et al., 1995; Kiyomoto et al., 2007).

Pluteus larvae incubated for 92 h and 72.5 h were characterised by deformed spicules (Figure 30) in contrast to pluteus larvae incubated for 48 h. This can be explained by the fact that the stage incubated for 48 h (prism) already built parts of the growing spicule. In contrast, the stage incubated for 72.5 h (gastrula) had only just started calcification, and the blastula stage incubated for 92 h did not start calcification at all. Thus, the PMCs of the prism stage could develop under normal conditions for 24 h and thus the filopodial network could develop normally in the beginning. The other two incubations lack this normal development for the first 24 h and may have experienced a more severe impact on filopodial development and NKCC might also impact these filopodia. By doing this, the base for calcification is disturbed which would explain the deformation of spicules in 72.5 h and 92 h incubations. A disturbance in cell proliferation, like in bronchial smooth muscle cells (Iwamoto et al., 2004), could be an explanation for the reduced development of filopodial network, but this is only speculative at this point.

4.1.6 Localisation of NKCC within primary mesenchyme cells

The functional studies already localised the cotransporter to be associated with the PMCs and based on them I would assume the location to be rather within the plasma membrane of PMCs and cytoplasmic cord.

The already discussed FM®1-43 staining showed that the cytoplasmic cords did not surround the spicules when sea urchin larvae were treated with azosemide, indicating the functional importance and expression of the cotransporter within the plasma membrane.

Staining of larvae with a monoclonal anti-human NKCC1 antibody (T4, DSHB), which had a 71% identical (e-value 10^{-75}; blastP Altschul et al., 1997) antigen region compared to the *sp*-NKCC sequence (Figure 39) stained the ectoderm, digestive systems and PMCs of whole larvae in immunofluorescence (Figure 41). The staining of ectoderm and digestive system is not surprising as at least NKCC1 is expected to be widely expressed (Haas and Sontheimer, 2010; Garzon-Muvdi et al., 2012; Cuddapah and Sontheimer, 2011; Payne and Forbush III, 1995; Hoffmann et al., 2007) and may be needed by these cells for intracellular volume regulation caused by changes in salinity. In freshly fixed larvae the cytoplasmic cords were also dominantly stained and PMC plasma membrane appeared to be stained (Figure 56). This localisation perfectly matches the assumed function of NKCC: maintaining of the calcification platform *via* volume regulation.

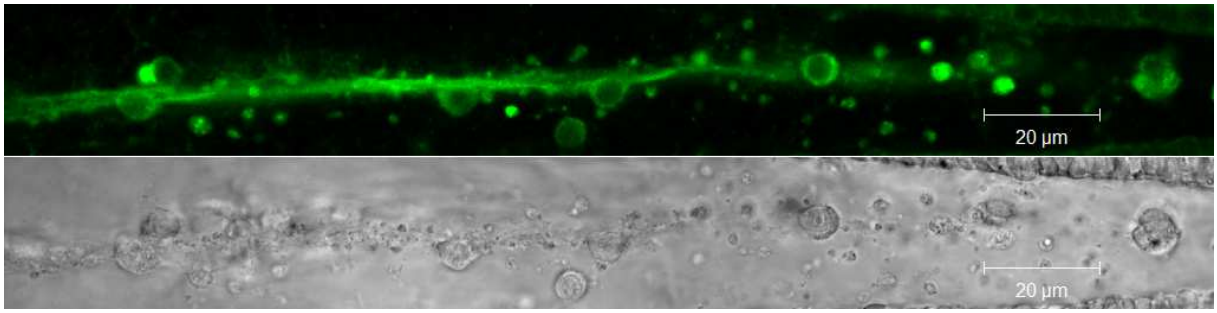

Figure 56 Exemplary staining (monoclonal antibody, T4) of PMC plasma membrane and cytoplasmic cord of fed pluteus larvae (day 8).

4.1.7 The current cell model cannot be confirmed by a pharmacological assay

As I already discussed, all non-loop diuretics revealed strong toxic side effects in a concentration dependent way on gastrulation and pluteus development. This limits the interpretation of any effect on calcification and shows that the tested non-loop diuretics cannot be used in whole larvae assays. This conclusion is further confirmed by the differences among the two drug groups on the growth of the primary body rod: non-loop diuretic drugs only partially inhibited this process (Figure 32) but strong effects on development were shown.

Presumably the non-loop diuretics are not specific enough to inhibit their target proteins in *S. droebachiensis* larvae. Another possibility is that the drugs did not reach the PMCs based on the size selectivity of the ectoderm. In sea urchin larvae this has been proposed by Mitsunaga et al. (1986a) for acetazolamide and also in ants and moths it has been shown that V-ATPase inhibitors could not easily access the target site (summarised in Dröse and Altendorf, 1997). However, Stumpp et al. (2012a) showed that FITC-dextrans < 40 kDa could pass the ectoderm after 60 min exposure. As all used inhibitors are < 40 kDa, they could pass the ectoderm and reach the PMCs if no charge and lipophobic characters blocked the diffusion.

Combining these results, I come to the conclusion that I cannot confirm the current cell model or develop a new cell model for calcification. Although almost no current functional studies on ion transporters and pumps exist for sea urchin larvae, current work on protein expression in sea urchin larvae and PMCs are summarised here in the context of the only PMC model. L-type Ca^{2+} channels have been shown in inhibitory studies (Fujino et al., 1985; Yasumasu et al., 1985; Dale et al., 1997) but only N-type Ca^{2+} channels have been shown to be expressed in PMCs (Zhu et al., 2001). Based on the DIDS toxication no conclusion can be drawn about the Ca^{2+}channels coupled to an anion transporter (Fujino et al., 1985; Yasumasu et al., 1985). The existence of an H^+K^+ ATPase and carbonic anhydrase is established (Chow and Benson, 1979; Carson et al., 1985; Mitsunaga et al., 1986a, 1987a, 1987b, 1989; Todgham and Hofmann, 2009) and a Ca^{2+} ATPase or Na^+ coupled transporter within the calcification vesicle is needed. This is based on a presumably higher intravesicular Ca^{2+} concentration and activity compared to the cytoplasm (McConnaughey and Whelan, 1997). Ca^{2+} ATPases are expressed in larvae (Jayantha Gunaratne and Vacquier, 2007;

Todgham and Hofmann, 2009). To complete this, it has been shown that Ca^{2+}channels, $Na^{+}Ca^{2+}$ exchange protein, $Na^{+}H^{+}$ exchange, $Na^{+}K^{+}Ca^{2+}$ exchanger and $Na^{+}HCO_3^{-}$- transporter are present in sea urchin larvae (Zhu et al., 2001; Todgham and Hofmann, 2009). Furthermore, it has recently been shown that PMCs are able to regulate pH_i with a Na^{+} and HCO_3^{-} dependent mechanism (Stumpp et al., 2012a).

4.1.8 Assignability of NKCC-concept to other calcifying marine organisms

I have come to the conclusion that NKCC is involved in the development of a calcification related platform as it is also known for rat chondrocytes (Bush et al., 2010) but was not known for marine organisms up to now. Although the calcification model of sea urchins is rather unique among calcifying marine organisms, this concept could also be adopted in other calcification models. In adult sea urchins, calcification is presumably similar to larval calcification (chapter 1.1.3.2) and sclerocytes could be dependent on NKCC function. Other calcifying groups also transport relevant materials (organic matrix and ACC) within vesicles and exocytose them into an extracellular matrix (*e.g.* molluscs, radial foraminifera, presumably corals) or form mature calcified elements within vesicles (*e.g.* coccolithophorides, miliolid foraminifera) (Weiner and Addadi, 2011; Addadi et al., 2006; Cohen and McConnaughey, 2003; Bentov and Erez, 2006). In corals and molluscs the vesicles are formed and transported in epithelia (calicoblastic epithelium, epithelial cells of the mantle). The respective cells could also undergo a volume increase similar to chondrocytes.

4.2 Mechanisms for an increase in the buffer capacity of the coelomic fluid and effects of ocean acidification on skeletal elements of adult sea urchins

Strongylocentrotus droebachiensis was shown to be able to actively regulate its extracellular pH during chronic CO_2 exposure (Stumpp et al., 2012b). To understand more about the mechanisms underlying these regulatory processes was one goal of my thesis. For this, two tissues were investigated, as well as the skeleton structure. I could show that the intestine is tight for HCO_3^- and could thus contribute to acid-base regulation but no pronounced electrogenic transport was detected. The peritoneal epithelium is presumably not regulating the stroma due to its leaky character. The skeletal structures were impacted at different levels by hypercapnic conditions; the inner ossicle surface of hypercapnia-stressed animals exhibited only minor surface alterations. In contrast the spicules of those animals were characterised by rather severe dissolution.

4.2.1 Methodological discussion

4.2.1.1 Ussing chamber measurements

In both Ussing chamber approaches, I worked almost at the limit of detection due to the low resistances of both tissues. This implies a source of error in terms of the voltage measurement which were avoided by controlling the agar bridges in terms of air bubbles and by avoiding the formation of salt bridges. Both factors would disturb the electrical measurements by increasing the resistance of the electric circuit or by short-circuiting the setup.

Peritoneal epithelium

The successful dissection of the epithelium was challenging and needed a new technical development. Due to the thin character (~5 µm thick) of the epithelium, the fragility was very high and disruptions of the epithelium occurred in the starting phase of dissection development. However, a good dissection method (chapter 2.4.1.1) finally resulted in reliable electrical measurements. They revealed that this epithelium was of really low resistance (0.8 ± 0.1 Ωcm^2, $n = 39$) compared to epithelia of other marine organisms and mammals (intestine of *S. droebachiensis*: 6.2 ± 1.3 Ωcm^2 (this study); tentacle of *Anemona virids*: 23 ± 5 Ωcm^2 (Bénazet-Tambutté et al., 1996); thick ascending limp, kidney, *Mus musculus*: 10-20 Ωcm^2; colon, *M. musculus*: 40-60 Ωcm^2 (Himmerkus, *personal communication*)). The success of the described dissection method was shown by the size-dependent FITC-diffusion and the FM®1-43 staining (Figure 49, Figure 48). The measured low resistance is almost at the detection limit and reflects an almost completely leaky epithelium (Gizurarson, 1993) which leads to the assumption that the peritoneal epithelium is not regulating the stroma (*e.g.* pH, ion composition) *via* transcellular transporters.

Intestine

The dissection of this tissue was less complicated compared to the peritoneal epithelium. Cleaning of the lumen was done carefully and the peristaltic movements of the intestine were reversibly inhibited by ASW enriched with 10% $MgCl_2$. Before the properties were measured the tissue was allowed to acclimatise to the experimental conditions; thus, no influences on the results were expected.

4.2.1.2 Investigations of the adult skeleton

Fracture force measurements

These measurements were conducted on dried skeletons. The drying process might have modified the organic parts of the skeletons (organic matrix, mutable collagenous tissue). This would had an impact on the measure of the ossicle junctions rather than on the ossicle stereom.

In 5 of 62 measurements of the ossicle junctions, the gained mechanical resistance was higher compared to the respective mechanical resistance of ossicle stereom. These measurements have been excluded from the analysis and retrospecifically they have been identified to reflect measurements in which the measuring needle did not meet the ossicle junction but the stereom.

SEM

The protocol for preparation of SEM-samples is well established. Only the different bleaching times used in my thesis could have impacted the surface structure, but no visible differences were observed.

To quantify the changes of the stereom surfaces I chose four regions along the latitudinal axis to overcome the problem of overlooking an effect.

4.2.1.3 $[HCO_3^-]_{PCF}$ differences among different sea urchin studies

$[HCO_3^-]_{PCF}$ in control animals of Stumpp et al. (2012b) were higher compared to other echinoidea studies (Table 1). This indicates an active – but still unknown – uptake mechanism. However, the artificial increase of Kiel fjord water salinity has to be taken into account. The alkalinity of the experimental seawater was raised by the increase in salinity (Trübenbach, 2009) and could have influenced the carbonate chemistry of the PCF. A correlation of seawater alkalinity and $[HCO_3^-]_{PCF}$ becomes clear by comparison of two studies on *S. droebachiensis* (Spicer et al., 2011; Stumpp et al., 2012b; Figure 57). Thus, the high starting $[HCO_3^-]_{PCF}$ of the investigated sea urchins may be due to the artificial increase in salinity. However, $[HCO_3^-]_{PCF}$ of *S. droebachiensis* is higher compared to $[HCO_3^-]_{SW}$ (Table 1) which is still favouring any

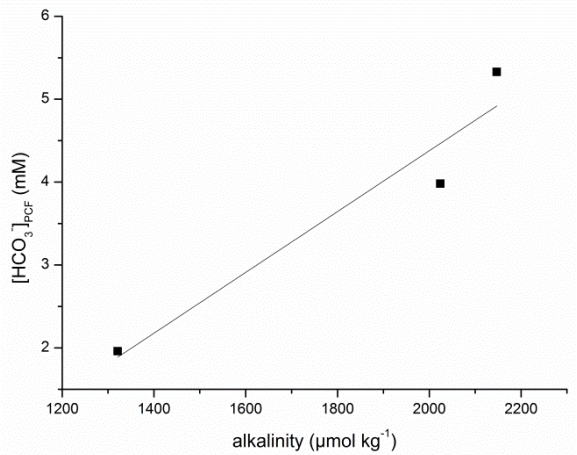

Figure 57 Relationship between seawater alkalinity and PCF HCO_3^- concentration in *S. droebachiensis*. The linear fit results in $R^2 = 0.93$. Data originate from two studies (Spicer et al., 2011; Stumpp et al., 2012b).

HCO_3^- uptake mechanism.

4.2.2 Tissue contribution to acid-base regulation of PCF

Two epithelia were investigated in terms of their electrogenic transport potential and paracellular tightness to determine their contribution to acid-base regulation. The thin peritoneal epithelium was measured the first time in an Ussing chamber and did not exhibit any electrogenic transport functions (chapter 3.2.2). Thus, it is not expected to contribute to any regulation of the stroma of coelomic fluid. However, it is not a loose and leaky united cell structure, as the paracellular pathway exhibited size selective properties (Figure 49). Free FITC (0.3 kDa) could pass the paracellular pathway and is negatively charged (pK_2 of fluorescein is 6.7; Butcher and Weissman, 1980) which favours diffusion of other negatively charged ions like HCO_3^- along the paracellular pathway.

The intestine of sea urchins is responsible for absorption and the accumulation of reserve substances (Boolootian, 1964; Tokin and Filimonova, 1977) and has been proposed to be actively transporting transcellularly due to the presence of numerous mitochondria within the absorbing cells (Tokin and Filimonova, 1977; Santos-Gouvea and Freire, 2007). Up to now, the intestine has not been investigated with the Ussing chamber technique to test the occurrence of any electrogenic transporter.
To test if an electrogenic member of the SLC4-family (*i.e.* NBCe1 and NBCe2, both are Na^+ coupled; Romero et al., 2004) is localised within the intestine epithelium, DIDS was applied on both sides in succession. Only the luminal application changed the potential but, unfortunately, the application of the vehicle alone and of DIDS caused a similar potential change. Thus, no conclusion about the presence of a SLC4-member can be drawn. Although DMSO is widely used as a solvent for drugs, it can cause some side effects. These effects are reported for cell cycle, differentiation, lipid metabolism and many other study fields (Santos et al., 2003) and also for electrical measurements of tissues (Kosik-Bogacka et al., 2002). In the latter study, DMSO has been reported to predominantly decrease the transepithelial potential of rabbit caecum and frog skin.
Although no conclusive outcome resulted from this investigation, I could show that the intestine is tight for HCO_3^- and charge selective. By being a barrier for HCO_3^- the intestine is not a sink for HCO_3^- and thus contributes to the acid-base regulation. Important for this consideration is the tightness of the outer epidermis since otherwise HCO_3^- could diffuse via this pathway (Figure 59). Experiments by Ries et al. (2009) on cidaroid and non-cidaroid sea urchins indicate this tissue to be tight since cidaroid sea urchins (no epidermis covering fully grown spines) are characterised by hypercapnic induced dissolution (Table 2).
In addition, I could demonstrate relative cation selectivity of the intestine. This is consistent with SJ of the intestine in *Macrobrachium rosenbergii* (freshwater prawn) and in the larval midgut of *Bombyx mori* (silkworm/ -moth) (Ahearn, 1980; Fiandra et al., 2006). In contrast, malpighian tubules of *Rhodnius prolixus* (kissing bug) and of *Aedes aegypti* (mosquito) are permeable for uncharged and

negatively charged molecules (Skaer et al., 1987) and anions (Yu and Beyenbach, 2001), respectively. Compared to other diffusion potential studies, the diffusion potentials of the sea urchin intestine were not symmetric. This may indicate that the revealed potential is a combination of the SJ properties and the function of an unknown transporter. This transporter could be responsible for anion transport towards the basolateral side. If this anion transport is a $Na^+HCO_3^-$ coupled transport, a Cl^- transport or any other anion transporter cannot be answered. HCO_3^- supply could be mediated by two different pathways: either by a luminal HCO_3^- uptake or by intracellular CO_2 hydration mediated by carbonic anhydrases coupled to luminal H^+ secretion as known for gastric glands of mammalian stomach (de Beus et al., 1993).

In a pilot study, the effects of temperature, DIDS and 0 mM HCO_3^- were tested on the asymmetric diffusion potential (Figure 58) but did not result in symmetric potentials. The idea was that inhibition of a DIDS sensitive HCO_3^- transporter should result in an increased basolateral potential if HCO_3^- is not generated intracellularly. The same would have been true for the reduction of HCO_3^- if this was a relevant substrate for the transporter. Also the temperature reduction should have resulted in a changed diffusion pattern. Ion transporter-activity is temperature dependent and reported Q_{10} values range between 2.5 (K-Cl cotransporter in frog erythrocytes; Agalakova et al., 1997) and 1.8-3.0 (HCO_3^- secretion in fish intestine; Grosell and Genz, 2006). The attempt to decrease the temperature to 0-1°C (Δ°C = 9-10) failed and only 4.5°C (Δ°C = 5.5) was reached. By applying reported Q_{10} values differences in V_{te} change could have been detected. However, technical reasons could be responsible for the differences in diffusion potential. The intestine consists of four layers: the intestinal epithelium is located luminally, followed by more basolateral layers of connective tissue, muscles and an outer epithelium (Boolootian, 1964). Solution changes on the luminal side are in direct contact with the investigated epithelium and SJ. In contrast, any solution change basolaterally has to cross first the other layers and could diminish the effect of the basolateral side of the intestinal epithelium.

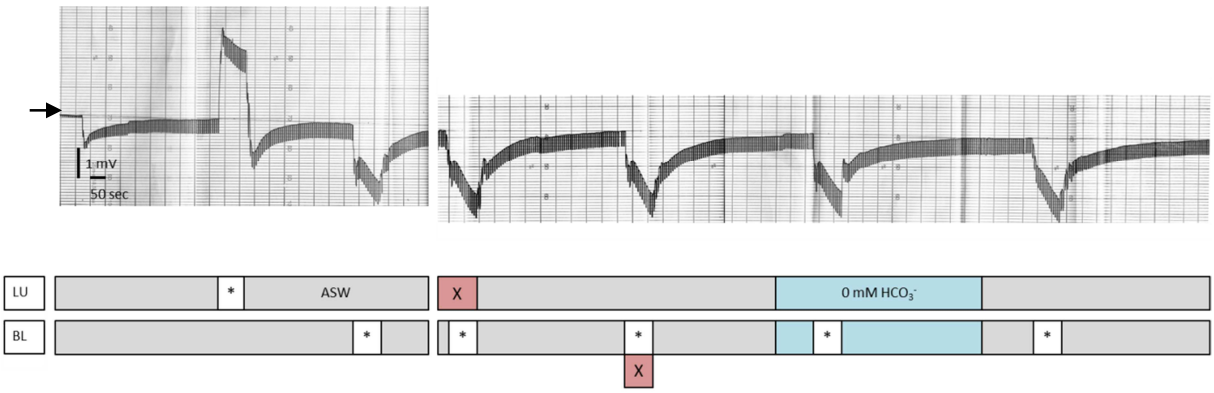

Figure 58 Investigation to overcome the asymmetric NaCl-diffusion potential. * marks the application of low NaCl-ASW, X is marking the application of 50 µM DIDS, the arrow indicates 0 mV.

However, both effects reveal cation selectivity. The reason why I addressed the charge selectivity of SJ

to the overall terms “cation” and “anion” and not to sodium vs. chloride selectivity is the following: although only [NaCl] was changed in the experiment, the diffusion of other cations and anions cannot be excluded. This is based on the fact, that their concentration (*i.e.* Mg^{2+}: 53 mM, Ca^{2+}: 10 mM, SO_4^{2-}: 28 mM) is rather high. Thus, these ions are also able to compensate the charge differences when the paracellular pathway is selective for the respective ion.

In addition to the described results, an initial lumen-negative potential was found in the Ussing chamber measurements. This potential either indicates an anion transport towards the lumen or a cation transport towards the basolateral cavity. The potential became smaller during the experiment (Figure 43) and thus, an unknown stimulus could be responsible for the initial potential. To address the stimulus, different approaches were used: basolateral stimulation with FSK/IMBX (increase in intracellular cAMP) or ATP (purinergic agonist to stimulate Ca^{2+} release) stimulation did not change the potential. Thus, it can be said that the intestine of *S. droebachiensis* does not exhibit these activation processes known for mammalian epithelial transport. Nevertheless, in one experiment, the tissue had to be realigned on the Ussing chamber insert and after placing it back into the chamber, a new lumen negative potential was generated. Thus, mechanical stimulation by fecal pellets (Trendelenburg, 1917) activates peristalsis and maybe also transport processes.
The lumen-negative potential caused by luminal glucose application indicates that the intestine possesses an electrogenic Na^+ coupled glucose transporter as it is known for the mammalian intestine (Wright, 1993).

4.2.3 Dissolution of ossicles is partially contributing to PCF-buffering and not leading to destabilisation of the skeleton

4.2.3.1 Investigation of the inner stereom surface

In the foregoing sections I showed that the stereom is not insulated from the PCF by the peritoneal epithelium. Thus, the conditions of stroma and PCF are the same and the stereom is exposed to any condition the PCF is experiencing (Figure 59). The stereom of the investigated CO_2-stressed sea urchins was exposed to $CaCO_3$-undersaturated conditions, which were characterised by PCF aragonite saturation state < 1 in the intermediate and high pCO_2 treatment for at least four days (Stumpp et al., 2012b; Figure 59). During at least this time, the stereom could have been partially dissolved as suggested from the SEM analysis (Figure 50, Table 17) and contributed partially to an increase in HCO_3^-. In the following long-term exposure PCF pH was compensated by an increase in $[HCO_3^-]_{PCF}$ (Stumpp et al., 2012b; Figure 59). The stabilisation of the acid-base conditions is also confirmed by the lack of major dissolution events. CO_2-related dissolutions have been reported for pluteus larvae (Clark et al., 2009) and for adult sea urchin spines (Figure 50, Table 17).

The amount of released CO_3^{2-}, presumably released during an acute CO_2 exposure, was calculated to be 0.21-0.84 10^{-3} M depending on the CO_2 treatment (chapter 3.3.1). This calculation is a rough estimation as the enlarged surface area of the fenestrated stereom was not considered. But the SEM analysis did not allow drawing any conclusions about the surfaces in the inner stereom areas. In some of the ossicles with altered microstructure the pore surfaces seemed to be rather smooth than granular. Comparing the estimated values with the HCO_3^- increase measured by Stumpp et al (2012b) reveals that stereom dissolution contributes only partially to the increased buffer capacity.

The CO_2-dependent surface alterations appeared as round granular structures (Figure 50). To my knowledge, such a structure had not been characterised in the context of ocean acidification before but as the percentage of appearance increased under the highest CO_2 treatment, it seems that this is due to hypercapnia. Similar structures are found in studies dealing with ACC, mainly in sea urchin larval spicules (Weiner and Addadi, 2011; Decker et al., 1987). Decker et al. (1987) further showed that those granular structures are not resulting from etching.

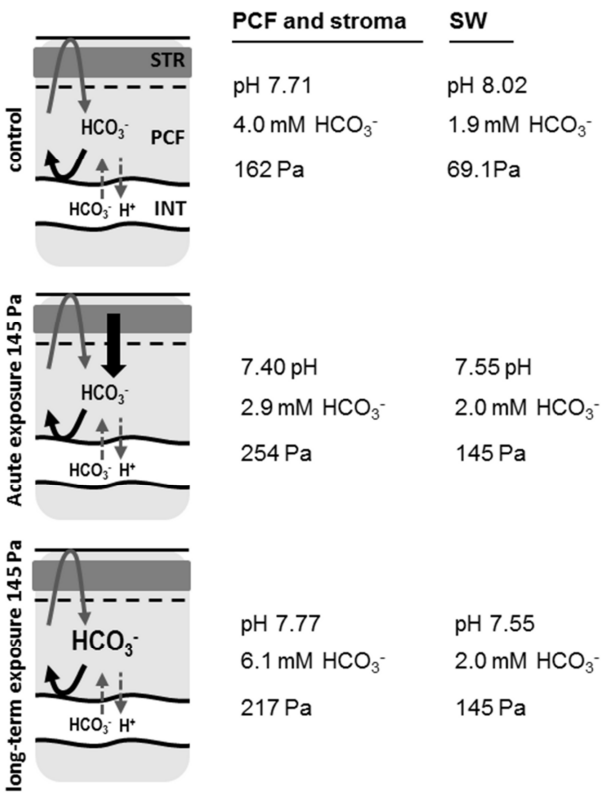

Figure 59 Model for pH homeostasis in perivisceral coelomic fluid based on data for PCF carbonate system from Stumpp et al. (2012b) and this thesis during control, acute exposure (day 4) and long-term exposure (10 days) to hypercapnic conditions (145 Pa). CO_2 in PCF increases with seawater CO_2. The drop in PCF pH is partially prevented by the free ion movement between PCF and stereom *via* a highly permeable peritoneum. This allows proton buffering and HCO_3^- release by skeletal carbonate dissolution during the acute exposure. HCO_3^- loss from PCF is prevented by the barrier function of the intestine and by a presumed barrier built by the epidermis (indicated by the grey reflecting arrow). Future studies have to investigate the active contribution of the intestine to the elevation of PCF buffer concentration as a HCO_3^- source or a proton sink (dotted arrow). The solid line indicates the epidermis, followed by the stereom (STR) and the peritoneal epithelium (dashed line); PCF = perivisceral coelomic fluid, INT = intestine.

Stereom dissolution in other studies

In other short-term (12 h to 8 days) echinoid studies on *P. miliaris*, *Brissopsis lyrifera* and *S. droebachiensis* stereom dissolution has been hypothesised, based on an increase in $[Ca^{2+}]_{PCF}$ or $[Mg^2]_{PCF}$ and $[HCO_3^-]_{PCF}$ (Miles et al., 2007; Spicer et al., 2011; Spicer and Widdicombe, 2012). These findings are consistent with my assumption that minor dissolution in *S. droebachiensis* happened during acute hypercapnia (Figure 59).

4.2.3.2 Investigation of ossicle stability

That dissolution of ossicles is not severe was also shown in the fracture force analysis. Among the CO_2 treatments, no significant difference in the applied force to break the ossicles was found.

Investigations of the shell stability in other phyla (bivalves and barnacles) revealed also no correlation between pCO_2 treatments and shell stability except of one experiment on juveniles of *Amphibalanus improvius*. In two experiments, these juveniles were incubated for 8-weeks either in batch cultures or in a flow through system and individuals of the batch culture showed a reduction of the shell stability at 217 Pa which might be due to different culture and starting conditions (Pansch et al., 2012). In another study on *Mytilus edulis* and *Arctica islandica*, Hiebenthal et al. (2012) found no correlation of shell stability to pCO_2 treatments.

In addition to the stability test of ossicles, the stability of the latitudinal ossicle junction was tested. This, and not the testing of the stability of the longitudinal junctions, was done due to dissection reasons. The measuring needle was placed on this junction and in both hypercapnic treatments the force needed for breaking was significantly smaller than in the control ossicles. Surprisingly, the force needed for the intermediately treated ossicle junctions was lower in average than that needed for ossicles of the highest CO_2 treatment. However, the finding, that junctions are less stable due to hypercapnia, was also confirmed by a qualitative characterisation during dissection of sea urchin test. Instable test felt apart at the ossicle junctions when they were touched, strong tests were difficult to break and the test which could not be assigned to one of these categories were of middle strength. In a quality evaluation, 11% of the control ossicle junctions broke easily and 63% were strong. In contrast, 50% of the high CO_2 ossicle junctions were instable and only 6% were strong. These observations are also in agreement with previously reported brittleness of sea urchin skeletal elements (Shirayama and Thornton, 2005; Miles et al., 2007; Siikavuopio et al., 2007). Which part of the ossicles and their junctions is exactly affected is not clear. The junctions are made of connective tissue and for echinoderms in general it is known that they are made of mutable collagenous tissue (MCT) which can change its viscosity within seconds (Wilkie, 2005; Barbaglio et al., 2012). But dried skeletons were used for this study, and MCT-properties could have changed during the drying process (chapter 4.2.1.2).

Also newly built trabeculae could be affected by hypercapnia and resulted in destabilised ossicle junctions. But two arguments speak against this thought: i) no differences in appearance were visible (Figure 50); ii) growth increment at the latitudinal edge was low under the highest hypercapnic condition (aboral I: 0.12 ± 0.07 µm d^{-1}; aboral II: 0.02 ± 0.02 µm d^{-1}) and changes in the new grown parts could thus contribute only little to a change in stability.

4.2.4 Shape of hypercapnia stressed ossicles is not changed but growth is reduced

4.2.4.1 Hypercapnia related effects on ossicle growth

The investigation revealed that ossicle growth was reduced but still positive under hypercapnic conditions and that newly grown stereom parts could not be distinguished from older parts (Figure 50).

Thus, it seems that net-calcification is not altered which is favoured by the regulation of PCF acid-base status during the long-term incubation. Also in a recent publication, increased net-calcification at hypercapnic conditions (4 day exposure to 155 Pa) was hypothesised based on an increase of [Ca^{2+}] and [Mg^{2+}] within the test (Calosi et al., 2013).

The investigated ossicles originate from sea urchins whose metabolic allocation had been investigated in advance by Stumpp et al. (2012b). They could show that the energy budget in animals of the highest treatment was shifted but metabolic rates were not changed significantly. This is in accordance with my growth data as they imply that less energy was provided for somatic growth. Furthermore, the data of reduced growth were also in line with other studies on echinoidea (Shirayama and Thornton, 2005; Ries et al., 2009; Table 2).

If ossicle growth of *S. droebachiensis* recovers to control rates when sea urchins are incubated longer than six weeks to hypercapnic conditions, remains unclear. Nevertheless, 102-145 Pa is already seasonally experienced by individuals of *S. droebachiensis* from the Kattegat today (Thomsen et al., 2010). Thus, it is possible that an adaption can occur. Dupont et al. (2012), for example, showed adaption in terms of fecundity: they incubated individuals of *S. droebachiensis* at 122 Pa for 16 months and could show that their fecundity was not different from control individuals. In animals incubated for only four months a significant lower fecundity was shown.

4.2.4.2 General observations made on ossicle growth

By measuring the growth in different areas along the oral-aboral axis, I could detect a growth gradient which was independent of the CO_2 treatment. A similar gradient was previously reported by Kobayashi and Taki (1969) for *Strongylocentrotus intermedius*.

The daily control ossicle increment of the investigated sea urchins is approx. 0.06 mm d^{-1} (region aboral II). This calculation is based on the daily growth of ossicles (1.4 µm d^{-1}) and the assumption that all 40 growing areas (2 per ossicle) grow with the same rate. The estimated daily growth is in accordance with other studies on *S. droebachiensis*, which revealed test growth rates ranging from 0.01-0.07 mm d^{-1} in sea urchins with a diam. of 13-57 mm under variable food availability (Swan, 1961; Meidel and Scheibling, 1999; Scheibling and Anthony, 2001).

4.2.5 Spine stereom dissolution decreases effectiveness of spines as a defence mechanism

The analysis of the outer spine stereom structure and the stability revealed that both parameters are affected by hypercapnia.

Significant differences in length of dissected spines indicated an effect of hypercapnia on spine stability which could be confirmed by quantification (Figure 51). In this context, it is likely that the spines broke already during the experiment. The consequence of this may be that the epidermis, which

usually protects the skeleton against dissolution (Ries et al., 2009; Doney et al., 2009), was disrupted at the breaking edge and had to be regenerated prior to the regeneration of spicules. Immediately after spine rupture epidermal cells accumulate at the breaking edge but are missing paracellular junctions (Heatfield and Travis, 1975). Thus, not only the non-corrosive stroma (284 Pa: pH 7.48, 7.62 mM HCO_3^-, Ω_{Ar} = 1.46, filled stomach) was in contact with the spine stereom but also the corrosive hypercapnic seawater (284 Pa: pH 7.19, 2.14 mM HCO_3^-, Ω_{Ar} = 0.32).

In sea urchins, spines serve as defence mechanisms against predators (Moitoza and Phillips, 1979; Tegner and Levin, 1983). By loss of stability, the spines lose part of their function resulting in more predation which in turn would impact the sea urchin population. This impact is further increased by the longevity of sea urchins (at least 25-50 years; Scheibling and Hatcher, 2007; Ebert and Southon, 2003) and might reduce the fitness of older sea urchins.

5 Conclusions and Outlook

To judge the effects and consequences of ocean acidification it is important to understand the concept of calcification in more detail.

For sea urchin larval calcification, I could show that the $Na^+K^+2Cl^-$ cotransporter is needed to support the calcification platform (*i.e.* cytoplasmic cord) for spicule formation. How this transporter is affected by increased pCO_2 remains unclear; however, at a certain acidic pH, individual for different proteins, membrane proteins function is inhibited.

Adult *S. droebachiensis* have been shown to react to hypercapnic conditions *via* an increase in $[HCO_3^-]_{PCF}$ which stabilises the acid-base conditions of PCF (Stumpp et al., 2012b). This phenomenon is mirrored by my data as the inner ossicle surface, which is in contact with PCF, is characterised by minor dissolution events. In contrast to this, the spines are characterised by a more severe dissolution which is presumably caused by their direct contact to corrosive seawater when the epidermis is ruptured.

5.1 Cellular mechanisms involved in larval calcification

The presented work contributes to the understanding of cellular processes involved in sea urchin larval calcification by showing the involvement of the $Na^+K^+2Cl^-$ cotransporter (NKCC). By functional studies, I could show that the cotransporter is located within the primary mesenchyme cells (PMCs), also the immunohisotchemistry data confirm this hypothesis. Other visualising methods like *in-situ* hybridisation and Western blotting failed to localise NKCC-expressing regions in larvae. Quantitative RT-PCR would be useful to show expression levels of NKCC in relation to housekeeping genes in PMC tissue.

Isolation of PMCs is known to work in *e.g. Hemicentrotus pulcherrimus*, *Pseudocentrotus depressus*, *Anthocidaris crassispina* and *S. purpuratus* (Okazaki, 1975; Wilt et al., 2008). However, in *S. droebachiensis* my attempts to isolate PMCs for primary cell culture resulted in cells with poorly developed spicules which thus could not be used for any further experiments. An alternative to isolate PMCs for molecular techniques could be a modification of the bag isolation technique.

Isolated PMC cultures could further be used to work on the calcification cell model. The used inhibitors may not cause toxic side effects on isolated PMCs as they reach the target cell immediately. Such an attempt is promising as nifedipine was shown to have no effects on the protein synthesis in PMC cultures of *S. purpuratus* (Hwang and Lennarz, 1993). And verapamil was shown to inhibit 50% of spicule formation at 5 µM in PMC cultures (Hwang and Lennarz, 1993) but in whole larvae concentrations of ~16 µM and ~50 µM were needed (Fujino et al., 1985; Yasumasu et al., 1985).

The effect of azosemide on the cytoplasmic cord and filopodia could be adressed further by using isolated PMCs. Adopting the ratiometric microfluorimetry with the pH sensitive dye BCECF

(visualising of pH_i; *e.g.* Stumpp et al., 2012a for sea urchin larvae) would help to investigate NKCC regulation in PMCs according to the described protocoll by Warth et al. (1998). In short, giving a NH_3/NH_4^+ pulse leads to a pH_i drop based on the uptake of NH_4^+ *via* the cotransporter after an intial increase in pH_i (NH_3 uptake). Activating NKCC *a priori* by *e.g.* cAMP increase would change the NH_4^+ uptake rate (Warth et al., 1998). Studying the NKCC-activation in PMCs and possible rearrangements within the cells would also be another goal. In sea urchin coelomocytes NKCC is homogenously present in the plasma membrane after acitvation and could be inhibited by phalloidin (inhibition of cytoskeleton rearrangement) (D'Andrea-Winslow et al., 2001).

Another interesing question is, of course, the assignability of the NKCC-concept to adult sea urchins. A simple first approach would be the incubation of juvenile or young sea urchins in azosemide-rich seawater and the measurement of ossicle growth by calcein staining pior to the experiment. Odontoblast of the plumula region of jaws could be a good candidate for cell culture to further study the involvement of NKCC. This would allow more budget-priced research as the water and drug volume could be reduced.

5.2 Mechanisms for an increase in the buffer capacity of the coelomic fluid and effects of ocean acidification on skeletal elements of adult sea urchins

With the work on this topic I contributed to the question which mechanisms underlie the acid-base regulation in CO_2-stressed adult *S. droebachiensis* and could show that growth of ossicles is still maintained under hypercapnic conditions.

In my thesis I could successfully establish dissections of the peritoneal epithelium and the intestine for a following characterisation *via* the Ussing chamber technique. By using this technique, I could confirm my hypotheses on these tissues: the intestine is tight for HCO_3^- and is thus contributing to acid-base regulation and the peritoneal epithelium does not form an effective barrier. This means that the stereom is in contact to any PCF condition and the corrosive PCF conditions during acute CO_2 exposure (first 4 days). This resulted in minor dissolution patterns of inner ossicle surfaces. However, it remains unclear if and how the intestine transports HCO_3^- towards the PCF.

Further investigations of the intestine would help to understand transport mechanisms. One approach would be the repetition of Ussing chamber experiments with sea urchins that have been maintained at high pCO_2 (*e.g.* ~102 and ~280 Pa) values for six weeks. If the regulatory processes are based on electrogenic transporters, negative V_{te} should be increased, based on increased regulatory transport. Another approach would be testing for potential candidates by RT-PCR, *e.g.* members of the SLC4-family (HCO_3^- transport proteins). By adopting the ratiometric microfluorimetry with BCECF (previous chapter), a possible transport pathway of HCO_3^- could be investigated: similar as in mammalian stomach HCO_3^- might be formed intracellularly by CO_2 hydration (de Beus et al., 1993). Protons are secreted luminally and HCO_3^- is transported towards the basolateral compartment *via* a Cl^-

HCO_3^- exchanger. Incubating the cells in Cl^- free solution then results in an increase of pH_i (Paradiso et al., 1986).

Also, the seawater could serve as a HCO_3^- source for acid-base regulation as it was recently shown for fish (Esbaugh et al., 2012): 24 h incubation at 190 Pa in nominally 0 mM HCO_3^- seawater (*i.e.* 182 µM) resulted in unchanged plasma [HCO_3^-]. If an adopted protocol resulted in similar findings for sea urchins, tissues like the epidermis, peristomial membrane (tissue around the mouth) and the water vascular system should be investigated.

In contrast to the inner ossicle surface, the spines were characterised by severe dissolution and loss in stability when the respective sea urchins were exposed to hypercapnic conditions. This loss in stability involves a loss in predator defence. Still, the question remains why the spines get into contact with the corrosive seawater as *S. droebachiensis* in a non-cidaroid sea urchin. To investigate the histology of the epidermis of normally grown and regenerating spines under control and CO_2 exposure would be a good starting point to understand more about the epidermis function.

References

Adams, D. K., Sewell, M. A., Angerer, R. C. and Angerer, L. M. (2011). Rapid adaptation to food availability by a dopamine-mediated morphogenetic response. *Nature Communications* **2**, 592.

Addadi, L., Joester, D., Nudelman, F. and Weiner, S. (2006). Mollusk Shell Formation: A Source of New Concepts for Understanding Biomineralization Processes. *Chemistry – A European Journal* **12**, 980-987.

Addadi, L., Raz, S. and Weiner, S. (2003). Taking Advantage of Disorder: Amorphous Calcium Carbonate and Its Roles in Biomineralization. *Advanced Materials* **15**, 959-970.

Addison, J. A. and Pogson, G. H. (2009). Multiple gene genealogies reveal asymmetrical hybridization and introgression among strongylocentrotid sea urchins. *Molecular Ecology* **18**, 1239-1251.

Agalakova, N. I., Lapin, A. V. and Gusev, G. P. (1997). Temperature Effects on Ion Transport Across the Erythrocyte Membrane of the Frog *Rana temporaria*. *Comparative Biochemistry and Physiology Part A: Physiology* **117**, 411-418.

Ahearn, G. A. (1980). Intestinal electrophysiology and transmural ion transport in freshwater prawns. *American Journal of Physiology Cell Physiology* **239**, C1-C10.

Aizenberg, J., Weiner, S. and Addadi, L. (2003). Coexistence of Amorphous and Crystalline Calcium Carbonate in Skeletal Tissues. *Connective Tissue Research* **44**, 20-25.

Akberali, H. B. (1980). ^{45}Calcium uptake and dissolution in the shell of *Scrobicularia plana* (da Costa). *Journal of Experimental Marine Biology and Ecology* **43**, 1-9.

Alper, S. L. (2006). Molecular physiology of SLC4 anion exchangers. *Experimental Physiology* **91**, 153-161.

Altschul, S., Madden, T., Schaffer, A., Zhang, J., Zhang, Z., Miller, W. and Lipman, D. (1997). Gapped BLAST and PSI-BLAST: a new generation of protein database search programs. *Nucleic Acids Research* **25**, 3389 - 3402.

Altschul, S. F., Wootton, J. C., Gertz, E. M., Agarwala, R., Morgulis, A., Schäffer, A. A. and Yu, Y.-K. (2005). Protein database searches using compositionally adjusted substitution matrices. *FEBS Journal* **272**, 5101-5109.

Ameye, L., De Becker, G., Killian, C., Wilt, F., Kemps, R., Kuypers, S. and Dubois, P. (2001). Proteins and Saccharides of the Sea Urchin Organic Matrix of Mineralization: Characterization and Localization in the Spine Skeleton. *Journal of Structural Biology* **134**, 56-66.

Andersson, A., Mackenzie, F. and Bates, N. (2008). Life on the margin: implications of ocean acidification on Mg-calcite, high latitude and cold-water marine calcifiers. *Marine Ecology Progress Series* **373**, 265-273.

Armstrong, N. and McClay, D. R. (1994). Skeletal Pattern Is Specified Autonomously by the Primary Mesenchyme Cells in Sea Urchin Embryos. *Developmental Biology* **162**, 329-338.

Banerjee, S., Sousa, A. and Bhat, M. (2006). Organization and function of septate junctions. *Cell Biochemistry and Biophysics* **46**, 65-77.

Barbaglio, A., Tricarico, S., Ribeiro, A., Ribeiro, C., Sugni, M., Di Benedetto, C., Wilkie, I., Barbosa, M., Bonasoro, F. and Candia Carnevali, M. D. (2012). The mechanically adaptive connective tissue of echinoderms: Its potential for bio-innovation in applied technology and ecology. *Marine Environmental Research*.

Barnes, R. D. (1980). Invertebrate Zoology. Philadelphia: Saunders College.

Beisvag, V., Falck, G., Loennechen, J. P., Qvigstad, G., Jynge, P., Skomedal, T., Osnes, J. B., Sandvik, A. K. and Ellingsen, Ø. (2003). Identification and regulation of the gastric H^+/K^+-ATPase in the rat heart. *Acta Physiologica Scandinavica* **179**, 251-262.

Beldowski, J., Löffler, A., Schneider, B. and Joensuu, L. (2010). Distribution and biogeochemical control of total CO_2 and total alkalinity in the Baltic Sea. *Journal of Marine Systems* **81**, 252-259.

Benarroch, E. E. (2012). Membrane trafficking and transport: Overview and neurologic implications. *Neurology* **79**, 1288-1295.

Bénazet-Tambutté, S., Allemand, D. and Jaubert, J. (1996). Permeability of the oral epithelial layers in cnidarians. *Marine Biology* **126**, 43-53.

Beniash, E., Addadi, L. and Weiner, S. (1999). Cellular Control Over Spicule Formation in Sea Urchin Embryos: A Structural Approach. *Journal of Structural Biology* **125**, 50-62.

Beniash, E., Aizenberg, J., Addadi, L. and Weiner, S. (1997). Amorphous calcium carbonate transforms into calcite during sea urchin larval spicule growth. *Proceedings of the Royal Society of London. Series B: Biological Sciences* **264**, 461-465.

Benson, S., Smith, L., Wilt, F. and Shaw, R. (1990). The synthesis and secretion of collagen by cultured sea urchin micromeres. *Experimental Cell Research* **188**, 141-146.

Benson, S. C., Benson, N. C. and Wilt, F. (1986). The organic matrix of the skeletal spicule of sea urchin embryos. *The Journal of Cell Biology* **102**, 1878-1886.

Bentov, S. and Erez, J. (2006). Impact of biomineralization processes on the Mg content of foraminiferal shells: A biological perspective. *Geochemistry, Geophysics, Geosystems* **7**.

Beyenbach, K. W., Skaer, H. and Dow, J. A. T. (2010). The Developmental, Molecular, and Transport Biology of Malpighian Tubules. *Annual Review of Entomology* **55**, 351-374.

Beyer, K. H., Baer, J. E., Michaelson, J. K. and Russo, H. F. (1965). Renotropic characteristics of ethacrynic acid: a phenoxyacetic salutetic-diuretic agent *Journal of Pharmacology and Experimental Therapeutics* **147**, 1-22.

Bishop, C. D. and Watts, S. A. (1992). Biochemical and morphometric study of growth in the stomach and intestine of the echinoid *Lytechinus variegatus* (Echinodermata). *Marine Biology* **114**, 459-467.

Boolootian, R. (1964). A histological study of the food canal of *Strongylocentrotus franciscanus*. *Helgoländer wissenschaftliche Meeresuntersuchungen* **11**, 118-127.

Bornancin, M., de Renzis, G. and Naon, R. (1980). $Cl^-HCO_3^-$ ATPase in gills of the rainbow trout: evidence for its microsomal localization. *American Journal of Physiology - Regulatory, Integrative and Comparative Physiology* **238**, R251-R259.

Boron, W. F. (2004). Regulation of intracellular pH. *Advances in Physiology Education* **28**, 160-179.

Burg, M. and Green, N. (1973a). Effect of ethacrynic acid on the thick ascending limb of Henle's loop. *Kidney International* **4**, 301-308.

Burg, M. and Green, N. (1973b). Function of the thick ascending limb of Henle's loop. *American Journal of Physiology* **224**, 659-668.

Burg, M., Stoner, L., Cardinal, J. and Green, N. (1973). Furosemide effect on isolated perfused tubules. *American Journal of Physiology -- Legacy Content* **225**, 119-124.

Bush, P. G., Pritchard, M., Loqman, M. Y., Damron, T. A. and Hall, A. C. (2010). A key role for membrane transporter NKCC1 in mediating chondrocyte volume increase in the mammalian growth plate. *Journal of Bone and Mineral Research* **25**, 1594-1603.

Butcher, E. C. and Weissman, I. L. (1980). Direct fluorescent labeling of cells with fluorescein or rhodamine isothiocyanate. I. Technical aspects. *Journal of Immunological Methods* **37**, 97-108.

Byrne, M. (1994). Ophiuroidea. In *Microscopic Anatomy of Invertebrates - Echinodermata*, vol. 14 (ed. F. W. Harrison and F.-S. Chia), pp. 247-343: Wiley-Liss, Inc.

Cabantchik, Z. I. and Greger, R. (1992). Chemical probes for anion transporters of mammalian cell membranes. *American Journal of Physiology - Cell Physiology* **262**, C803-C827.

Cai, W.-J., Hu, X., Huang, W.-J., Murrell, M. C., Lehrter, J. C., Lohrenz, S. E., Chou, W.-C., Zhai, W., Hollibaugh, J. T., Wang, Y. et al. (2011). Acidification of subsurface coastal waters enhanced by eutrophication. *Nature Geoscience* **4**, 766-770.

Calosi, P., Rastrick, S. P. S., Graziano, M., Thomas, S. C., Baggini, C., Carter, H. A., Hall-Spencer, J. M., Milazzo, M. and Spicer, J. I. (2013). Distribution of sea urchins living near shallow water CO_2 vents is dependent upon species acid–base and ion-regulatory abilities. *Marine Pollution Bulletin*.

Carson, D. D., Farachach, M. C., Earles, D. S., Decker, G. L. and Lennarz, W. J. (1985). A monoclonal antibody inhibits calcium accumulation and skeleton formation in cultured embryonic cells of the sea urchin. *Cell* **41**, 639-648.

Catarino, A., Bauwens, M. and Dubois, P. (2012). Acid–base balance and metabolic response of the sea urchin *Paracentrotus lividus* to different seawater pH and temperatures. *Environmental Science and Pollution Research* **19**, 2344-2353.

Chen, C.-P. and Lawrence, J. M. (1987). The role of carbonic anhydrase in facilitating the transport of CO_2 in the tooth of *Lytechinus variegatus* (Echinodermata: Echinoidea). *Comparative Biochemistry and Physiology Part A: Physiology* **87**, 327-331.

Chow, G. and Benson, S. C. (1979). Carbonic anhydrase activity in developing sea urchin embryos. *Experimental Cell Research* **124**, 451-453.

Clark, D., Lamare, M. and Barker, M. (2009). Response of sea urchin pluteus larvae (Echinodermata: Echinoidea) to reduced seawater pH: a comparison among a tropical, temperate, and a polar species. *Marine Biology* **156**, 1125-1137.

Cohen, A. L. and McConnaughey, T. A. (2003). Geochemical Perspectives on Coral Mineralization. *Reviews in Mineralogy and Geochemistry* **54**, 151-187.

Conley, D. J., Carstensen, J., Ærtebjerg, G., Christensen, P. B., Dalsgaard, T., Hansen, J. L. S. and Josefson, A. B. (2007). Long-term Changes and Impacts of Hypoxia in Danish Coastal Waters. *Ecological Applications* **17**, S165-S184.

Cuddapah, V. A. and Sontheimer, H. (2011). Ion channels and tranporters in cancer. 2. Ion channels and the control of cancer cell migration. *American Journal of Physiology - Cell Physiology* **301**, C541-C549.

D'Andrea-Winslow, L., Strohmeier, G. R., Rossi, B. and Hofman, P. (2001). Identification of a sea urchin $Na^+/K^+/2Cl^-$ cotransporter (NKCC): microfilament-dependent surface expression is mediated by hypotonic shock and cyclic AMP. *Journal of Experimental Biology* **204**, 147-156.

Dale, B., Yazaki, I. and Tosti, E. (1997). Polarized distribution of L-type calcium channels in early sea urchin embryos. *American Journal of Physiology - Cell Physiology* **273**, C822-C825.

de Beus, A. M., Fabry, T. L. and Lacker, H. M. (1993). A gastric acid secretion model. *Biophysical Journal* **65**, 362-378.

De Ridder, C. and Jangoux, M. (1982). Digestive systems: echinoidea. In *Echinoderm nutrition*, (ed. M. Jangoux and J. M. Lawrence), pp. 213-234. Rotterdam: A.A. Balkema.

Decker, G. L., Morrill, J. B. and Lennarz, W. J. (1987). Characterization of sea urchin primary mesenchyme cells and spicules during biomineralization in vitro. *Development* **101**, 297-312.

Delpire, E., Kaplan, M. R., Plotkin, M. D. and Hebert, S. C. (1996). The Na-(K)-Cl cotransporter family in the mammalian kidney: molecular identification and function(s). *Nephrology Dialysis Transplantation* **11**, 1967-1973.

Doney, S. C., Fabry, V. J., Feely, R. A. and Kleypas, J. A. (2009). Ocean Acidification: The Other CO_2 Problem. *Annual Review of Marine Science* **1**, 169-192.

Dröse, S. and Altendorf, K. (1997). Bafilomycins and concanamycins as inhibitors of V-ATPases and P-ATPases. *Journal of Experimental Biology* **200**, 1-8.

Dubyak, G. R. (2004). Ion homeostasis, channels, and transporters: an update on cellular mechanisms. *Advances in Physiology Education* **28**, 143-154.

Dumont, C., Himmelman, J. H. and Russell, M. P. (2004). Size-specific movement of green sea urchins *Strongylocentrotus droebachiensis* on urchin barrens in eastern Canada. *Marine Ecology Progress Series* **276**, 93-101.

Dupont, S., Dorey, N., Stumpp, M., Melzner, F. and Thorndyke, M. (2012). Long-term and trans-life-cycle effects of exposure to ocean acidification in the green sea urchin *Strongylocentrotus droebachiensis*. *Marine Biology*.

Dupont, S., Ortega-Martínez, O. and Thorndyke, M. (2010). Impact of near-future ocean acidification on echinoderms. *Ecotoxicology* **19**, 449-462.

Ebert, T. A. and Southon, J. (2003). Red sea urchins (*Strongylocentrotus franciscanus*) can live over 100 years: confirmation with A-bomb ^{14}carbon. *Fishery Bulletin* **101**, 915-922.

Ecke, D., Bleich, M. and Greger, R. (1996). Crypt base cells show forskolin-induced Cl^- secretion but no cation inward conductance. *Pflügers Archiv European Journal of Physiology* **431**, 427-434.

Elliott, W. J. and Ram, C. V. S. (2011). Calcium Channel Blockers. *The Journal of Clinical Hypertension* **13**, 687-689.

Esbaugh, A., Heuer, R. and Grosell, M. (2012). Impacts of ocean acidification on respiratory gas exchange and acid–base balance in a marine teleost, *Opsanus beta*. *Journal of Comparative Physiology B: Biochemical, Systemic, and Environmental Physiology* **182**, 921-934.

Ettensohn, C. A., Wessel, G. M. and Wray, G. A. (2004). The Invertebrate Deuterostomes: An Introduction to Their Phylogeny, Reproduction, Development, and Genomics. In *Methods in Cell Biology*, vol. Volume 74 (ed. G. A. W. Charles A. Ettensohn and M. W. Gary), pp. 1-13: Academic Press.

Fabry, V. J., Seibel, B. A., Feely, R. A. and Orr, J. C. (2008). Impacts of ocean acidification on marine fauna and ecosystem processes. *ICES Journal of Marine Science* **65**, 414-432.

Farmanfarmaian, F. (1966). The respiratory physiology of echinoderms. In *Physiology of echinodermata*, (ed. R. A. Boolootian), pp. 245-265. New York, London; Sydney: Interscience Publisher.

Feely, R. A., Alin, S. R., Newton, J., Sabine, C. L., Warner, M., Devol, A., Krembs, C. and Maloy, C. (2010). The combined effects of ocean acidification, mixing, and respiration on pH and carbonate saturation in an urbanized estuary. *Estuarine Coastal and Shelf Science* **88**, 442-449.

Feely, R. A., Sabine, C. L., Lee, K., Berelson, W., Kleypas, J., Fabry, V. J. and Millero, F. J. (2004). Impact of Anthropogenic CO_2 on the $CaCO_3$ System in the Oceans. *Science* **305**, 362-366.

Fiandra, L., Casartelli, M. and Giordana, B. (2006). The paracellular pathway in the lepidopteran larval midgut: Modulation by intracellular mediators. *Comparative Biochemistry and Physiology Part A: Molecular & Integrative Physiology* **144**, 464-473.

Frisch, M. J., Trucks, G. W., Schlegel, H. B., Scuseria, G. E., Robb, M. A., Cheeseman, J. R., Scalmani, G., Barone, V., Mennucci, B., Petersson, G. A. et al. (2009). Gaussian 09 *Revision A.02*. Gaussian Inc., Wallingford CT

Fujino, Y., Mitsunaga, K., Fujiwara, A. and Yasumasu, I. (1985). Inhibition of $^{45}Ca^{2+}$ uptake in the eggs and embryos of the sea urchin, *Anthocidaris crassispina*, by several calcium antagonists, anion transport inhibitor, and chloride transport inhibitors. *Journal of Experimental Zoology* **235**, 281-288.

Fujino, Y., Mitsunaga, K. and Yasumasu, I. (1987). Inhibitory Effect of Omeprazole, a Specific Inhibitor of H^+, K^+-ATPase, on Spicule Formation in Sea Urchin Embryos and in Cultured Micromere-Derived Cells. *Development, Growth & Differentiation* **29**, 591-597.

Furuse, M. and Tsukita, S. (2006). Claudins in occluding junctions of humans and flies. *Trends in Cell Biology* **16**, 181-188.

Garzon-Muvdi, T., Schiapparelli, P., ap Rhys, C., Guerrero-Cazares, H., Smith, C., Kim, D.-H., Kone, L., Farber, H., Lee, D. Y., An, S. S. et al. (2012). Regulation of Brain Tumor Dispersal by NKCC1 Through a Novel Role in Focal Adhesion Regulation. *PLoS Biology* **10**, e1001320.

Gassner, D. and Komnick, H. (1981). Inhibition of a $Cl^-HCO_3^-$-ATPase in the avian salt gland by furosemide and ethacrynic acid. *Cell Biology International Reports* **5**, 239-246.

Gerencser, G. A. and Zhang, J. (2004). The Cl^- ATPase pump. *International Congress Series* **1275**, 104-113.

Gillen, C. M., Blair, C. R., Heilman, N. R., Somple, M., Stulberg, M., Thombre, R., Watson, N., Gillen, K. M. and Itagaki, H. (2006). The cation-chloride cotransporter, masBSC, is widely expressed in *Manduca sexta* tissues. *Journal of Insect Physiology* **52**, 661-668.

Gizurarson, S. (1993). The relevance of nasal physiology to the design of drug absorption studies. *Advanced Drug Delivery Reviews* **11**, 329-347.

Goeger, D. E., Riley, R. T., Dorner, J. W. and Cole, R. J. (1988). Cyclopiazonic acid inhibition of the Ca^{2+}-transport ATPase in rat skeletal muscle sarcoplasmic reticulum vesicles. *Biochemical Pharmacology* **37**, 978-981.

Green, C. R. (1981). Fixation-induced intramembrane particle movement demonstrated in freeze-fracture replicas of a new type of septate junction in echinoderm epithelia. *Journal of Ultrastructure Research* **75**, 11-22.

Green, C. R., Bergquist, P. R. and Bullivant, S. (1979). An anastomosing septate junction in endothelial cells of the phylum echinodermata. *Journal of Ultrastructure Research* **68**, 72-80.

Greger, R. (1981). Chloride reabsorption in the rabbit cortical thick ascending limb of the loop of Henle. *Pflügers Archiv European Journal of Physiology* **390**, 38-43.

Greger, R. (1995). Loop diuretics. In *Diuretics*, (ed. R. Greger H. Knauf and E. Mutschler), pp. 221-274. Berlin Heidelberg: Springer-Verlag.

Greger, R. (2000). Role of CFTR in the Colon. *Annual Review of Physiology* **62**, 467-491.

Greger, R. and Schlatter, E. (1981). Presence of luminal K^+, a prerequisite for active NaCl transport in the cortical thick ascending limb of Henle's loop of rabbit kidney. *Pflügers Archiv European Journal of Physiology* **392**, 92-94.

Grosell, M. and Genz, J. (2006). Ouabain-sensitive bicarbonate secretion and acid absorption by the marine teleost fish intestine play a role in osmoregulation. *American Journal of Physiology - Regulatory, Integrative and Comparative Physiology* **291**, R1145-R1156.

Guerinot, M. L. and Patriquin, D. G. (1981). The association of N_2-fixing bacteria with sea urchins. *Marine Biology* **62**, 197-207.

Günzel, D. and Yu, A. S. L. (2013). Claudins and the Modulation of Tight Junction Permeability. *Physiological Reviews* **93**, 525-569.

Gutowska, M., Melzner, F., Langenbuch, M., Bock, C., Claireaux, G. and Pörtner, H. O. (2010). Acid–base regulatory ability of the cephalopod (*Sepia officinalis*) in response to environmental hypercapnia. *Journal of Comparative Physiology B: Biochemical, Systemic, and Environmental Physiology* **180**, 323-335.

Haas, B. R. and Sontheimer, H. (2010). Inhibition of the Sodium-Potassium-Chloride Cotransporter Isoform-1 Reduces Glioma Invasion. *Cancer Research* **70**, 5597-5606.

Haas, M. and Forbush, B. (1998). The Na-K-Cl Cotransporters. *Journal of Bioenergetics and Biomembranes* **30**, 161-172.

Hannaert, P., Alvarez-Guerra, M., Pirot, D., Nazaret, C. and Garay, R. (2002). Rat NKCC2/NKCC1 cotransporter selectivity for loop diuretic drugs. *Naunyn-Schmiedeberg's Archives of Pharmacology* **365**, 193-199.

Hardin, J. (1988). The role of secondary mesenchyme cells during sea urchin gastrulation studied by laser ablation. *Development* **103**, 317-324.

Harkey, M. A. and Whiteley, A. H. (1980). Isolation, culture, and differentiation of echinoid primary mesenchyme cells. *Development Genes and Evolution* **189**, 111-122.

Heatfield, B. M. (1970). Calcification in echinoderms: effects of temperature and diamox on incorporation of Calcium-45 in vitro by regenerating spines of *Strongylocentrotus purpuratus The Biological Bulletin* **139**, 151-163.

Heatfield, B. M. and Travis, D. F. (1975). Ultrastructural studies of regenerating spines of the sea urchin *Strongylocentrotus purpuratus* I. Cell types without spherules. *Journal of Morphology* **145**, 13-49.

Hebert, S., Mount, D. and Gamba, G. (2004). Molecular physiology of cation-coupled Cl^- cotransport: the SLC12 family. *Pflügers Archiv European Journal of Physiology* **447**, 580-593.

HELCOM. (2009). Eutrophication in the Baltic Sea – An integrated thematic assessment of the effects of nutrient enrichment and eutrophication in the Baltic Sea region: Executive Summary. *Baltic Sea Environment Proceeding* **No. 155A**.

Hiebenthal, C., Philipp, E. R., Eisenhauer, A. and Wahl, M. (2012). Effects of seawater pCO_2 and temperature on shell growth, shell stability, condition and cellular stress of Western Baltic Sea *Mytilus edulis* (L.) and *Arctica islandica* (L.). *Marine Biology*, 1-15.

Hoffmann, E. K., Lambert, I. H. and Pedersen, S. F. (2009). Physiology of Cell Volume Regulation in Vertebrates. *Physiological Reviews* **89**, 193-277.

Hoffmann, E. K., Schettino, T. and Marshall, W. S. (2007). The role of volume-sensitive ion transport systems in regulation of epithelial transport. *Comparative Biochemistry and Physiology Part A: Molecular & Integrative Physiology* **148**, 29-43.

Huber, R., Kohl, B., Sachs, G., Senn-Bilfinger, J., Simon, W. A. and Sturm, E. (1995). The continuing development of proton pump inhibitors with particular reference to pantoprazole. *Alimentary Pharmacology & Therapeutics* **9**, 363-378.

Hwang, S. P. and Lennarz, W. J. (1993). Studies on the Cellular Pathway Involved in Assembly of the Embryonic Sea Urchin Spicule. *Experimental Cell Research* **205**, 383-387.

Hyman, L. H. (1955). The invertebrates. Vol IV Echinodermata. New York: McGraw-Hill Book Company, INC.

Inesi, G. and Sagara, Y. (1994). Specific inhibitors of intracellular Ca^{2+} transport ATPases. *The Journal of Membrane Biology* **141**, 1-6.

Ingersoll, E. P., McDonald, K. L. and Wilt, F. H. (2003). Ultrastructural localization of spicule matrix proteins in normal and metalloproteinase inhibitor-treated sea urchin primary mesenchyme cells. *Journal of Experimental Zoology Part A: Comparative Experimental Biology* **300A**, 101-112.

IPPC. (2007). Climate Change 2007 Synthesis Report, (ed.: Cambridge University Press, New York.

Isenring, P. and Forbush, B. (2001). Ion transport and ligand binding by the Na–K–Cl cotransporter, structure–function studies. *Comparative Biochemistry and Physiology Part A: Molecular & Integrative Physiology* **130**, 487-497.

Iwamoto, L. M., Fujiwara, N., Nakamura, K. T. and Wada, R. K. (2004). Na-K-2Cl cotransporter inhibition impairs human lung cellular proliferation. *American Journal of Physiology - Lung Cellular and Molecular Physiology* **287**, L510-L514.

Jayantha Gunaratne, H. and Vacquier, V. D. (2007). Sequence, annotation and developmental expression of the sea urchin Ca^{2+}-ATPase family. *Gene* **397**, 67-75.

Ji, W., Foo, J. N., O'Roak, B. J., Zhao, H., Larson, M. G., Simon, D. B., Newton-Cheh, C., State, M. W., Levy, D. and Lifton, R. P. (2008). Rare independent mutations in renal salt handling genes contribute to blood pressure variation. *Nature Genetics* **40**, 592-599.

Jokumsen, A. and Fyhn, H. J. (1982). The influence of aerial exposure upon respiratory and osmotic properties of haemolymph from two intertidal mussels, *Mytilus edulis* L. and *Modiolus modiolus* L. *Journal of Experimental Marine Biology and Ecology* **61**, 189-203.

Killian, C. E. and Wilt, F. H. (2008). Molecular Aspects of Biomineralization of the Echinoderm Endoskeleton. *Chemical Reviews* **108**, 4463-4474.

Kinne, R., Koenig, B., Hannafin, J., Kinne-Saffran, E., Scott, D. M. and Zierold, K. (1985). The use of membrane vesicles to study the NaCl/KCl cotransporter involved in active transepithelial chloride transport. *Pflügers Archiv European Journal of Physiology* **405**, S101-S105.

Kiyomoto, M., Zito, F., Costa, C., Poma, V., Sciarrino, S. and Matranga, V. (2007). Skeletogenesis by transfated secondary mesenchyme cells is dependent on extracellular matrix–ectoderm interactions in *Paracentrotus lividus* sea urchin embryos. *Development, Growth & Differentiation* **49**, 731-741.

Kobayashi, S. and Taki, J. (1969). Calcification in sea urchins. *Calcified Tissue International* **4**, 210-223.

Kosik-Bogacka, D., Banach, B., Tyrakowski, T. and Wojciechowska, I. (2002). Effect of capsaicin and dimethyl sulfoxide on ion transport in the selected experimental models. *Polish Journal of Pharmacology* **54**, 267-274.

Lamare, M. D. and Mladenov, P. V. (2000). Modelling somatic growth in the sea urchin *Evechinus chloroticus* (Echinoidea: Echinometridae). *Journal of Experimental Marine Biology and Ecology* **243**, 17-43.

Lane, N. J., Martinucci, G., Dallai, R. and Burighel, P. (1994). Electron microscopic structure and evolution of epithelial junctions. In *Molecular Mechanisms of Epithelial Cell Junctions: From Development to Disease*, (ed. S. Citi), pp. 23-43. Austin, Texas: R.G Landes company.

Lang, F., Busch, G. L., Ritter, M., Völkl, H., Waldegger, S., Gulbins, E. and Häussinger, D. (1998). Functional Significance of Cell Volume Regulatory Mechanisms. *Physiological Reviews* **78**, 247-306.

Larsen, B. K., Pörtner, H. O. and Jensen, F. B. (1997). Extra- and intracellular acid-base balance and ionic regulation in cod (*Gadus morhua*) during combined and isolated exposures to hypercapnia and copper. *Marine Biology* **128**, 337-346.

Lingrel, J. (1992). Na,K-ATPase: Isoform structure, function, and expression. *Journal of Bioenergetics and Biomembranes* **24**, 263-270.

Livingston, B. T., Killian, C. E., Wilt, F., Cameron, A., Landrum, M. J., Ermolaeva, O., Sapojnikov, V., Maglott, D. R., Buchanan, A. M. and Ettensohn, C. A. (2006). A genome-wide analysis of biomineralization-related proteins in the sea urchin *Strongylocentrotus purpuratus*. *Developmental Biology* **300**, 335-348.

Loong, A., Chew, S., Wong, W., Lam, S. and Ip, Y. (2012). Both seawater acclimation and environmental ammonia exposure lead to increases in mRNA expression and protein abundance of $Na^+K^+2Cl^-$ cotransporter in the gills of the climbing perch, *Anabas testudineus*. *Journal of Comparative Physiology B: Biochemical, Systemic, and Environmental Physiology* **182**, 491-506.

Märkel, K. (1990). Biomineralization in echinoderms. In *Echinoderm research*, (ed. D. Ridder P. Dubois Lahaye and Jangoux), pp. 277-282. Balkema, Rotterdam.

Märkel, K. and Röser, U. (1983a). Calcite-resorption in the spine of the echinoid *Eucidaris tribuloides*. *Zoomorphology* **103**, 43-58.

Märkel, K. and Röser, U. (1983b). The spine tissues in the echinoid *Eucidaris tribuloides*. *Zoomorphology* **103**, 25-41.

Matskevich, I., Hegney, K. L. and Flatman, P. W. (2005). Regulation of erythrocyte Na–K–2Cl cotransport by threonine phosphorylation. *Biochimica et Biophysica Acta (BBA) - Biomembranes* **1714**, 25-34.

Matsuoka, S., Nawada, T., Hisatome, I., Miyamoto, J., Hasegawa, J., Kotake, H. and Mashiba, H. (1991). Comparison of Ca^{2+} channel inhibitory effects of cibenzoline with verapamil on guinea-pig heart. *General Pharmacology: The Vascular System* **22**, 87-91.

Matter, K. and Balda, M. S. (2003). Functional analysis of tight junctions. *Methods* **30**, 228-234.

Mattsson, J. P., Väänänen, K., Wallmark, B. and Lorentzon, P. (1991). Omeprazole and bafilomycin, two proton pump inhibitors: Differentiation of their effects on gastric, kidney and bone H^+-translocating ATPases. *Biochimica et Biophysica Acta (BBA) - Biomembranes* **1065**, 261-268.

McConnaughey, T. A. and Whelan, J. F. (1997). Calcification generates protons for nutrient and bicarbonate uptake. *Earth-Science Reviews* **42**, 95-117.

McEdward, L. R. and Herrera, J. C. (1999). Body form and skeletal morphometrics during larval development of the sea urchin *Lytechinus variegatus* Lamarck. *Journal of Experimental Marine Biology and Ecology* **232**, 151-176.

Meidel, S. K. and Scheibling, R. E. (1999). Effects of food type and ration on reproductive maturation and growth of the sea urchin *Strongylocentrotus droebachiensis*. *Marine Biology* **134**, 155-166.

Melzner, F., Gutowska, M. A., Langenbuch, M., Dupont, S., Lucassen, M., Thorndyke, M. C., Bleich, M. and Pörtner, H. O. (2009). Physiological basis for high CO_2 tolerance in marine ectothermic animals: pre-adaptation through lifestyle and ontogeny? *Biogeosciences* **6**, 2313-2331.

Miles, H., Widdicombe, S., Spicer, J. I. and Hall-Spencer, J. (2007). Effects of anthropogenic seawater acidification on acid-base balance in the sea urchin *Psammechinus miliaris*. *Marine Pollution Bulletin* **54**, 89-96.

Miller, J., Fraser, S. E. and McClay, D. (1995). Dynamics of thin filopodia during sea urchin gastrulation. *Development* **121**, 2501-2511.

Miner, B. G. (2005). Evolution of feeding structure plasticity in marine invertebrate larvae: a possible trade-off between arm length and stomach size. *Journal of Experimental Marine Biology and Ecology* **315**, 117-125.

Mitsunaga-Nakatsubo, K., Yamazaki, K., Hatoh-Okazaki, M., Kawashita, H., Okamura, C., Akasaka, K., Shimada, H. and Yasumasu, I. (1996). cDNA Cloning of Na^+,K^+-ATPase α-Subunit from Embryos of the Sea Urchin, *Hemicentrotus pulcherrimus*. *Zoological Science* **13**, 833-841.

Mitsunaga, K., Akasaka, K., Shimada, H., Fujino, Y., Yasumasu, I. and Numanoi, H. (1986a). Carbonic anhydrase activity in developing sea urchin embryos with special reference to calcification of spicules. *Cell Differentiation* **18**, 257-262.

Mitsunaga, K., Fujino, Y. and Yasumasu, I. (1986b). Change in the Activity of Cl^-,HCO_3^--ATPase in Microsome Fraction daring Early Development of the Sea Urchin, *Hemicentrotus pulcherrimus*. *Journal of Biochemistry* **100**, 1607-1615.

Mitsunaga, K., Fujino, Y. and Yasumasu, I. (1987a). Distributions of H^+,K^+-ATPase and Cl^-,HCO_3^--ATPase in micromere-derived cells of sea urchin embryos. *Differentiation* **35**, 190-196.

Mitsunaga, K., Fujino, Y. and Yasumasu, I. (1987b). Probable Role of Allylisothiocyanate-Sensitive H^+, K^+-ATPase in Spicule Calcification in Embryos of the Sea Urchin, *Hemicentrotus pulcherrimus*. *Development, Growth & Differentiation* **29**, 57-70.

Mitsunaga, K., Fujiwara, A., Fujino, Y. and Yasumasu, I. (1989). Changes in the Activities of H^+, K^+-ATPase and Na^+, K^+-ATPase in Cultured Cells Derived from Micromeres of Sea Urchin Embryos with Special Reference to Their Roles in Spicule Rod Formation. *Development, Growth & Differentiation* **31**, 171-178.

Mitsunaga, K., Hatoh, M., Yamazaki, K., Yasumasu, I., Yamada, K., Akasaka, K. and Shimada, H. (1991). Expression of Na^+, K^+-ATPase alpha - subunit in embryos of the sea urchin, *Hemicentrotus pulcherrimus*, during early development. In *Biology of Echinodermata: Proceedings of the 7th International Echinoderm Conference, Japan (Atami) 9th - 14th September 1990,* (ed. Yanagisawa Yasumasu Oguro Suzuki and Motokawa), pp. 75-79. Balkema, Rotterdam.

Mitsunaga, K., Makihara, R., Fujino, Y. and Yasumasu, I. (1986c). Inhibitory effects of ethacrynic acid, furosemide, and nifedipine on the calcification of spicules in cultures of micromeres isolated from sea-urchin eggs. *Differentiation* **30**, 197-204.

Moitoza, D. J. and Phillips, D. W. (1979). Prey defence, predator preference, and non-random diet - the interactions between *Pycnopodia helianthoides* and two species of sea urchins. *Marine Biology* **53**, 299-304.

Morii, M., Takata, H., Fujisaki, H. and Takegucht, N. (1990). The potency of substituted benzimidazoles such as E3810, omeprazole, RO 18-5364 to inhibit gastric H^+,K^+-ATPase is correlated with the rate of acid-activation of the inhibitor. *Biochemical Pharmacology* **39**, 661-667.

Morse, J. W., Arvidson, R. S. and Luttge, A. (2007). Calcium carbonate formation and dissolution. *Chemical Reviews-Columbus* **107**, 342-381.

Muroi, M., Shiragami, N., Nagao, K., Yamasaki, M. and Takatsuki, A. (1993). Folimycin (Concanamycin A), a Specific Inhibitor of V-ATPase, Blocks Intracellular Translocation of the Glycoprotein of Vesicular Stomatitis Virus before Arrival to the Golgi Apparatus. *Cell Structure and Function* **18**, 139-149.

Nakano, E., Okoazaki, K. and Iwamatsu, T. (1963). Accumulation of radioactive calcium in larvae of the sea urchin *Pseudocentrotus depressus The Biological Bulletin* **125**, 125-132.

Nishihara, T., Akifusa, S., Koseki, T., Kato, S., Muro, M. and Hanada, N. (1995). Specific Inhibitors of Vacuolar Type H^+-ATPases Induce Apoptotic Cell Death. *Biochemical and Biophysical Research Communications* **212**, 255-262.

Okazaki, K. (1975). Spicule Formation by Isolated Micromeres of the Sea Urchin Embryo. *American Zoologist* **15**, 567-581.

Okazaki, K. and Inoué, S. (1976). Crystal property of the larval sea uchin spicule. *Development, Growth & Differentiation* **18**, 413-434.

Orr, J. C., Fabry, V. J., Aumont, O., Bopp, L., Doney, S. C., Feely, R. A., Gnanadesikan, A., Gruber, N., Ishida, A., Joos, F. et al. (2005). Anthropogenic ocean acidification over the twenty-first century and its impact on calcifying organisms. *Nature* **437**, 681-686.

Pane, E. F. and Barry, J. P. (2007). Extracellular acid-base regulation during short-term hypercapnia is effective in a shallow-water crab, but ineffective in a deep-sea crab. *Marine Ecology-Progress Series* **334**, 1-9.

Pansch, C., Nasrolahi, A., Appelhans, Y. and Wahl, M. (2012). Tolerance of juvenile barnacles (*Amphibalanus improvisus*) to warming and elevated pCO_2. *Marine Biology*, 1-13.

Pappone, P. A. and Lee, S. C. (1995). Alpha-adrenergic stimulation activates a calcium-sensitive chloride current in brown fat cells. *The Journal of General Physiology* **106**, 231-258.

Paradiso, A. M., Negulescu, P. A. and Machen, T. E. (1986). Na^+-H^+ and Cl^- OH^- (HCO_3^-) exchange in gastric glands. *American Journal of Physiology - Gastrointestinal and Liver Physiology* **250**, G524-G534.

Payne, J. A. and Forbush III, B. (1995). Molecular characterization of the epithelial Na-K-Cl cotransporter isoforms. *Current Opinion in Cell Biology* **7**, 493-503.

Peterson, W. L. (1997). The role of antisecretory drugs in the treatment of *Helicobacter pylori* infection. *Alimentary Pharmacology & Therapeutics* **11**, 21-25.

Politi, Y., Arad, T., Klein, E., Weiner, S. and Addadi, L. (2004). Sea Urchin Spine Calcite Forms via a Transient Amorphous Calcium Carbonate Phase. *Science* **306**, 1161-1164.

Politi, Y., Metzler, R. A., Abrecht, M., Gilbert, B., Wilt, F. H., Sagi, I., Addadi, L., Weiner, S. and Gilbert, P. U. P. A. (2008). Transformation mechanism of amorphous calcium carbonate into calcite in the sea urchin larval spicule. *Proceedings of the National Academy of Sciences* **105**, 17362-17366.

Poustka, A. J., Groth, D., Hennig, S., Thamm, S., Cameron, A., Beck, A., Reinhardt, R., Herwig, R., Panopoulou, G. and Lehrach, H. (2003). Generation, Annotation, Evolutionary Analysis, and Database Integration of 20,000 Unique Sea Urchin EST Clusters. *Genome Research* **13**, 2736-2746.

Pullikuth, A. K., Filippov, V. and Gill, S. S. (2003). Phylogeny and cloning of ion transporters in mosquitoes. *Journal of Experimental Biology* **206**, 3857-3868.

Raven, J., Caldeira, K., Elderfield, H., Hoegh-Guldberg, O., Liss, P., Riebesell, U., Shepherd, J., Turley, C. and Watson, A. (2005). Ocean acidification due to increasing atmospheric carbon dioxide, (ed. T. R. S. p. d. 12/05), pp. 60: The Clyvedon Press Ltd., Cardiff, UK.

Raz, S., Hamilton, P. C., Wilt, F. H., Weiner, S. and Addadi, L. (2003). The Transient Phase of Amorphous Calcium Carbonate in Sea Urchin Larval Spicules: The Involvement of Proteins and Magnesium Ions in Its Formation and Stabilization. *Advanced Functional Materials* **13**, 480-486.

Ries, J. B., Cohen, A. L. and McCorkle, D. C. (2009). Marine calcifiers exhibit mixed responses to CO_2-induced ocean acidification. *Geology* **37**, 1131-1134.

Romero, M., Fulton, C. and Boron, W. (2004). The SLC4 family of HCO_3^- transporters. *Pflügers Archiv European Journal of Physiology* **447**, 495-509.

Santos-Gouvea, I. A.-. and Freire, C. A. (2007). Effects of Hypo- and Hypersaline Seawater on the Microanatomy and Ultrastructure of Epithelial Tissues of *Echinometra lucunter* (Echinodermata: Echinoidea) of Intertidal and Subtidal Populations. *Zoological Studies* **46**, 203-215.

Santos, N. C., Figueira-Coelho, J., Martins-Silva, J. and Saldanha, C. (2003). Multidisciplinary utilization of dimethyl sulfoxide: pharmacological, cellular, and molecular aspects. *Biochemical Pharmacology* **65**, 1035-1041.

Sawabe, T., Oda, Y., Shiomi, Y. and Ezura, Y. (1995). Alginate degradation by bacteria isolated from the gut of sea urchins and abalones. *Microbial Ecology* **30**, 193-202.

Scheibling, R. E. and Hatcher, B. G. (2007). Ecology of *Strongylocentrotus droebachiensis*. In *Edible sea urchins: Biology and ecology second edition*, (ed. J. M. Lawrence), pp. 353-392. Amsterdam: Elsevier.

Scheibling, R. S. and Anthony, S. A. (2001). Feeding, growth and reproduction of sea urchins *Strongylocentrotus droebachiensis* on single and mixed diets of kelp (*Laminaria* spp.) and the invasive alga *Codium fragile* ssp. *tomentosoides*. *Marine Biology* **139**, 139-146.

Shirayama, Y. and Thornton, H. (2005). Effect of increased atmospheric CO_2 on shallow water marine benthos. *Journal of Geophysical Research: Oceans* **110**, C09S08.

Siikavuopio, S. I., Mortensen, A., Dale, T. and Foss, A. (2007). Effects of carbon dioxide exposure on feed intake and gonad growth in green sea urchin, *Strongylocentrotus droebachiensis*. *Aquaculture* **266**, 97-101.

Sikes, C. S., Okazaki, K. and Fink, R. D. (1981). Respiratory CO_2 and the supply of inorganic carbon for calcification of sea urchin embryos. *Comparative Biochemistry and Physiology Part A: Physiology* **70**, 285-291.

Skaer, H. B., Maddrell, S. H. and Harrison, J. B. (1987). The permeability properties of septate junctions in Malpighian tubules of *Rhodnius*. *Journal of Cell Science* **88**, 251-265.

Smith, M. M., Cruz Smith, L., Cameron, R. A. and Urry, L. A. (2008). The larval stages of the sea urchin, *Strongylocentrotus purpuratus*. *Journal of Morphology* **269**, 713-733.

Somasekharan, S., Tanis, J. and Forbush, B. (2012). Loop Diuretic and Ion-binding Residues Revealed by Scanning Mutagenesis of Transmembrane Helix 3 (TM3) of Na-K-Cl Cotransporter (NKCC1). *Journal of Biological Chemistry* **287**, 17308-17317.

Spicer, J. I. (1995). Oxygen and acid-base status of the sea urchin *Psammechinus miliaris* during environmental hypoxia. *Marine Biology* **124**, 71-76.

Spicer, J. I., Taylor, A. C. and Hill, A. D. (1988). Acid-base status in the sea urchins *Psammechinus miliaris* and *Echinus esculentus* (Echinodermata: Echinoidea) during emersion. *Marine Biology* **99**, 527-534.

Spicer, J. I. and Widdicombe, S. (2012). Acute extracellular acid-base disturbance in the burrowing sea urchin *Brissopsis lyrifera* during exposure to a simulated CO_2 release. *Science of The Total Environment* **427–428**, 203-207.

Spicer, J. I., Widdicombe, S., Needham, H. R. and Berge, J. A. (2011). Impact of CO_2-acidified seawater on the extracellular acid-base balance of the northern sea urchin *Strongylocentrotus dröebachiensis*. *Journal of Experimental Marine Biology and Ecology* **407**, 19-25.

Storch, V. and Welsch, U. (2009). Kükenthal Zoologisches Praktikum. Heidleberg: Spektrum Akademischer Verlag.

Stumpp, M., Hu, M. Y., Melzner, F., Gutowska, M. A., Dorey, N., Himmerkus, N., Holtmann, W. C., Dupont, S. T., Thorndyke, M. C. and Bleich, M. (2012a). Acidified seawater impacts sea urchin larvae pH regulatory systems relevant for calcification. *Proceedings of the National Academy of Sciences* **109**, 18192-18197.

Stumpp, M., Trübenbach, K., Brennecke, D., Hu, M. Y. and Melzner, F. (2012b). Resource allocation and extracellular acid-base status in the sea urchin *Strongylocentrotus droebachiensis* in response to CO_2 induced seawater acidification. *Aquatic Toxicology* **110–111**, 194-207.

Swan, E. F. (1961). Some observations on the growth rate of sea urchins in the genus Strongylocentrotus *The Biological Bulletin* **120**, 420-427.

Sweadner, K. J. (1985). Enzymatic properties of separated isozymes of the Na,K-ATPase. Substrate affinities, kinetic cooperativity, and ion transport stoichiometry. *Journal of Biological Chemistry* **260**, 11508-11513.

Sweadner, K. J. (1989). Isozymes of the Na^+/K^+-ATPase. *Biochimica et Biophysica Acta (BBA) - Reviews on Biomembranes* **988**, 185-220.

Swift, D. M., Sikes, C. S. and Wheeler, A. P. (1986). Analysis and function of organic matrix from sea urchin tests. *Journal of Experimental Zoology* **240**, 65-73.

Tambutté, E., Allemand, D., Mueller, E. and Jaubert, J. (1996). A compartmental approach to the mechanism of calcification in hermatypic corals. *Journal of Experimental Biology* **199**, 1029-1041.

Tegner, M. J. and Levin, L. A. (1983). Spiny lobsters and sea-urchins - analysis of a predator prey interacion *Journal of Experimental Marine Biology and Ecology* **73**, 125-150.

Thomsen, J., Gutowska, M. A., Saphörster, J., Heinemann, A., Trübenbach, K., Fietzke, J., Hiebenthal, C., Eisenhauer, A., Körtzinger, A., Wahl, M. et al. (2010). Calcifying invertebrates succeed in a naturally CO_2-rich coastal habitat but are threatened by high levels of future acidification. *Biogeosciences* **7**, 3879-3891.

Todgham, A. E. and Hofmann, G. E. (2009). Transcriptomic response of sea urchin larvae *Strongylocentrotus purpuratus* to CO_2-driven seawater acidification. *Journal of Experimental Biology* **212**, 2579-2594.

Tokin, I. B. and Filimonova, G. F. (1977). Electron microscope study of the digestive system of *Strongylocentrotus droebachiensis* (Echinodermata: Echinoidea). *Marine Biology* **44**, 143-155.

Trendelenburg, P. (1917). Physiologische und pharmakologische Versuche über die Dünndarmperistaltik. *Archiv für experimentelle Pathologie und Pharmakologie* **81**, 55-129.

Trübenbach, K. (2009). Effects of ocean acidification on key physiological parameters in the green sea urchin *Strongylocentrotus droebachiensis*, (ed., pp. 104. Kiel: CAU Kiel.

Tu, Q., Cameron, R. A., Worley, K. C., Gibbs, R. A. and Davidson, E. H. (2012). Gene structure in the sea urchin *Strongylocentrotus purpuratus* based on transcriptome analysis. *Genome Research* **22**, 2079-2087.

Ueberfeld, J., Parthasarathy, N., Zbinden, H., Gisin, N. and Buffle, J. (2001). Coupling Fiber Optics to a Permeation Liquid Membrane for Heavy Metal Sensor Development. *Analytical Chemistry* **74**, 664-670.

Unkles, S. E. (1977). Bacterial flora of the sea urchin *Echinus esculentus*. *Applied and Environmental Microbiology* **34**, 347-350.

Urry, L. A., Hamilton, P. C., Killian, C. E. and Wilt, F. H. (2000). Expression of Spicule Matrix Proteins in the Sea Urchin Embryo during Normal and Experimentally Altered Spiculogenesis. *Developmental Biology* **225**, 201-213.

Uyama, Y., Imaizumi, Y. and Watanabe, M. (1992). Effects of cyclopiazonic acid, a novel Ca^{2+}-ATPase inhibitor, on contractile responses in skinned ileal smooth muscle. *British Journal of Pharmacology* **106**, 208-214.

Van Zwieten, P. A. (1998). The Pharmacological Properties of Lipophilic Calcium Antagonists. *Blood Pressure* **7**, 5-9.

Waldbusser, G. G., Voigt, E. P., Bergschneider, H., Green, M. A. and Newell, R. I. E. (2011). Biocalcification in the Eastern Oyster (*Crassostrea virginica*) in Relation to Long-term Trends in Chesapeake Bay pH. *Estuaries and Coasts* **34**, 221-231.

Wallach, D. F. H., Surgenor, D. M., Soderberg, J. and Delano, E. (1959). Preparation and Properties of 3,6-Dihydroxy-2,4-bis-[N-N'-di-(carboxymethyl)-aminomethyl] fluoran. *Analytical Chemistry* **31**, 456-460.

Warth, R., Bleich, M., Thiele, I., Lang, F. and Greger, R. (1998). Regulation of the $Na^+2Cl^-K^+$ cotransporter in in vitro perfused rectal gland tubules of *Squalus acanthias*. *Pflügers Archiv European Journal of Physiology* **436**, 521-528.

Weiner, S. and Addadi, L. (2011). Crystallization Pathways in Biomineralization. *Annual Review of Materials Research* **41**, 21-40.

Weiner, S., Levi-Kalisman, Y., Raz, S. and Addadi, L. (2003). Biologically Formed Amorphous Calcium Carbonate. *Connective Tissue Research* **44**, 214-218.

Wessel, G. M., Etkin, M. and Benson, S. (1991). Primary mesenchyme cells of the sea urchin embryo require an autonomously produced, nonfibrillar collagen for spiculogenesis. *Developmental Biology* **148**, 261-272.

Wessel, G. M. and Wikramanayake, A. (1999). How to grow a gut: ontogeny of the endoderm in the sea urchin embryo. *BioEssays* **21**, 459-471.

Wilkie, I. C. (2005). Mutable Collagenous Tissue: Overview and Biotechnological Perspective vol. 39 (ed. V. Matranga), pp. 221-250: Springer Berlin Heidelberg.

Wilson, C., Venditti, R., Rega, L. R., Colanzi, A., D'Angelo, G. and De Matteis, M. A. (2011). The Golgi apparatus: an organelle with multiple complex functions. *Biochemical Journal* **433**, 1-9.

Wilt, F. H. (1999). Matrix and Mineral in the Sea Urchin Larval Skeleton. *Journal of Structural Biology* **126**, 216-226.

Wilt, F. H. (2002). Biomineralization of the Spicules of Sea Urchin Embryos. *Zoological Science* **19**, 253-261.

Wilt, F. H., Killian, C. E., Hamilton, P. and Croker, L. (2008). The dynamics of secretion during sea urchin embryonic skeleton formation. *Experimental Cell Research* **314**, 1744-1752.

Wright, E. M. (1993). The Intestinal Na^+/Glucose Cotransporter. *Annual Review of Physiology* **55**, 575-589.

Wright, S. H. (2004). Generation of resting membrane potential. *Advances in Physiology Education* **28**, 139-142.

Xu, J. C., Lytle, C., Zhu, T. T., Payne, J. A., Benz, E. and Forbush, B. (1994). Molecular cloning and functional expression of the bumetanide-sensitive Na-K-Cl cotransporter. *Proceedings of the National Academy of Sciences* **91**, 2201-2205.

Yasumasu, I., Mitsunaga, K. and Fujino, Y. (1985). Mechanism for electrosilent Ca^{2+} transport to cause calcification of spicules in sea urchin embryos. *Experimental Cell Research* **159**, 80-90.

Yoshimori, T., Yamamoto, A., Moriyama, Y., Futai, M. and Tashiro, Y. (1991). Bafilomycin A1, a specific inhibitor of vacuolar-type H($^+$)-ATPase, inhibits acidification and protein degradation in lysosomes of cultured cells. *Journal of Biological Chemistry* **266**, 17707-17712.

Yu, M.-J. and Beyenbach, K. W. (2001). Leucokinin and the modulation of the shunt pathway in Malpighian tubules. *Journal of Insect Physiology* **47**, 263-276.

Zeebe, R. E. and Wolf-Gladrow, D. (2001). CO_2 in seawater: Equlibrium, kinetics, isotopes. Amsterdam: Elsevier Science B.V.

Zhang, Z., Schwartz, S., Wagner, L. and Miller, W. (2000). A Greedy Algorithm for Aligning DNA Sequences. *Journal of Computational Biology* **7**, 203-214.

Zhu, X., Mahairas, G., Illies, M., Cameron, R. A., Davidson, E. H. and Ettensohn, C. A. (2001). A large-scale analysis of mRNAs expressed by primary mesenchyme cells of the sea urchin embryo. *Development* **128**, 2615-2627.

APPENDIX

Nucleotide sequences of transcriptomal reads

The following three transcriptomal reads of 2- and 6-day old larvae were kindly provided by Ulrike Findeisen, Meike Stumpp and Frank Melzner (*unpublished*).

1) (green in Figure 60)

CTGATCTTCTCCGTTGCTAACACCATCGCCGTTGCTATGTACGTCGTGGTTTCTCGGAGACGGTCGCTCTCCTGC
TAAGGATATGATGCTCAGATGGTCGACCTGGTCAACGATGTCAGGATCATTGGTATGATCACCATCGTCGTCCT
CCTGGCCATCATCTTTATAGGCATGGCATGGGAAGCTAAGATTCAGCTGGTCCTTCTGGTTGTACTCAGTATAG
CCATTCTTAACATGATTGTTGGGAGTTTCCTTCCTGTAACAGAGGCTAAAGCTGCAAAGGGATTCACTGGATAC
AGAAAGGATGTCTTTGTTCAAAATCTGAAGCCAGGCTTTCAGAATGGAGAGACCTTCTTCTCCGTCTTCTCCAT
CTTCTTCCCGGCAGCCACCGGTATCTTAGCAGGAGCTAACATCTCAGGAGATCTTCATGATGCCCAGAAGGCCA
TCCCCAAGGGGACCCTATGGGCCATCCTCATCTCCAC

2) (red in Figure 60)

TGAAGTAGACGAAGAGGAGGAGGAGAAAGAGAAAGAGAACGCCAAGGAATCCACCTCGTTGGTCCATAACTC
GGACAATCAGACGAACAATCAATCACGCCCTCTATTGACCAGCGGGAAGCTGGTGCGCAACATGCCGATCGGC
TCCGTCATCAAGACCACACAGAAGTTCCAGGGCAAACAGCCGAAGGGAACCATCGATGTCTGGTGGCTGTTTG
ATGATGGAGGTCTGACGCTGCTGATTCCCCATCTGCTCACCCCAGAAAGACCAACTGGCAGAAGTGTAAGCTG
AGGGTCTTTGCTAGCGGCAAGAAGGAAGAGTCGATGATGAGAAGAGAAAGATGGCTAACTTGCTGAGCAAGT
TCCGATCCCTCACGACAGTGTGAACATCATTCCAAACATCGGCAAGTTGCCATCTGCAGCAAGTATAGAGAAA
TTTAACAAGATCA

3) (olive in Figure 60)

CAAGTATAGAGAAATTAACAAGATCATCAAGCCATGGTACTGAGGAGGCGAAGACCCAAGCGTATCCATGGA
AGATCTCCGAACAGGATGTGGAATCGCTCAATGATAAGACAATGAGACAAATCCGTCTTAGAGAACTTCTTCA
AGAGCACTCCAAAGATGCCAGCCTTATTGTTATGTCTCTACCGATGCCCAGGAAGAGTCTGTGTCCACCCATCA
TGTACATGTGCTGGCTAGAAGTGCTTTCTGGTGACCTCCCTCCAATGCTGCTCATGAGAGGCAATCAAACCAGT
GTTCTCACCTACTACTCATAGTATACGCTTCAGTAGATTGTTCATCTCAGGCAGACTGAACGCACCCATATGTA
ATACATCATGCTCCTGAGAGGCAACCAAATCAGAG

Figure 60 All three transcriptomal reads for NKCC in *S. droebachiensis*, given in green, red and olive. The grey bar symbolises the *S. purpuratus* nucleotide sequence and is shown to localise to the transcriptomal reads.

Nucleotide sequences of sequenced RT-PCR products

The following nucleotide sequences resulted from sequencing different RT-PCR products conducted with 5-day old larvae.

4) product generated from primer pair 3

CNTNAGGAGNCNGGGCACGANGTCAGGGATCATTGGGTATGATCACCATCGTCGTCCTCCTGGCCATCATCTT
CATAGGCATGGCATGGGAAGCCAAGATTCAGCTGGTCCTTCTGGTTGTACTCAGTATAGCCATTCTTAACATGA
TTGTTGGGAGTTTCCTTCCTGTAACAGAGGCTAAAGCTGCAAAGGA

5) product generated from primer pair 7

NCATTCGCATCGAGACATCATCGCGCCCTCTATTGACCAGCGGGAAGCTGGTCCGCAACATGCCGATTGGCTCC
GTCATCAAGACCACACAGAAGTTCCAGGGCAAACAGCCCAAGGGAACCATCGACGTCTGGTGGCTGTTTGATG
ATGGAGGTCTGACGCTGCTGATTCCCCATCTGCTCACCCAAAAGACCAACTGGCAGAAGTGTAAGCTGAGGGT
CTTTGCTAGCGGCAAGAAGGAAAGAGTCGATGATGAGAAGAGAAAGATGGCTAACTTGCTGAGCAAGTTCCG
TATCCCTCACGACAGTGTGAACATCATTCCAAACATCGGCAAGTTGCCATCTGCAGCAAGTATAGAGAAATTC
AACAAGATCATCCAGCCATGGTTACTGAAGGAGGGCGAAGACCCCAAGATGTATCCNTGGAANATCTCTGAAC
ANGATGTGGAATCNCTCAATGATAANACAATGANACAAATCCNTCTTANANAACTTCTTCAANANCACTCCNA
ANATNCCNNCCTTATTGTTATGTCTCTACCNATNCCCNNNANNANTCTNTGTCCNCCCNTCNNGTNCNTNTNCT
NNTTANAANTNCTTTCTNNTNACCTCCCTCCNNT

6) product generated from primer pair 4

NNNGTCTGNCCTGGTGGGCGCTCTCCTCACCATCGCCATCATCTCAGGTCTCTACATGTACGTCCACAGCACAA
AACCAGAGGTAAATTGGGGAGACTCAAACCAAGCGTTCTTATACAAAAGAGCAATCCAGACAACTATCAAGCT
AGGCAATGTACCAGAGCATGTCAAGACATTCAGACCTCAAATCTTACTTCTGACTGGGCCCCCTAACTGCCGTC
CAGCCATGCTTCATCTATGTTCACATATCACCAAAAATACCAGCTTGCTACTGTGTGGAAACGTTATTATAGGT
GAACAACCCAATGTTTTTAGACAACTCAGAACAACAGAATATGAGCAATGGCTAAACTACAAGAAAATCAAG
GCTTTCCTTGCCTTCACTACAGCACCAACACTCAGGAAAGGAGCACAACAACTCATGCAGCTTGGAGGATTGG
GTAAGATCCGTCCTAACACCATGTTTATGGGATTCAAGAGAAACTGGAGTGCCTGCAAACCTGAAGACCTCTT
AGATTACGTTGGCATCATACACGATGCCTTTGATCTACAGCTGGGTGTGTGTATCCTGAGGTTGCAAGAGGGTT
CTGATGTATCAGCAGCTTTAGACTTTGAGAAGGAGGAGCCTTATAACCAGAAGGAAGATCTTCAGCAGGAAAA
TGAGAAAGCAAGNAACAGCGTCACNACGCCAACNATCACGATCACGGGANCTACGCNANAGGACAACGCGAT
GAAAGAGAACTTNAGNTGAANTNANNNAANAGNANGAGGGNAANGAGAAGTNNAAANNNCCNNNNNNN

7) product generated from primer pair 5

CCNNCNTTAATNNGTTNGGCATCATACACGATGCCTTTGATCTACAGCTGGGTGTGTGTATCCTGAGGTTGCAA
GAGGGTTCTGATGTATCAGCAGCTTTAGACTTTGAGAAGGAGGAGCCTTATAACCAGAAGGAAGATCTTCAGC
AGGAAAATGAGAAAGCAAGTAACAGCGTCACCACGCCAACCATCACGATCACGGGAACTACGCAAAAGGACA
ACGCGATGAAAGAGAACTTAGATGAAGTAGACGAAGAGGAGGAGGAGAAAGAGAAAGAGAACGCCAAGGAA
TCCACCTCGCTGGTCCATAACTCNNACAATCAGACNAACAATCAATCNCNCCCTCTATTGACCANCGGGAANC
TGGTNCGCANCATGCCNATCGNCTCCNTCNTCNNNACCACNCNNAANTTCCNGGGCAAACNNCCNANNGNAA
CCNTCNATNTCTGGTGNCTGTTTNATNATNNANGTCTNACNCTNCTNATTCCCCNTCTNCTC

8) product generated from primer pair 6

TTTTATCGGCGATGAGCCAGAGGTCGACCTGGTCACGATGTCAGGATCATTGGTATGATCACCATCGTCGTCCT
CCTGGCCATCATCTTTATAGGCATGGCATGGGAAGCTAAGATTCAGCTGGTCCTTCTGGTTGTACTCAGTATAG
CCATTCTTAACATGATTGTTGGGAGTTTCCTTCCTGTAACCGAGGCTAAAGCTGCAAAGGGATTCACTGGATAC
AGAAAGGATGTCTTCGTACAAAATCTGAAGCCCGGCTTTCAGAATGGAGAGACCTTCTTCTCCGTCTTCTCCAT
CTTCTTCCCAGCAGCCACCGGTATCTTAGCGGGAGCCAACATCTCCGGAGATCTTCATGACGCCCAGAAGGCC
ATCCCCAAGGGGACCCTATGGGCCATCCTGATCTCCACCGTCATCTACGTGGGTCTCTCCTGGCTCATAGGAGG
CTGCATGATCAGGGAGGCTACAGGGAGCATCGCCGACGTGATAGCAGGGAACGTCACCACCGCATGCCTGAAT
GGGACCGTCGAGTGCGAGTATGGGATTGTCAATGACCTGGCTGCAGCCAAGATCATCTCTGGATGGGTGCCTT
TAGTTCTGGCTGGAATCTTTGCTGCATCTCTCTCCTCGGCTCTGGCCAGCTTGGTCAGTGCTCCAAAGGTGTTCC
AGGCTGTCTGCAAGGACAAGATCTTCCCTAAGATTGAGTACTTTGCTCATGGTGTAGGAACGGGTGATGAACC
CAAGAGGGCCTATGTGCTCACCTTCTTCATCGCCGCCGCATTCATTGCTATAGGTGATCTGAACACCGATTGCT
CCTACTCATCTCAAACTTCCTTCTTGGGCTTCCAAATGCTCTCAATCACCTTCTCCTTGCTTTCTCTGCATTCCCT
AGCCAAAGTCACCCAACGCTGGGAAAAAGAAGACCCCATTCCCAAGAAAAACCAAAAAAACACGGGGCGGA
AAAGGGGGGGCGGCGCGGGGGAGGAAGAGGTGATGGTATGATGGCAAGCTCTAGGAGCACGAGATGTCGGAT
GTGGGCGCTGTCTGGATATCGACGAAGC

Affirmation

Wiebke Holtmann
Mangoldtstrasse 35
24106 Kiel

Erklärung gem. §8 der Promotionsordnung:

Ich erkläre hiermit,

a) dass die Abhandlung - abgesehen von der Beratung durch die Betreuerin oder den Betreuer - nach Inhalt und Form die eigene Arbeit ist,

b) dass diese Arbeit vor dem jetzigen Promotionsverfahren keinem anderen Promotionsverfahren unterzogen wurde;

c) dass die Arbeit unter Einhaltung der Regeln guter wissenschaftlicher Praxis der Deutschen Forschungsgemeinschaft entstanden ist.

Gez. Wiebke Holtmann

Acknowledgements

This thesis was funded by the project “BIOACID”, funded by the Federal Ministry of Education and Research (BMBF, FKZ 03F0608M) whom I thank for the financial support.
The monoclonal antibody T4, developed by Christina Lytle and Bliss Forbush III, was obtained from the Developmental Studies Hybridoma Bank, developed under the auspices of the NICHD and maintained by The University of Iowa, Department of Biology, Iowa City, IA 52242.

I would like to thank my supervisors Prof. Dr. Markus Bleich and Prof. Dr. Frank Melzner for giving me the chance to work on this interesting thesis and for their support and fruitful discussions throughout my dissertation.

I thank Dr. Nina Himmerkus und Dr. Magdalena Gutowska for their support and methodical discussions in the last years. A big ‘thank you’ to Dr. Kerstin Suffrian, Dipl. Biol. Sandra Grüssel, Vera Wulfmeyer, Annalisa Krause, Caroline Sandmann, and Allein Plain for all the lab time, support and off-time.

For urchin discussions, sharing of material and the opportunity of a research visit I thank Dr. Sam Dupont and Dr. Meike Stumpp. Dipl. Biol. Ulrike Findeisen I thank for the help with the transcriptomal data of *Strongylocentrotus droebachiensis* larvae. Further, I thank M. Stumpp and F. Melzner for the opportunity to gain the transcriptomal sequences and Rüdiger Siek is thanked for the RT-PCR lab assistance.
I would like to thank Prof. Dr. Dan Jackson for his trys on the *in situ* hybridisation and for the nice telephone discussions.
Dr. Sönke Cordeiro und Dr. Hariolf Fritzenschaft enabled me to use their sequencing account and supported me during RT-PCR. Thank you for this.
For the help in cultivation of the sea urchins I thank Ashlie Cipriano and Stephanie Syré.

Ute Schuldt and Arno Lettmann of the Institute of Geosciences are thanked for their support at the Scanning Electron Microscope. Thank you to the laboratory assistance of the Institute of Physiology, namely Thomas Stegmann, Regina Lingg and Inka Geurink for their assistance in preparing experimental solutions, drug stock solutions and assistance in paraffin-histology.

For the introduction into quantum chemical calculations I thank Dr. Benjamin Sahlmann.

Many thanks to my family and Morten for all their support.

Curriculum vitae

Persönliche Daten

Name: Wiebke Catharina Holtmann
E-Mail: holtmann.wiebke@gmail.com

Schulische Ausbildung

Sept 1999 - Jun 2002	Besuch des „Niedersächsisches Internatsgymnasium Bad Bederkesa“, Abschluss Abitur

Studium

Okt 2002 - Jan 2009	Studium der Biologie mit Abschluß Diplom an der Christian-Albrechts-Universität zu Kiel; Hauptfach: Biologische Meereskunde, Nebenfächer: Zoologie, Toxikologie Diplomarbeitsthema: „Electrophysiological studies on the cold-water coral *Lophelia pertusa*“
Jan 2006 - Jun 2006	Erasmus-Studium an der Universitetet i Tromsø, Norwegen
ab Feb 2009	Promotion am Physiologischen Institut, CAU Kiel Thema: „Sea urchin membrane transport mechanisms for calcification and pH homeostasis“; innerhalb des BMBF geförderten Projektes „BIOACID”; Teilnahme an der „Integrated School of Ocean Sciences“

Tätigkeiten als studentische Hilfskraft

März 2003 - Feb 2007	studentische Hilfskraft im Aquarium; GEOMAR | Helmholtz-Zentrum für Ozeanforschung Kiel
Mai 2005	studentische Hilfskraft im Rahmen einer Sammelausfahrt mit FK „Littorina“; GEOMAR
Nov 2006 - Apr 2008	studentische Hilfskraft im Rahmen des DFG geförderten Forschungsvorhabens „Kaltwasserkorallen“; GEOMAR
Apr 2008 - Okt 2008	studentische Hilfskraft am GEOMAR | Helmholtz-Zentrum für Ozeanforschung Kiel

Lehre

SoSe 2009	Betreuung einer Studentin im Seminar „Marine Animal Physiology“ am GEOMAR, Thema „Epigenetics“

SS 2009 - WS 2012/2013	Betreuung des Medizinerpraktikums Physiologie, Themen: „Vestibularapparat und Somatosensorik“ (1x) „Herz und Elektrokardiogramm“ (2x) „Membranpotenzial und epithelialer Transport“ (3x) „Arbeitsphysiologie“ und „Säure-Basen-Haushalt“ (2x)
Jan 2012	Zweitägige Betreuung einer Biologie-Profil-Klasse, 12ter Jahrgang an der Wattenmeerstation List auf Sylt, AWI Vortrag: „Seeigel und Ozeanversauerung – Ein Einblick in eine Doktorarbeit“

Veröffentlichungen

Publikationen

Stumpp, M., et al. (2012) Acidified seawater impacts sea urchin larvae pH regulatory systems relevant for calcification, PNAS, doi: 10.1073/pnas.1209174109

Holtmann, W.C. et al. (2013) Maintenance of coelomic fluid pH in sea urchins exposed to elevated CO_2: the role of body cavity epithelia and stereom dissolution, Marine Biology, *accepted*

Poster und Vorträge

Suffrian, K. et al. (2009) Microfluorimetric and electrophysiological approaches to acid base transport physiology in marine organisms (Vortrag); Vorstellung der Diplomarbeit, Seminar AWI, Bremerhaven

Holtmann, W., et al. (2010) Microfluorimetric and electrophysiological studies of the cellular mechanisms underlying endoskeleton calcification in the sea urchin *Strongylocentrotus droebachiensis* (Poster); BIOACID/EPOCA/UKOARP meeting Bremerhaven, Germany

Krause, S., et al. (2010) High Mg-carbonate precipitation in the EPS of a sulfate-reducing bacterium (Poster); Hamburg-Kiel-Bremen PhD student conference / Cluster meeting, Hamburg, Germany

Holtmann, W., et al. (2011) Effects of ocean acidification on growth, calcification and pH homeostasis in the sea urchin *Strongylocentrotus droebachiensis* (Poster); BIOACID Meeting Bremen, Germany

Form, A., et al (2011) Acclimation effects of ocean acidification in the cold-water coral *Lophelia pertusa* and first investigations of single-channel activities (Poster); BIOACID Meeting Bremen, Germany

Holtmann, W., et al. (2012) Involvement of the $Na^+2Cl^-K^+$ cotransporter in spicule calcification of sea urchin larvae (Poster); 91st annual meeting of the DPG, Dresden, Germany and Future Ocean Cluster Retrear, Schleswig, Germany

Konferenzen

Ostseephysiologentagung, Greifswald (08. - 09.05.2009)
BIOACID Kickoff Meeting, Kiel (27. - 29.10.2009)
BIOACID / EPOCA / UKOARP Treffen, Bremerhaven (27. - 30.09.2010)
91. jährliche Treffen der DPG, Dresden (22. - 25.03.2012)

Future Ocean Cluster Retreat, Schleswig (20. - 21.08.2012)
Workshop (‘Analysis of transepithelial diffusion voltages as a measure of paracellular ion selectivity and permeability’), Sandbjerg, Dänemark (27. - 29.09.2012)

Preise

Posterpreis in der Session „Cellular Physiology”; 91st annual meeting of the DPG, Dresden Holtmann, W., et al. (2012) Involvement of the $Na^{+}2Cl^{-}K^{+}$ cotransporter in spicule calcification of sea urchin larvae

Fortbildungen

- Oral Presentation Skills
- Scientific Image Analysis with ImageJ
- Analysis of Univariate Data Sets – First Steps in R
- Career Planning for PhD Students: Application Standards – Personal Strategies
- Getting research published: Writing Effectively and Well in Science
- Basics of Professional University Teaching
- Premiumprogramm Hochschuldidaktik
- Methodenbausteine I Gruppenarbeit in Lehrveranstaltungen
- Methodenbausteine II Ein Leitfaden für gute Referate
- Digitale Bildbearbeitung mit Photoshop
- Sprachlich präsent - Natürlich, sicher und interessant vortragen
- Carbon footprint: The universal currency for climate change mitigation?
- Kernkompetenz Kommunikation